THE UNIVERSITY OF CHICAGO

INVESTIGATING THE HYDROLOGY OF ICE SHELVES, AND ITS IMPLICATIONS FOR ICE-SHELF STABILITY

A DISSERTATION SUBMITTED TO
THE FACULTY OF THE DIVISION OF THE PHYSICAL SCIENCES
IN CANDIDACY FOR THE DEGREE OF
DOCTOR OF PHILOSOPHY

DEPARTMENT OF THE GEOPHYSICAL SCIENCES

BY
GRANT JOHN MACDONALD

CHICAGO, ILLINOIS
DECEMBER 2019

"Limiting global warming to 1.5°C would require rapid, far-reaching and unprecedented changes in all aspects of society...With clear benefits to people and natural ecosystems, limiting global warming to 1.5°C compared to 2°C could go hand in hand with ensuring a more sustainable and equitable society...Global net human-caused emissions of carbon dioxide (CO2) would need to fall by about 45 percent from 2010 levels by 2030."

-The Intergovernmental Panel on Climate Change, Special Report on Global Warming of 1.5° C (press release)

TABLE OF CONTENTS

LIST OF FIGURES

LIST OF TABLES

ACKNOWLEDGMENTS

Thank you to my primary advisor Doug MacAyeal for all his support in developing my thesis and for supporting me in Chicago more generally. Thank you to Alison Banwell for the countless times she looked over my work and helped me improve it immeasurably. Thank you to David Archer and Mark Webster for serving on my committee and offering fresh perspectives and advice on my work. Thank you to David Mayer, who has served on my committee too, and to Ian Willis, for teaching me and being great collaborators. Thank you to Doug, Ali, Ian and Becky Goodsell for being amazing fieldwork teammates, I will never forget my time with I-190. Thank you to Brendan Hodge, Mike Cloutier and the countless workers that make the US Antarctic Program run and made our field project possible. Thank you to my officemates, and friends in the department and across the university for contributing to my time here. Thank you to all staff that have enabled me to work in a productive, safe and clean workspace. Thank you to everyone in Graduate Students United who is working to make the University of Chicago a better place to be and a more positive force in Chicago, and who helped to make me feel part of a positive community - we will win #BargainNow. Thank you to everyone who helped set me on the path to my PhD, notably my undergraduate advisor at Edinburgh, Pete Nienow, masters advisor at Cambridge, Neil Arnold and those that supported me at CEAZA. Especially thank you to my parents, Leigh Murray and John Macdonald, and my partner, Mariela Barajas, for everything - love yous. Thank you to Sally, Ollie, Betty and Napoleon Ferdinand for all they do. Thank you to everyone I forgot to thank.

For Chapter 2, which was published as Macdonald and others (2018), I acknowledge co-authors Alison Banwell and Douglas MacAyeal. I also thank Peter Langen of the Danish Meteorological Institute for providing surface runoff data.

For Chapter 3, which was published as Macdonald and others (2019), I acknowledge co-authors Alison Banwell, Ian Willis, David Mayer, Becky Goodsell and Douglas MacAyeal.

For Chapter 4, which is in preparation for publication, I acknowledge Douglas MacAyeal

and Alison Banwell for support.

For Chapter 5, which has been submitted for publication as Macdonald and others (in review), I acknowledge co-authors Predrag Popović and David Mayer. I also thank Jeff McMahon and my classmates in his writing class, who all helped improve the writing in this chapter.

All Landsat and Sentinel-2 images were downloaded for free from the United States Geological Survey's Earth Explorer website. MODIS images were observed in NASA's Worldview platform. The free, open-source GIS package, QGIS, and the Norwegian Polar Institute's Quantarctica package were valuable resources.

I acknowledge personal support from a NASA Earth and Space Sciences Fellowship (NNX15AN44H). This work was also supported by U.S. National Science Foundation grants PLR-1443126 and PLR-1841467.

ABSTRACT

Studies show that surface lakes that form on ice shelves can promote ice-shelf instability, which has consequences for wider ice-sheet stability. Meltwater on ice shelves will become increasingly pervasive due to climate change and it is therefore crucial that we improve understanding of ice-shelf hydrology and its implications for ice-shelf stability.

First, we use remote sensing to analyze the seasonal evolution of surface lakes on Petermann Glacier's floating ice tongue (a narrow ice shelf). Lakes start to form on the tongue in June and quickly peak in total number, volume and area in response to increases in air temperatures. However, despite sustained high temperatures, total lake number, volume and area decline through July/August. We suggest that rapid vertical lake drainage events, and evacuation of meltwater from lakes into the ocean via a surface river, limits water storage in lakes on the tongue. Additionally, mean areas of lakes on the tongue are calculated to be $\sim$20% of those on the grounded ice.

Second, we use remote sensing and field data to analyze and document the formation of pedestalled, relict lakes ('pedestals') that develop on the debris-covered part of the McMurdo Ice Shelf, Antarctica. Pedestals form when a surface lake that develops in the summer, freezes-over in winter, resulting in the lake-bottom debris being masked by a high-albedo, ice surface. If this ice surface fails to melt during a subsequent melt season, it experiences reduced surface ablation relative to the surrounding debris-covered areas of the ice shelf. We propose that this differential ablation, and resultant hydrostatic and flexural readjustments of the ice shelf, causes the former lake's surface to become increasingly pedestalled above the surrounding ice shelf. The development of pedestals has a significant influence on the surface-energy balance, hydrology and, potentially, flexure of the ice shelf.

Third, we apply an elastic model to investigate the flexural effect of pedestal formation on ice shelves. Our idealized model results suggest that the stresses produced by the effect of pedestal formation on ice-shelf flexure are unlikely to be sufficiently high to cause fracturing or threaten ice-shelf stability. Only in cases where ice-shelf thickness is very low, and surface

ablation is sufficiently high (conditions which could become more common due to climate change), does the model suggest that ice-shelf fracturing would occur.

Fourth, we use remote sensing to analyze the formation of sea ice ponds from ice-shelf runoff, adjacent to the McMurdo Ice Shelf. Each summer, meltwater flows from the ice shelf onto the sea ice and forms large (up to 9 km^2) ponds. This is an undocumented mechanism for the formation of sea ice ponds. These ponds decrease the sea ice's albedo, thinning it, and we suggest the added mass of ice-shelf meltwater runoff causes the ice to flex, promoting sea-ice instability close to the ice front. As surface melting on ice shelves increases, we suggest that ice-shelf surface hydrology will have a greater effect on sea ice.

By improving understanding of ice-shelf hydrology and processes, this thesis will enable the scientific community to better predict the response of the polar ice sheets to climate change.

CHAPTER 1

INTRODUCTION

A crucial factor in determining the magnitude and rate of sea-level rise, which is set to have devastating effects for coastal communities across the world (Oppenheimer and others, in press), is how the Antarctic and Greenland ice sheets respond to climate change. The Antarctic Ice Sheet stores 58 m of potential sea level (Fretwell and others, 2013) and Greenland a further 7 m (Aschwanden and others, 2019). In Greenland, approximately 60% of recent mass loss has been directly due to melting, and the other 40% has been due to ice dynamical processes that cause increased ice velocity and retreat (Csatho and others, 2014; Enderlin and others, 2014; van den Broeke and others, 2016). In Antarctica, ice dynamical processes dominate recent mass loss (Mouginot and others, 2014; Rignot and others, 2014; Scheuchl and others, 2016; Shen and others, 2018). To predict the future sea-level contribution of the Antarctic and Greenland ice sheets, it is therefore key to improve our understanding of ice dynamical processes at the margins of the ice sheets, and how these processes respond to warming. An important factor in determining this response is the evolution of floating ice shelves, which surround ∼75% of the Antarctic perimeter (Bindschadler and others, 2011). In Greenland, ice shelves are present at the terminus of several glaciers in northern Greenland, typically in the form of 'floating tongues', a type of ice shelf that is narrow and often constrained by the walls of a fjord (Hill and others, 2018). Ice shelves (and ice tongues) exert a buttressing force on the grounded ice that feeds them, which can be removed or reduced by ice-shelf collapse or thinning, causing increased flow of upglacier grounded ice (Scambos and others, 2004; Joughin and others, 2014; Mouginot and others, 2014).

Recent studies have shown that meltwater is pervasive on ice shelves around Antarctica (Langely and others, 2016; Kingslake and others, 2017; Stokes and others, 2019). This meltwater is often stored in surface lakes, which have been shown to promote ice-shelf instability and potential break-up in three ways. First, the water in surface lakes typically has a lower albedo than the surrounding ice or snow, and so absorb more solar radiation, which causes

more melting through a positive feedback effect; a process often called 'enhanced lake-bottom ablation' (Tedesco and others, 2012). Second, meltwater from lakes can fill and propagate fractures downwards through the ice (i.e. 'hydrofracture', Weertman, 1973; van der Veen, 1998; 2007; Alley and others, 2005), though this process has yet to be directly observed through in-situ measurements on an Antarctic ice shelf. Third, when a lake fills or drains, a load is added or removed from the ice shelf, respectively. This change of load causes the ice shelf to flex, which may weaken it and promote fracturing (MacAyeal and Sergienko, 2013; Banwell and MacAyeal, 2015; Banwell and others, 2019).

With air temperatures rising due to climate change, meltwater on ice shelves will become increasingly pervasive (Trusel and others, 2015; Bell and others, 2018). Consequently, it is essential that we have more observations and greater understanding of the behavior and implications of ice-shelf hydrology. However, substantial gaps in our knowledge about ice-shelf hydrology still remain. For example, prior to this thesis, there were no studies of surface lakes on floating ice tongues in Greenland, of how surface lakes evolve on debris-covered ice shelves, or of how ice-shelf surface hydrology could interact with sea ice. This thesis begins to address those gaps, using remote sensing, fieldwork and modeling to investigate the surface hydrology of ice shelves, and its implications for ice-shelf stability.

In Chapter 2, originally published as Macdonald and others (2018), we analyze the seasonal evolution of surface lakes on the floating ice tongue that forms the terminus of Petermann Glacier, which drains north from the Greenland Ice Sheet. We use remote sensing to analyze Landsat 8 imagery to analyze inter- and intra-seasonal evolution of surface lakes on the floating tongue from 2014 to 2016, and also compare these surface lakes to those on the grounded part of Petermann glacier. Our analysis shows that lakes start to fill in June and quickly peak in total number, volume and area in late June/early July, in response to increases in air temperatures. However, despite sustained high temperatures through July and August, total lake number, volume and area decline through this period. These observations may be explained by the transportation of meltwater into the ocean by a large surface

river, and by lake drainage events on the floating tongue, resulting in the vertical routing of this surface ponded water into the ocean below via fractures. Further, as mean lake depth remains relatively constant during this time, we suggest that a large proportion of the lakes that drain do so completely, likely by rapid hydrofracture. Additionally, the mean areas of lakes on the tongue are calculated to be substantially smaller than those on the grounded ice and exhibit lower variability in maximum and mean depth, differences likely attributable to the contrasting formation processes of lakes in each environment.

In Chapter 3, originally published as Macdonald and others (2019), we analyze and document the formation of pedestalled, relict lakes ('pedestals') that develop on the debris-covered part of the McMurdo Ice Shelf, Antarctica. Landsat 7/8 and Moderate Resolution Imaging Spectroradiometer (MODIS) visible satellite imagery from 1999 to 2018 are analyzed alongside field observations from the 2016/2017 austral summer. On the debris-covered part of the ice shelf there is an active surface hydrology. Pedestals form there when a surface meltwater lake, which develops in summer, freezes-over in winter, causing the low-albedo debris at the lake bottom to be masked by a high-albedo ice surface. If this ice surface does not melt during a subsequent melt season, it experiences reduced surface ablation relative to the surrounding debris-covered areas of the ice shelf. We propose that this differential ablation, and resultant hydrostatic and flexural readjustments of the floating ice shelf, cause the former surface lake surface to become increasingly pedestalled above the lower topography of the surrounding ice shelf. Consequently, surface meltwater streams cannot flow onto these pedestalled features, and instead divert around them. We suggest that the development of pedestals has a significant influence on the surface-energy balance, hydrology, and potentially flexure, of the ice shelf; something which is explored further in Chapter 4.

In Chapter 4, we apply an elastic finite-element model to investigate the effect of pedestal formation and differential ablation on ice-shelf flexure and possible fracture. The model is set up with an idealized, high-albedo pedestalled lake, represented by a central area that does not undergo surface ablation. Adjacent to this pedestal is an area that undergoes a

defined amount of surface ablation. The model is run with different pedestal radius, ice thickness and ablation values. The results suggest that the stresses produced by the effect of pedestal formation on ice shelf flexure are unlikely to be sufficiently high to cause fracturing or threaten ice-shelf stability. Only in cases where ice-shelf thickness is very low, and surface ablation is sufficiently high, does the model suggest that ice shelf fracturing would occur. Although such conditions do not exist at present (as far as we are aware), it is possible that the necessary conditions for fracturing associated with pedestal formation could be met in the future at the McMurdo Ice Shelf, or elsewhere, as ice shelves thin due rising air and ocean temperatures.

In Chapter 5, submitted for publication and currently in review, we analyze the formation of sea ice ponds from ice-shelf runoff, adjacent to the McMurdo Ice Shelf. This is a previously undocumented mechanism for the formation of sea ice ponds. Landsat 8 and Sentinel-2 images are used to analyze the ponds from the 2015/2016 to 2018/2019 austral summers. Each summer, meltwater flows from the ice shelf onto the sea ice and forms large (up to 9 km^2) ponds. These ponds decrease the sea ice's albedo, which causes thinning. Additionally, we suggest the added mass of ice-shelf runoff causes the ice to flex, promoting sea-ice instability close to the ice front. As the presence of sea ice at the ice front can influence calving processes, these ponds could have consequences for the ice-shelf's stability. As surface melting on ice shelves increases, ice-shelf surface hydrology is expected to come to have a greater influence on sea-ice surface hydrology and stability.

By improving our knowledge and understanding of ice-shelf surface hydrology, and the implications of ice-shelf hydrology for ice-shelf stability, this thesis enables better predictions of the response of ice shelves, and therefore ice sheets, to climate change. Ultimately, this will contribute to the effort to improve and constrain predictions of sea-level rise, which are essential for policymakers and communities defending themselves from the effects of climate change.

CHAPTER 2

SEASONAL EVOLUTION OF SURFACE LAKES ON A FLOATING ICE TONGUE, PETERMANN GLACIER, GREENLAND

2.1 Introduction

Surface lakes are known to affect the stability of ice shelves, which have an important buttressing effect on outlet glaciers around ice sheets (e.g. Scambos and others, 2004; Dupont and Alley, 2005; De Rydt and others, 2015). Therefore, surface lakes on ice shelves are likely to play an important role in the response of ice sheets to climate change, with recent studies suggesting that surface meltwater could become a primary factor in the future demise of Antarctica's ice shelves (e.g. DeConto and Pollard, 2016).

Around the north coast of the Greenland Ice Sheet (GrIS), numerous outlet glaciers terminate in narrow floating ice shelves, situated in confined fjords; features that we call 'tongues' in this study. In comparison, Antarctic ice shelves are more typically present in wider embayments. However, as the floating glacier ice in both environments is commonly constrained by embayment walls, both are typically subject to stress at their lateral margins and exhibit shear profiles in their seaward velocity. Although the magnitudes of these shear stresses will differ, floating ice shelves and tongues are considered similar in their form and environmental setting.

Although recent research has shown that numerous Antarctic ice shelves experience surface melting sufficient to enable widespread surface stream and lake formation (Langley and others, 2016; Lenaerts and others, 2016; Bell and others, 2017; Kingslake and others, 2017), to our knowledge, no studies of surface lakes on the floating tongues around the GrIS exist. Therefore, our prior knowledge of the evolution and effects of surface lakes on the stability of the floating glacier ice around Greenland comes from previous studies of surface lakes on

Antarctic ice shelves.

Around the Antarctic Ice Sheet (AIS), surface lakes on ice shelves have been shown to promote ice-shelf instability and potential break-up in three ways. Surface lakes can: i) fill and propagate fractures downwards through the ice (i.e. 'hydrofracture', Weertman, 1973, Alley and others, 2005; van der Veen, 1998; 2007), enabling them to drain rapidly (Gilbert and Domack, 2003; Banwell and others, 2013; Scambos and others, 2000; 2003); ii) act as time-dependent loads, which can cause a flexural response of the ice shelf, thereby weakening the ice shelf (MacAyeal and Sergienko, 2013; Banwell and MacAyeal, 2015); and iii) have a positive feedback effect on surface melt rates through enhanced lake-bottom ablation due to the lower albedo of water compared to the surrounding ice/snow (Tedesco and others, 2012).

While surface lakes on grounded ice form in depressions that reflect bedrock topography and ice flow conditions (Echelmeyer and others, 1991; Sergienko, 2013), surface lakes on floating ice shelves develop within surface topographic undulations that form in response to a variety of processes, including: i) basal crevassing (McGrath and others, 2012) and channelling (Le Brocq and others, 2013); ii) grounding-line flexure (e.g. Walker and others, 2013); and iii) incomplete flexural rebound from previous lake drainage events that often result in the formation of 'dolines' (Glasser and Scambos, 2008; Banwell and MacAyeal, 2015). This means that in contrast to surface lakes on grounded ice that remain in a fixed inter-annual location (Thomsen and others, 1988; Selmes and others, 2011), surface lakes on floating ice usually advect with ice flow (Banwell and others, 2014; Langley and others, 2016). Alternatively, surface lakes on ice shelves may form in 'pressure rolls' associated with compressive stress at the boundaries between floating ice and land. Consequently, surface lakes in these pressure rolls will migrate at a speed and direction that differs from ice flow (LaBarbera and MacAyeal, 2011). In addition to the presence of a surface topographic depression, lake formation on floating or grounded ice requires a surface of bare ice or firn that is sufficiently impermeable to enable water to pond (Scambos and others, 2000; Banwell and others, 2012; Lenaerts and others, 2016; Bevan and others, 2017).

Although various studies have suggested that surface lakes on Antarctic ice shelves may have drained rapidly by hydrofracture, such as on the Larsen B Ice Shelf (Scambos and others, 2003; Glasser and Scambos, 2008; Banwell and others, 2013), no direct observations exist. The quickest observed surface lake drainage event on an ice shelf took 5 days (Langley and others, 2016), however the precision of this drainage time is likely to be limited by the return-time of satellite imagery. Based on the physics of the hydrofracture mechanism (e.g. Weertman, 1973; Alley and others, 2005; van der Veen, 1998; 2007), lake drainage through this process is likely to occur over the order of a few hours on floating ice (Banwell and MacAyeal, 2015), comparable to the time that this process has been observed to take on the grounded ice of the GrIS (e.g. Das and others, 2008; Tedesco and others, 2013). Alternatively, surface lakes on Antarctic ice shelves have been observed to drain more slowly by overspilling their basins. Lakes may also only partially drain, or not drain at all, and re-freeze (Langley and others, 2016) and/or become covered in snow at the end of the summer (Koenig and others, 2015; Lenaerts and others, 2016).

For both the AIS and GrIS, the loss of the buttressing forces provided by floating ice shelves and tongues has been observed and modelled to significantly increase upstream outlet glacier flow speeds. For example, the collapse of Antarctica's Larsen B Ice Shelf in 2002 caused a multi-annual six-fold increase in speed, grounding-line retreat, and thinning of tributary glaciers feeding it (Scambos and others, 2004; Rignot and others, 2004; Rott and others, 2011; De Rydt and others, 2015; Wuite and others, 2015). Similarly, the loss of 95% of north Greenland's Zachariae Isstrom's ice shelf between 2002 and 2014 caused the glacier's flow rate to almost double (Mouginot and others, 2015).

Given the importance of the buttressing force of ice shelves against inland ice, and the clear link between ice shelf surface lakes and stability that has already been established in Antarctica, this study presents the first analysis of surface lakes on one of Greenland's floating tongues.

Focusing on Petermann Glacier, northwest Greenland, our first objective is to analyse the

inter- and intra-seasonal evolution in the overall pattern of lakes on its floating ice tongue over three consecutive melt seasons, 2014, 2015 and 2016. Our second objective is to focus more specifically on the inter- and intra-seasonal evolution of two individual surface lakes that repeatedly fill and drain during the three melt seasons. And finally, to help determine the extent to which our extensive knowledge of surface lakes on the GrIS's grounded ice can be applied to surface lakes on floating tongues, our third objective is to compare the characteristics of a subset of surface lakes on the floating tongue to surface lakes on the grounded ice of Petermann Glacier during June 2014.

2.2 Study Site

Petermann Glacier (Fig. 2.1), northwest Greenland (81°N), drains ∼4% of the ice sheet northwards into Petermann Fjord (Münchow and others, 2014). It terminates in a floating tongue that had an area of ∼1000 km^2 as of 2016. As is typical of floating tongues and ice shelves, it has a low surface gradient; the elevation change is only ∼40 m over a distance of ∼40 km from the ice front to the grounding line. Ice thickness varies across the tongue, but ranges from ∼600 m by the grounding line to <100 m close to the terminus (Münchow and others, 2014). It is one of only seven glaciers in Greenland with a permanently floating tongue, all of which are located on the north coast (Moon and others, 2012).

The glacier lost ∼40% of its tongue in two massive calving events in 2010 and 2012, and its terminus is now at its most retreated position since records began (Nick and others, 2012; Mnchow and others, 2014). These large calving events, however, did not cause a significant change in the velocity or thickness of the glacier (Nick and others, 2012), and research suggests that the grounded glacier is currently dynamically stable. Its grounding line is at ∼600 m below sea level on a forward slope, and the bed remains below sea level up to ∼80 km inland of the grounding line (Rignot, 1998; Bamber and others, 2013). Although the position of the grounding line has varied by an average of 470 m between 1992 and 2011 (with a maximum range of 7 km), it experienced no systematic retreat or advance (Hogg

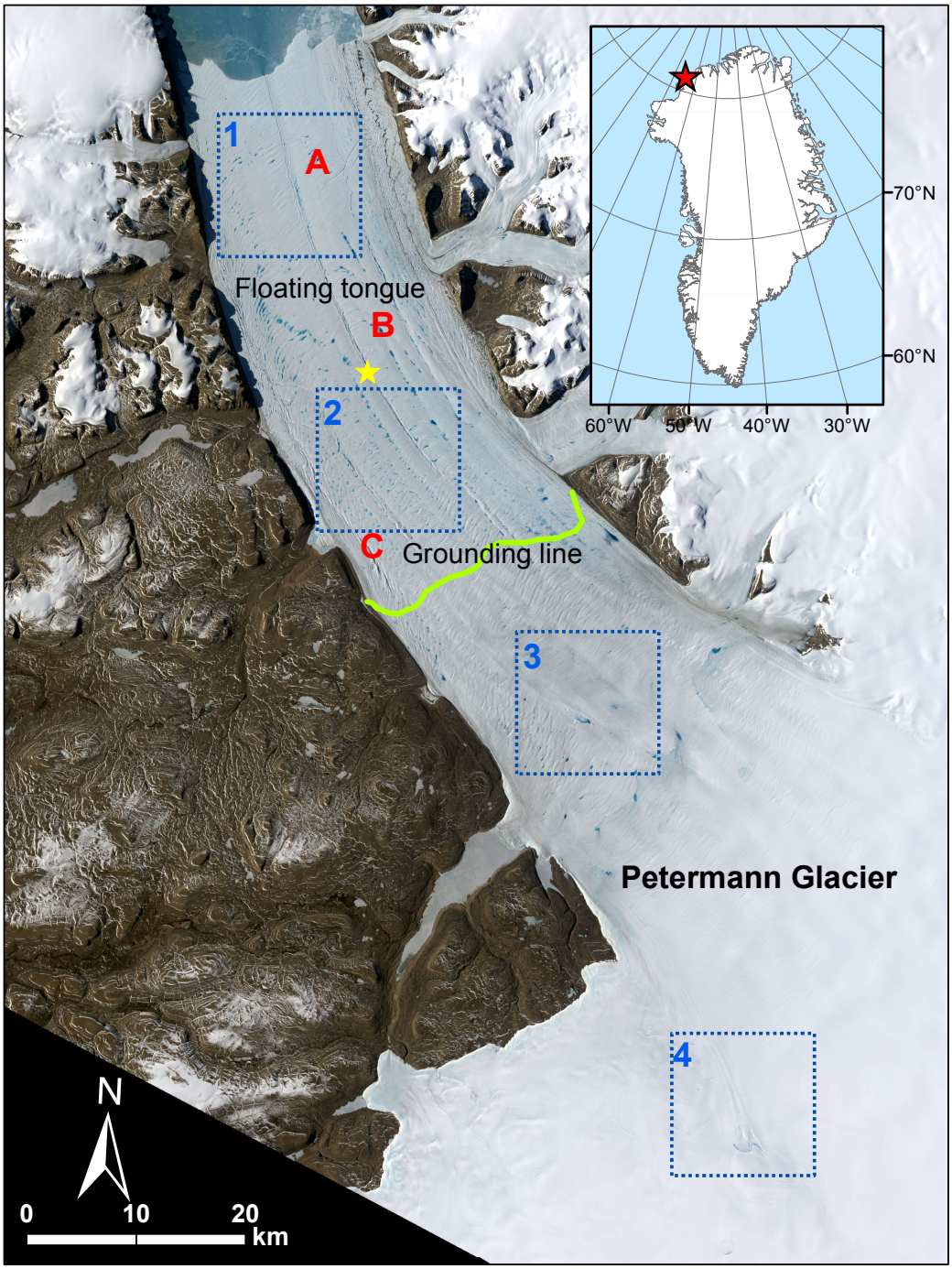

Fig. 2.1: The study site, Petermann Glacier, northwest Greenland, shown in a pan-sharpened true colour Landsat 8 OLI image, dated 18 June 2016. The approximate grounding line position (following Rignot, 1998) is shown by the green line. The letters A, B, and C indicate the locations of lakes shown in Figures 2.8 and 2.9, and the numbers 1-4 indicate the location of the subsampled areas used to compare surface lakes on the floating and grounded ice in Figures 2.10 and 2.11. The yellow star indicates the location of the $\sim$5.5 km^2 pixel from HIRHAM5's output used to represent daily mean surface temperature.

and others, 2016). However, this does not preclude the potential for future changes in the glacier's velocity and mass balance in response to tongue break-up events (Nick and others, 2012; Hogg and others, 2016).

For the GrIS as a whole, the average daily melt during the summers of the study period 2014-16 was largely unremarkable compared to the preceding decade, but continued the overall trend of increased melting (Tedesco and others, 2014; 2015; 2016). Additionally, data from an ice-sheet wide network of weather stations (PROMICE) suggests that net ablation, especially in northern regions, has been larger in recent years (2008-2015) than during any period in the previous ∼150 years (van As and others, 2016).

2.3 Data and Methods

2.3.1 Satellite image acquisition and processing

All Landsat 8 Operational Land Imager (OLI) images of Petermann's floating tongue that were either completely or partially cloud-free for the boreal summers (i.e. June to August) of 2014, 2015 and 2016 were downloaded from the EarthExplorer website (Table 2.1 and 2.2).

OLI imagery was partly chosen for its high spatial resolution (30 m), compared to, for example, Moderate Resolution Imaging Spectroradiometer (MODIS) imagery; the resolution (250 m) of which precludes such accurate lake identification and volume analysis. OLI imagery also does not have the missing scanlines of Landsat 7 Enhanced Thematic Mapper Plus (ETM+), and therefore we choose to study the three summers succeeding the launch of Landsat 8. Compared to ETM+, OLI also has enhanced radiometric resolution (12 bit compared to 8 bit), and features narrower multispectral and panchromatic bands, allowing for improved lake-identification and lake-depth estimation. Additionally, OLI has a higher temporal acquisition rate than ETM+ and although it has a 16-day revisit time, overlap between orbits means that images of the study site were sometimes acquired for consecutive

days.

Once acquired, images were cropped to the area of interest in ArcMap^{TM}. Subsequently, the upglacier boundary of the floating tongue was defined, based on the position of the grounding line estimated by Rignot (1998). As mentioned above (Section 2.2), although the grounding line position has varied over the last three decades, it has not systematically retreated or advanced, and thus this grounding line position is considered a best estimate for this study.

2.3.2 Seasonal evolution of surface lakes (2014-2016) (objective i)

To conduct analysis of the inter- and intra-seasonal evolution of surface lakes (2014-2016), only images that were completely cloud-free over the tongue (15 images in 2014, 18 in 2015 and 24 in 2016) were used (Table 2.1). Following processing (Section 2.3.1), a mask of surface lake boundaries in each image was produced in MATLAB^{TM} using a lake boundary/area algorithm, following the method of Banwell and others (2014), which is based on the algorithm developed by Box and Ski (2007) (see Section 2.7.1 for further details). From the masks, total lake number (TLN) and total lake area (TLA) were calculated for each image in each of the three melt seasons. Next, following the method of Sneed and Hamilton (2007) and Banwell and others (2014), but adapted for OLI instead of ETM+ (Pope and others, 2016), a lake-depth algorithm was applied to calculate the water depth of all pixels previously identified as being part of a lake (see section 2.7.2 for further details). Using these results, total lake volume (TLV) and mean lake depth (MLD) for each image was calculated.

Next, to analyse the inter- and intra-seasonal evolution of TLN, TLV, TLA and MLD in response to air temperature and thus surface melt conditions on the floating tongue, these four calculated statistics were compared to both the surface air temperature and surface runoff products from the Danish Meteorological Institute's (DMI)'s HIRHAM5 regional climate model for all years. These data were sourced from HIRHAM5' s daily meteorological re-analysis product for 2014 (documented in Langen and others, 2017) and the operational

product for 2015 and 2016 (as the reanalysis product for 2015 and 2016 was not yet available at the time of our study). A single ∼5.5 km^2 cell, located mid-way up the tongue (at 60.6°W, 80.7°N, Fig. 2.1), from the DMI's model output was used to represent mean daily air temperatures of the tongue throughout the study period. This was deemed acceptable as the magnitudes and seasonal trends in runoff (and therefore air temperatures) across the relatively flat tongue do not show significant variation (Fig. 2.2). Additionally, for each year, HIRHAM5's surface runoff product was used to analyze the mean daily surface runoff across the tongue for the periods 1-15 June, 16-30 June, 1-15 July, 16-31 July, 1-15 August, and 16-31 August. There is no observational weather data available for the region during the study period with which to facilitate an assessment of HIRHAM5's validity in the study area. However, HIRHAM5's overall performance has been validated against observations from the PROMICE network of automatic weather stations across the GrIS (Langen and others, 2015; 2017), and we regard this validation sufficient for the present study.

2.3.3 Seasonal evolution of individual surface lakes (2014-16) (objective ii)

To analyse the inter- and intra-seasonal evolution of individual lakes, with a specific focus on their filling and drainage patterns, two lakes that were observed to fill and drain from a sequence of high-temporal resolution imagery were chosen (Lakes A and B, locations indicated in Fig. 2.1). This analysis made use of images that were completely cloud-free over the tongue and also the images that were at least cloud-free at the sites of the specific lakes (15 images for Lake A, 33 for Lake B; Table 2.2). All selected images were cropped to only include Lake A or B, and lake volumes in each image were calculated using the lake boundary/area and depth algorithms. A lake was deemed to have drained 'rapidly' if >90% of volume drained within 48 hours (Selmes and others, 2011), or 'slowly' if drainage exceeded this time. Finally, to include examples of lakes that do not drain in our analysis, two cloud-free images of a group of lakes that freeze-over and/or are buried by snow were analysed by manual visual interpretation (location indicated by C in Fig. 2.1).

2.3.4 Comparison of surface lakes on the floating tongue and grounded ice (objective iii)

To compare surface lakes on the floating tongue with those on the grounded ice, four equally-sized areas (187 km^2 were selected, two of which are located on the tongue (Sites 1 and 2 in Fig. 2.1,) and two on the grounded ice (Sites 3 and 4 in Fig. 2.1). An OLI image dated 30 June 2014 was used to analyze surface lakes within Sites 2, 3 and 4, but as Site 1 did not fall within this image, an OLI image captured 3 days earlier (27 June 2014) was instead used for this site. These images from late June were chosen because it was then that surface lakes were widespread on both the floating tongue and the upglacier grounded ice, and there was no single cloud-free image that included all four sites around this time.

The two images were cropped to each site's area of interest and the lake boundary/area and lake-depth algorithms were used to calculate the maximum and mean depths, and areas, for surface lakes in each site. The results from the two floating tongue sites (1 and 2) and two grounded sites (3 and 4) were each combined into 'floating' and 'grounded' sets of results, respectively, and were quantitatively compared.

2.4 Results

2.4.1 Inter- and intra-seasonal evolution of meltwater features on the floating tongue (2014-16)

In each of the three melt seasons studied, surface lakes first start to develop on the tongue in early June, before rapidly increasing in total number, volume, area and density over the following days and weeks (Fig. 2.3). For example, in just one day (11-12 June 2016) TLN, TLA and TLV increase by 173%, 270% and 248%, respectively (Figs. 2.3 and 2.4). Mean daily temperatures $>0^{\circ}C$ are also first recorded in the first half of June each year. Peak TLN, TLA and TLV are reached in late June or early July in each year, but these peaks

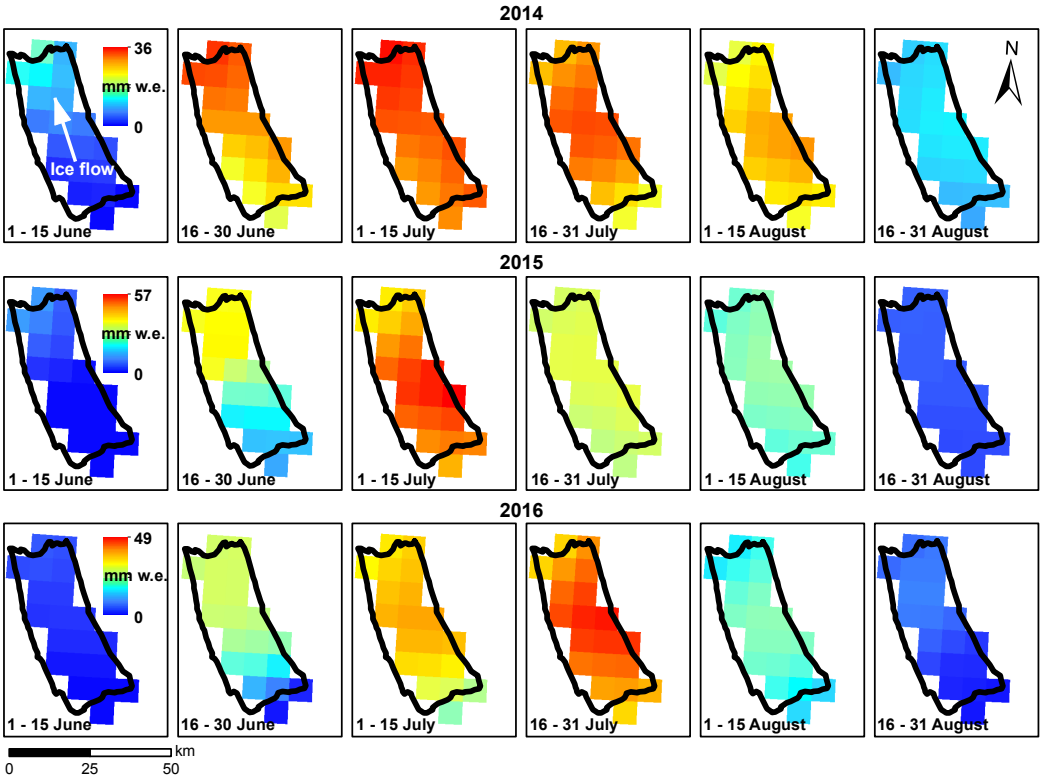

Fig. 2.2: Mean daily surface runoff (mm w.e.) through the 2014, 2015 and 2016 melt seasons. Petermann's floating tongue is shown by the black outline. Plots within each year have the same colour bar scale.

do not always occur simultaneously. Following these times, TLN, TLA and TLV decline throughout the rest of the summer, though some fluctuations around this trend do occur. Conversely, air temperatures peak in July or August, and the longest continuous periods of daily mean temperatures >0°C occur in these months, while TLN, TLA and TLV decline (Figs. 2.3 and 2.4). In contrast to TLN, TLA and TLV, MLD does not decline through July and August. Instead, after rising through June/early-July, MLD then becomes relatively stable (1-1.5 m) until the end of the season (Fig. 2.3).

Surface lake development varies spatially across the tongue during each melt season (Fig. 2.5). Surface lakes evolve upglacier in both 2015 and 2016 (unfortunately, there is insufficient imagery during 2014 to evaluate this phenomenon). For example, between 16 June and 4 July 2015 (Fig. 2.5), the areal extent of surface lakes declines on the lower part of the tongue, but increases in the upper ∼18 km, close to the grounding line. A similar pattern

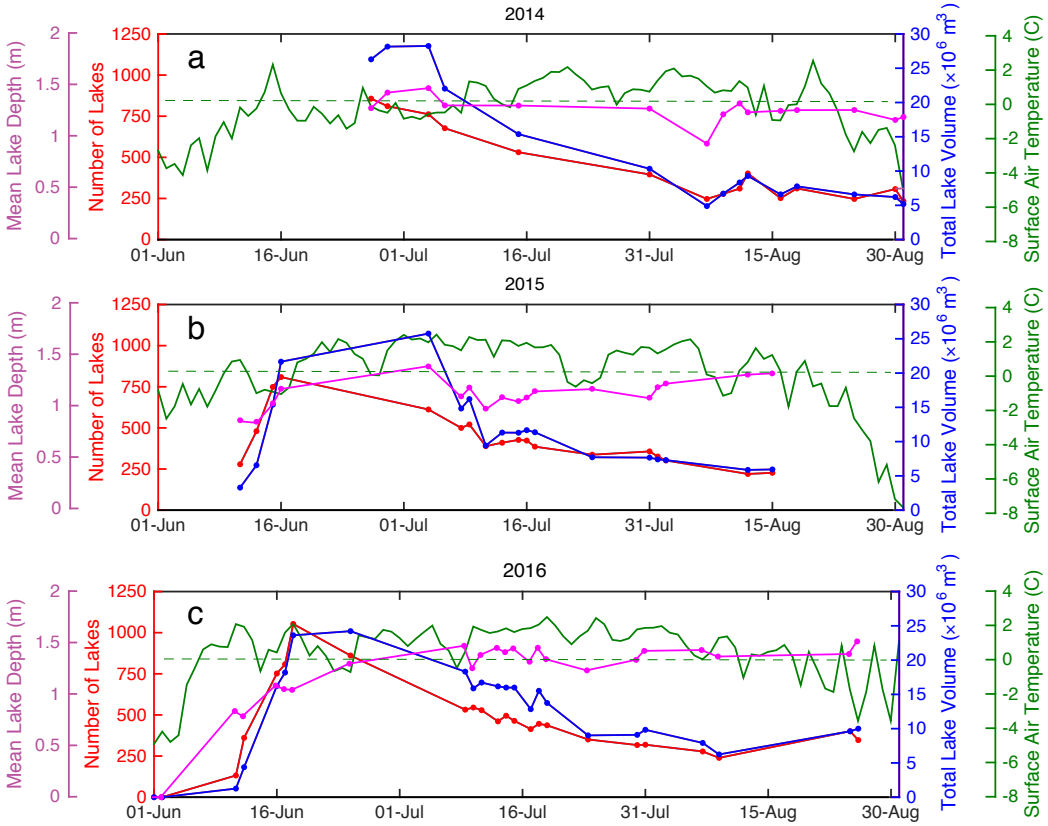

Fig. 2.3: Total lake number (TLN, red), total lake volume (TLV, blue), mean lake depth (MLD, purple) and daily mean surface air temperature (green) on Petermann's floating tongue in (a) 2014, (b) 2015, and (c) 2016.

is observed between 18 June and 25 June 2016. In both cases, this pattern of surface lake expansion close to the grounding line is concurrent with an overall decrease in TLN, and an overall increase in TLV and MLD across the whole tongue (Fig. 2.3) (TLA slightly increases over this period in 2015 but decreases in 2016; Fig. 2.4). In each year, higher runoff values spread upglacier as runoff increases. The location of each peak runoff also moves closer to the grounding line through June and July (Fig. 2.2).

At the time of peak TLA (Fig. 2.4), the area of the tongue covered by surface lakes in 2014, 2015 and 2016, is 2.5%, 2.3%, and 2.8%, respectively. The warmest melt season out of the three studied is 2016, with a mean temperature of 0.65°C, and the coldest melt season is in 2014, with a mean temperature of -0.06°C (Fig. 2.3). Not surprisingly, 2016 also has the greatest number of days (69) with a mean temperature >0°C, and the earliest day (7 June)

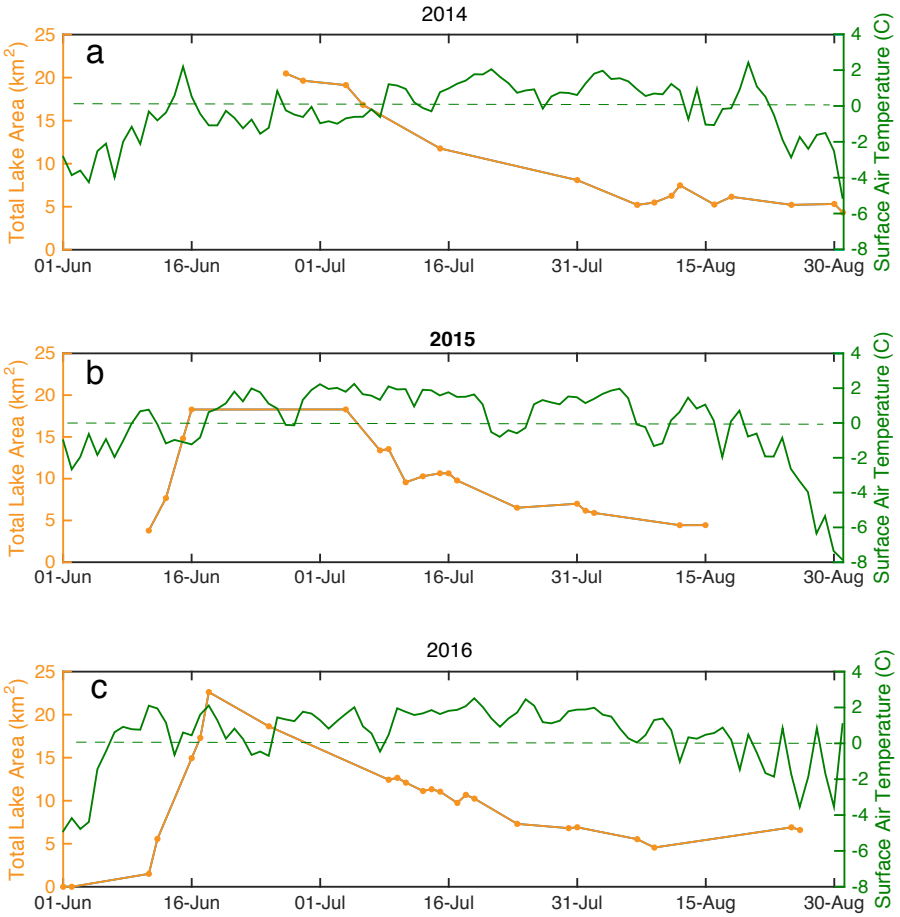

Fig. 2.4: Variations in total lake area (TLA, orange) and daily mean surface air temperature (green) on Petermann's floating tongue in (a) 2014, (b) 2015 and (c) 2016.

with a mean temperature >0°C. In contrast, 2014 has the smallest number of days (41) with a mean temperature >0°C and the latest day (14 June) with a mean temperature >0°C. Further, 2016 records the highest TLN (1053 lakes) and TLA (22.62 km^2), and earliest peak TLV (24.22 x 106 m^3). However, although 2014 records the lowest mean temperature, it has the highest peak TLV (28.24 x 106 m^3, which occurs 9 days later than in 2016).

While the pattern of lake distribution across the tongue appears broadly similar in each year, there are small inter-annual differences in surface lake locations due to ice flow (Fig. 2.6). During our study period, surface lakes migrate downglacier with ice flow at ∼1.2 km a^{-1}, which is comparable with the velocity observations made by Nick and others (2012)

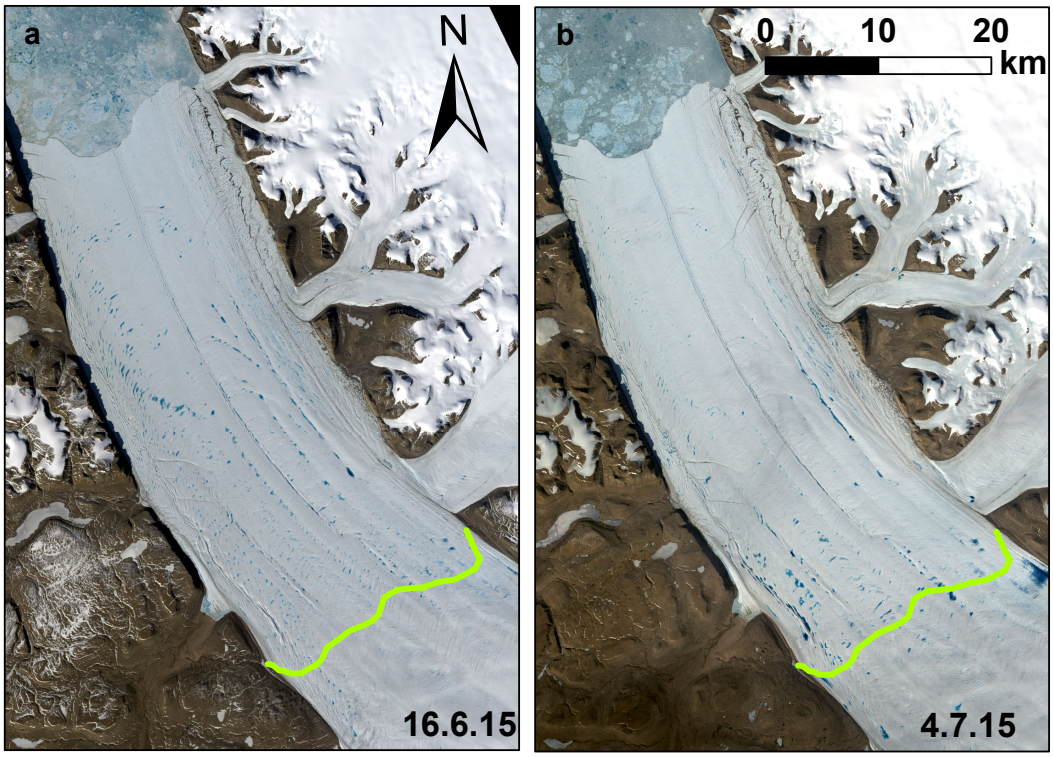

Fig. 2.5: The floating tongue on (a) 16 June and (b) 4 July 2015 in pan-sharpened OLI images. Note the increase in surface lake coverage close to the grounding line (green) between the images, while many surface lakes closer to the terminus have drained.

(1.1-1.4 km a^{-1}).

We also note that in each melt season, a surface river forms along the centre-line of the tongue and terminates at the ice front (Fig. 2.7), which is likely the same river identified in 2014 by Bell and others (2017). The river is visible in imagery between 27 June and 18 August 2014, 11 June and 14 August 2015, and 11 June and 9 August 2016. Each year, it reoccupies the same central channel that was observed by Münchow and others (2014), identified as an area of low ice thickness. Each summer, the river begins its activity on the same date that surface lakes are first identified (mid-late June). On 15 July 2016, a meltwater plume is visible in the ocean where the river terminates at the ice-front (Fig. 2.7d). In all three melt seasons, the river remains active until it empties in mid-late August.

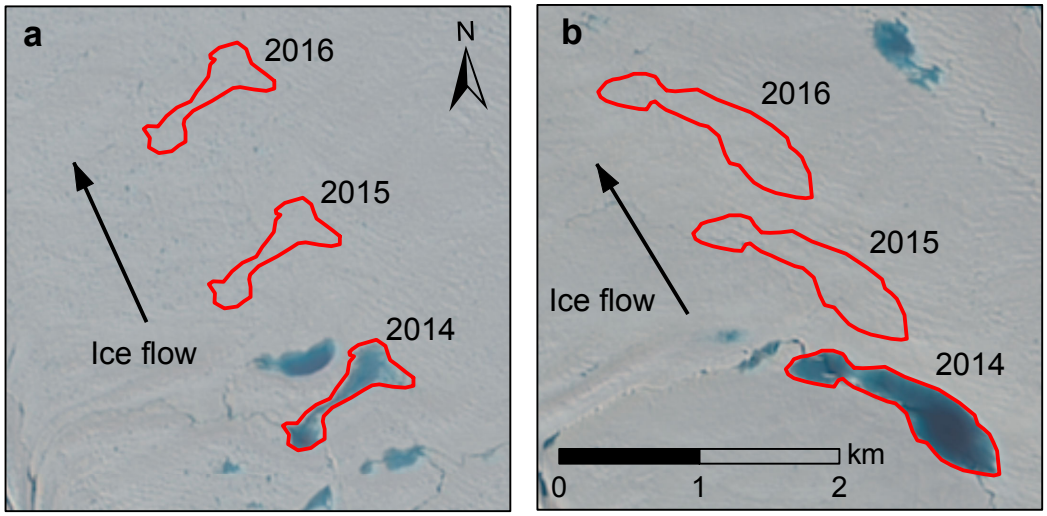

Fig. 2.6: The downglacier inter-annual migrations of Lakes A and B between 2014 and 2016. (a) Lake A and (b) Lake B on 24 June 2014 and their positions on 16 June 2015 and 18 June 2016. The background of both panels is an OLI image dated 24 June 2014.

2.4.2 Individual lake development and drainage on the floating tongue (2014-16)

Following lake development in early June in all three years, surface lakes generally expand in area, coalesce with nearby lakes, and then drain or become covered by snow or ice. We observe two instances of surface lakes draining 'rapidly', both in 2014 (Figs. 2.8a-b and 2.6). For example, between 24 and 25 June 2014, Lake A loses 96% of its 12.37 x 104 m^3 volume, and the remainder drains over the following day (Fig. 2.9a). The same lake, however, does not drain as rapidly in other years, taking >4 days to drain in 2015 and >6 days to drain in 2016 (Fig. 2.9a). Lake B also drains rapidly between 25 and 27 June 2014, when it loses 32% of its volume after one day and 92% after two days (Fig. 2.9b). Like Lake A, Lake B also does not drain as rapidly in other years, taking >18 days to drain more than 90% of its volume in 2015 and >7 days in 2016 (Fig. 2.9b). Many surface lakes, such as Lakes A and B in 2015 and 2016, drain slowly over several days to weeks by overflow into surface channels. Some of these surface lakes drain fully and others only partially. Finally, many other surface lakes do not drain at all, especially those close to the grounding line, such as

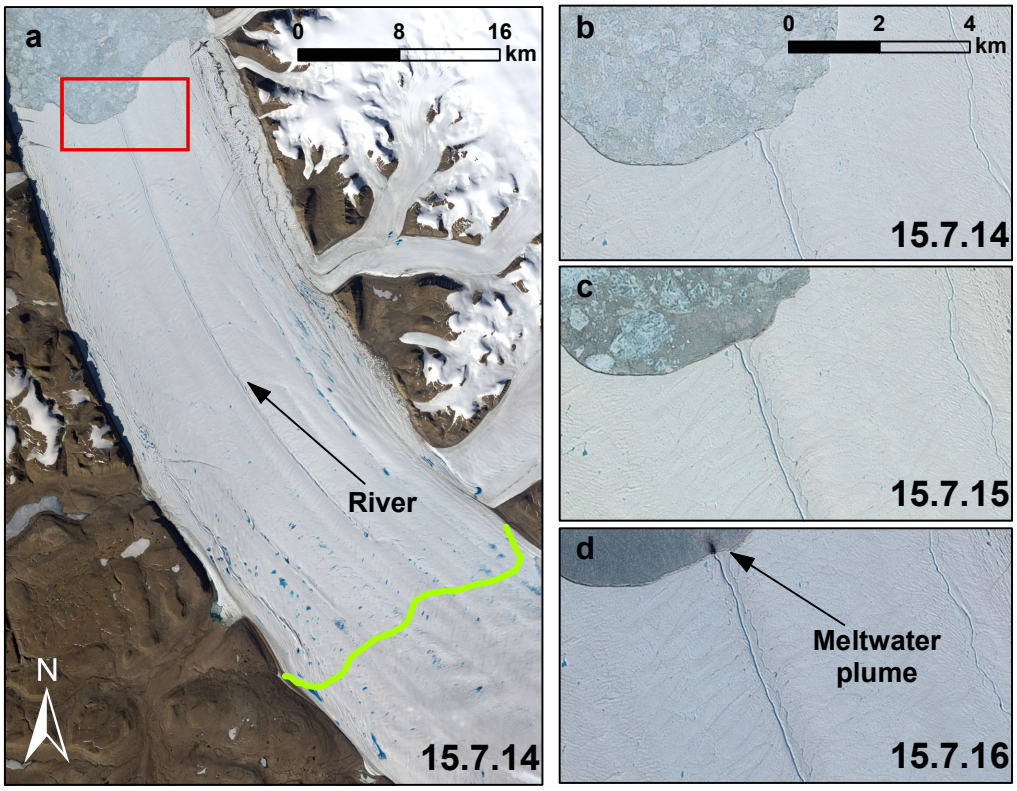

Fig. 2.7: The active river that forms annually down the centre-line of Petermann's floating tongue and terminates in the ocean. The whole tongue is shown on 15 July 2014, and just the terminus area is shown on 15 July in (b) 2014, (c) 2015 and (d) 2016 in pan-sharpened OLI images. The red box shows the location and extent of (b-d) and the green line indicates the location of the grounding line (following Rignot, 1998). Note the visible meltwater plume in the ocean where the river terminates in 2016 (d).

those at location C (Fig. 2.1), and instead freeze-over and/or are buried by snowfall events in late August and early September (Fig. 2.8c).

2.4.3 Comparison of lakes on floating ice with those on grounded ice

Compared to surface lakes on the floating tongue (Fig. 2.10), those on the grounded ice have a larger mean area of 0.140 km^2 (standard deviation: 0.228 km^2) and a larger median area of 0.025 km^2 (Fig. 2.11). In contrast, surface lakes on the floating tongue have a mean area of 0.025 km^2 (standard deviation: 0.033 km^2) and a median area of 0.013 km^2 (18% and 52% of the values for grounded surface lakes, respectively). Surface lakes on the grounded

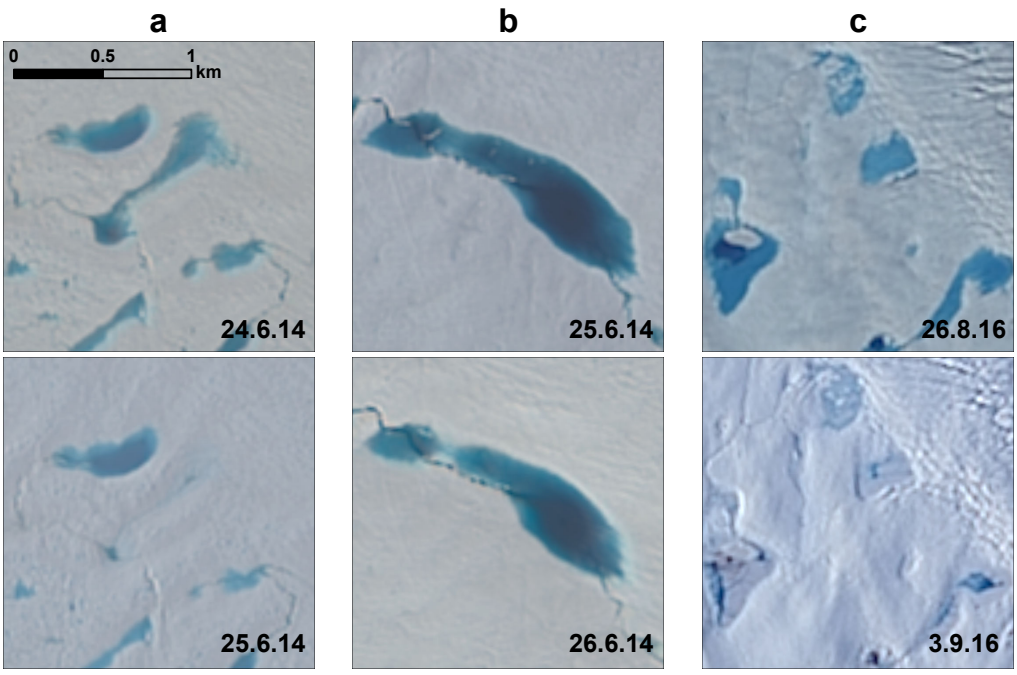

Fig. 2.8: Examples of lake drainage and burial/freeze-over events. Lake locations are indicated in Figure 2.1. (a) Lake A on 24 and 25 June 2014, before and after the rapid lake drainage event shown in Figure 2.9a. (b) Lake B on 25 and 26 June 2014, during the rapid lake drainage event shown in Figure 2.9b. (c) A group of lakes (C) that become buried by snow and ice between 26 August and 3 September 2016.

ice also reach a much higher maximum area (1.329 km^2) than those on the floating tongue (0.277 km^2).

Surface lakes on the grounded ice do not exhibit a large difference in depth characteristics compared to those on the floating tongue (Fig. 2.11). Surface lakes on the grounded ice are generally only slightly deeper, with a mean depth of 0.99 m, compared to 0.98 m on the floating ice. Surface lakes on the grounded ice also have a higher spread of depth values, with standard deviations of 0.86 m and 0.49 m for maximum and mean depth, compared to 0.72 m and 0.40 m, respectively, on the floating ice.

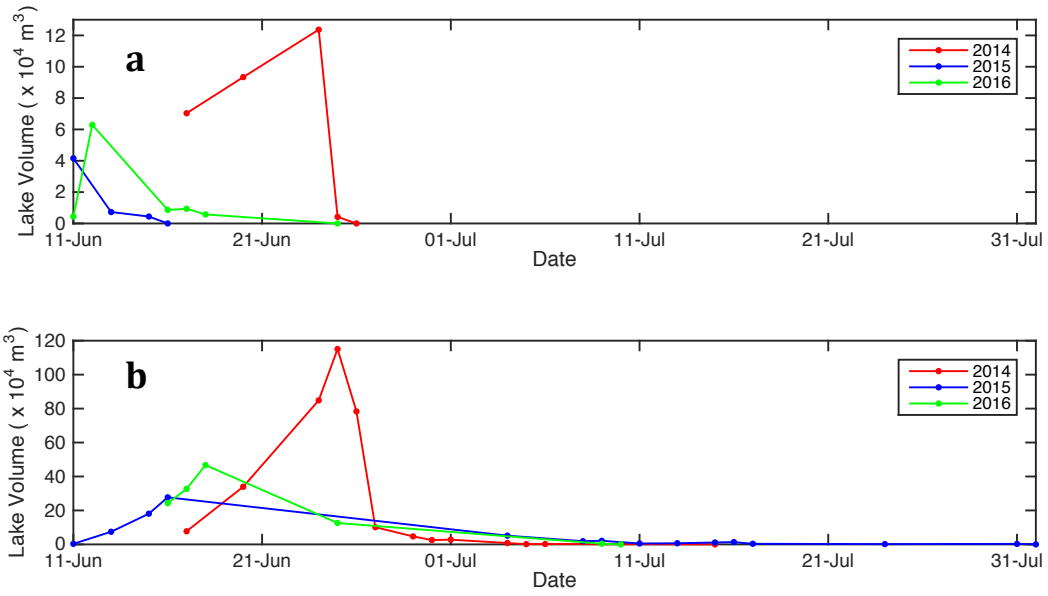

Fig. 2.9: Development and drainage of lakes (a) A, and (b) B, 2014-2016. In 2014, Lakes A and B drain 'rapidly', with Lake A losing 96% of its volume in one day and Lake B losing 30% of its volume one day, followed by a further 61% of its peak volume over the following day. Lakes A and B both drain 'slowly' in 2015 and 2016.

2.5 Discussion

2.5.1 Inter- and intra-seasonal evolution of meltwater features on the floating ice (2014-16)

We observe inter-seasonal variations in all the lake-related statistics that we calculate; TLN, TLA, TLV and MLD (Figs. 2.3 and 2.4), but, as with previous studies of surface lakes on grounded ice (Liang and others, 2012; Leeson and others, 2013), we observe no clear inter-seasonal relationship between our calculated surface lake statistics and air temperature. Strong inter-seasonal variations linked to air temperature are especially unlikely at low-elevation sites such as this, close to the terminus, where the melt and surface conditions necessary for ponding are likely met in both warm and cold years (Liang and others, 2012), including all years in our study period. Further, it is likely that the lake basins fill to their maximum capacity in both warmer and cooler melt seasons, meaning that much of the extra meltwater produced in warmer years simply drains from the tongue, rather than increasing

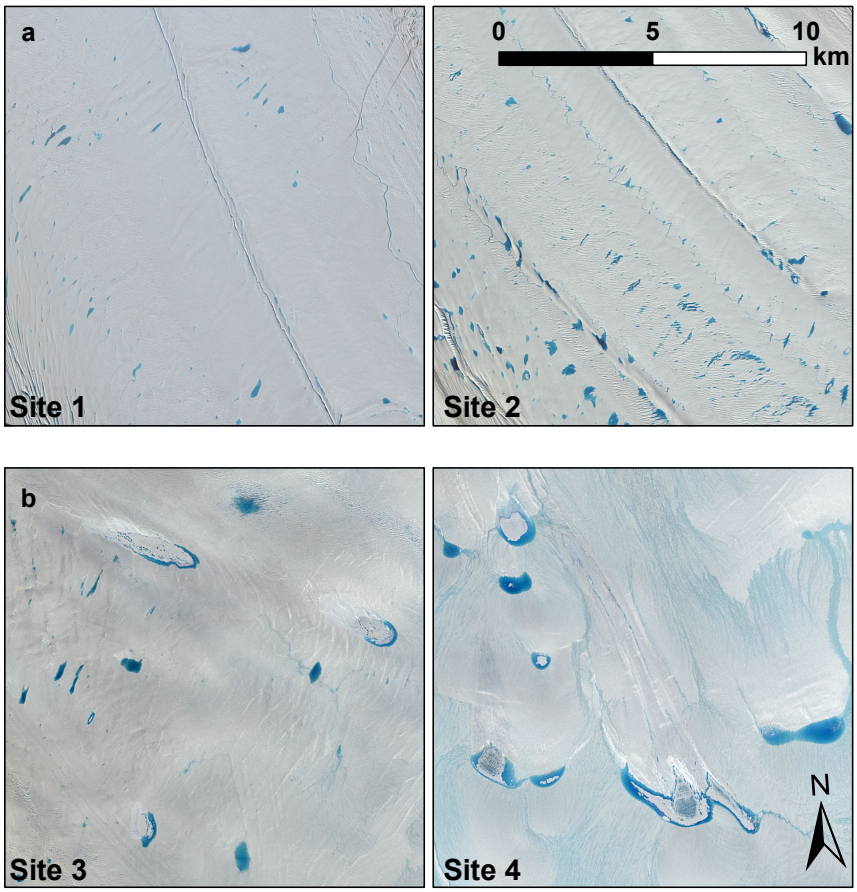

Fig. 2.10: A comparison of surface lakes on the a) floating tongue (Sites 1 and 2) and b) grounded region (Sites 3 and 4) of Petermann Glacier in pan-sharpened OLI images. Sites 1-4 are located at increasingly upglacier positions, as indicated in Figure 2.1, and the images were captured on 27 June 2014 for Site 1, and 30 June 2014 for Sites 2-4.

the volumes of surface lakes.

The rapid development of surface lakes once mean temperatures reach 0°C in each melt season portrays a high sensitivity to small changes in surface air temperature beyond a critical temperature threshold (Bartholomew and others, 2010). The rapid growth in TLV (Fig. 2.3) and TLA (Fig. 2.4) is further facilitated by the positive feedback between surface melting and lake growth associated with the low albedo of lake water compared to the surrounding ice/snow; a process which has been observed to enhance ablation <135% on the GrIS (Tedesco and others, 2012). Finally, as could be expected, surface lakes begin to develop later in the melt season than has been previously observed on warmer, lower

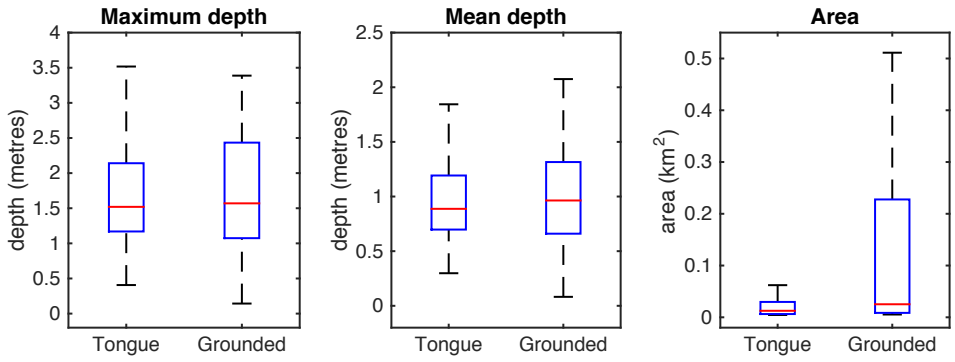

Fig. 2.11: Box plots of maximum depth, mean depth and area of surface lakes at two sites on Petermann's floating tongue (1 and 2, Fig. 2.1) and two sites on the grounded ice (3 and 4, Fig. 2.1). On each box, the red mark is the median and the edges of the box are the 25$^{\text{th}}$ and 75$^{\text{th}}$ percentiles (q1 and q3, respectively). The length of the whiskers (dashed lines) are equal to q3 + 1.5(q3 - q1). The measurements were made using OLI images from 27 June 2014 (site 1) and 30 June 2014 (sites 2-4) that are shown in Figure 2.10.

latitude glaciers of the GrIS. For example, surface lakes began to develop as early as May in the Paakitsoq region (∼69°N) in 2001 (McMillan and others, 2007) and at Russell Glacier (∼67°N) in 2007-2009 (Johansson and others, 2013).

From mid-late June until late June/early July, there is a decrease in TLN despite a continued increase in TLV (Fig. 2.3). The accompanying increase in MLD suggests that this occurs partly because multiple surface lakes coalesce into fewer deeper, larger surface lakes, and partly because some lakes completely drain while others increase in volume.

There are a few possible explanations for the overall decline of TLN, TLV and TLA from mid-late July, which shows no clear relationship with temperature. First, the concurrent relatively stable nature of MLD suggests that many surface lakes drain rapidly and completely, likely by hydrofracture (i.e. as slow/partial drainage would be associated with a decline in MLD). Though, notably, the stability of MLD alongside a decrease in TLN suggests that there is not a relationship between the depth of a lake on the tongue and its tendency to rapidly drain. Second, the meltwater plume (Fig. 2.7) suggests the central river likely efficiently evacuates meltwater over the ice tongue front, thereby reducing TLV in the latter part of the melt season. For example, Bell and others (2017) showed that a similar river had

an important role in exporting meltwater from the Nansen Ice Shelf, Antarctica.

The increased spatial coverage of surface lakes closer to the grounding line in late June and early July (Fig. 2.5), while overall TLN, TLA and TLV decline, can partly also be explained by the shift in peak volume of meltwater runoff from closer to the terminus towards the grounding line over a similar period (Fig. 2.2). Additionally, it can be partly explained by the inflow of surface meltwater from the upglacier grounded ice, as surface melting in higher-elevation areas likely only commences in the mid-late melt season once air temperatures are sufficiently high. Similar observations of meltwater from upglacier areas flooding floating portions have been made on the Nivlisen (Kingslake and others, 2015) and Roi Baudouin ice shelves (Lenaerts and others, 2016). We therefore suggest that surface melting on Petermann's grounded ice forms an important contribution to the surface hydrology of its floating tongue.

2.5.2 Individual lake development and drainage

Our observations of rapid (i.e. <48 hours) lake drainage on Petermann's floating tongue (Figs. 2.8a-b and 2.9) suggest that surface lakes likely drain vertically by hydrofracture, as previously discussed. The rapid drainage of Lakes A and B in 2014, but not 2015 and 2016 (Fig. 2.9) may be explained by the substantially higher peak lake volumes in 2014 ($\sim$3 x that of 2015, and $\sim$2 x that of 2016 for Lake A, and $\sim$4 x that of 2015, and $\sim$2 x that of 2016 for Lake B) (Weertman, 1973; Alley and others, 2005; van der Veen, 1998; 2007).

Slow drainage events (e.g. Lakes A and B in 2015 and 2016), and/or the freeze-over/burial of some lakes at the end of the season (e.g. Fig. 2.8c), on Petermann's tongue suggest that the preconditions for hydrofracture (e.g. the presence of a fracture (Das and others, 2008) or sufficient lake volume (Alley and others, 2005; van der Veen, 2007; Arnold and others, 2014)) may not exist for some surface lakes. Slow lake drainage events by surface overflow have been observed elsewhere on both grounded ice of the GrIS (e.g. Tedesco and others, 2013; Poinar and others, 2015) and floating ice of the AIS (e.g. Langley and others, 2016). Likewise,

the freeze-over and/or burial-by-snow of many surface lakes is also common elsewhere in areas such as East Antarctica (e.g. Langley and others, 2016) and higher-elevation regions of the GrIS (e.g. Koenig and others, 2015; Poinar and others, 2015). It is unclear whether these lakes on Petermann freeze-through or remain as englacial features, but in any case, the existence of such storage features limits further meltwater contribution to surface streams and lakes. Latent heat release from any freezing may affect the energy balance of the upper layers of snow/firn/ice (e.g. Humphrey and others, 2012).

2.5.3 Comparison of lakes on floating ice with those on grounded ice

The lower mean and maximum areas of surface lakes on the floating tongue, compared to those on the grounded ice (Fig. 2.11), can primarily be explained by the various processes that govern each set of lakes' formation. Meltwater on the tongue appears to pond in densely-spaced flow stripes, crevasses and surface undulations that form in response to ice flow, flexure and the ice crossing the grounding line, as previously observed on Antarctic ice shelves (e.g. McGrath and others, 2012; Banwell and others, 2014). This pattern of lake formation is particularly apparent on the floating ice close to the grounding line (Fig. 2.10a). Also, lake volumes on the tongue are relatively small due to the small catchment areas of each lake, a function of the low gradient of the tongue (Banwell and others, 2014). In contrast, meltwater on the grounded ice largely ponds in less-densely spaced, larger depressions (Fig. 2.10b) that likely reflect bedrock topography (Echelmeyer and others, 1991; Sergienko, 2013). Here, catchment areas are also larger, like those observed in other grounded regions of the GrIS (e.g. Banwell and others, 2014; Poinar and others, 2015).

2.6 Conclusion

Focusing on three melt seasons, 2014, 2015 and 2016, we present the first quantitative study of surface lake characteristics on a floating ice tongue in Greenland. We take advantage of

the narrower bands and higher acquisition rate of Landsat 8 OLI compared to its predecessor, Landsat 7 ETM+, which allows us to constrain spatial and temporal variations in surface hydrology on Petermann Glacier to a daily temporal-resolution on occasions.

We show that surface lakes form across Petermann's floating ice tongue during each melt season. In each year, surface lakes develop in early-mid June as air temperatures begin to rise, and the total number of surface lakes and their total volumes peak in late June/early July. Despite sustained high temperatures through July and August in each year, the total meltwater storage in surface lakes falls during this time. We suggest that this may be due to both meltwater transportation across the tongue and into the ocean by a river, and due to lake drainage events on the tongue. However, we note that as the mean lake depth stays relatively constant during this time, a large proportion of the lakes that drain must be doing so rapidly, and completely, by hydrofracture. (NB. in this study we only actually observe two rapid lake drainage events.) Many other surface lakes drain more slowly (either completely or partially), and the remainder do not drain at all, but instead become covered by snow/ice. Lakes on the tongue have a mean area $\sim$20% of those on the grounded ice, and exhibit lower variability in maximum and mean depth, differences which are due to the contrasting formation processes of lakes in each environment.

Based on previous studies of surface lakes on Antarctic ice shelves, the presence of surface lakes on Petermann's floating tongue may be indicative of its vulnerability to instability and potential collapse (e.g. Scambos and others, 2000, 2003; Banwell and others, 2013). We find lakes to cover $<$2.8% of the total surface area of Petermann's tongue, compared to the 5.3% of Larsen B's area that was covered prior to its collapse in 2002 (Banwell and others, 2014). Predicted future rises in air temperature (Kirtman and others, 2013) could enable a higher density of lakes, with larger volumes, to develop from earlier in the season, possibly leading to increased ice tongue instability. However, the decline of surface lakes through July and August in each year studied, despite sustained high temperatures during those months, suggests that evacuation of meltwater from the tongue (e.g. by a river. c.f. Bell

and others, 2017) may limit the total volumes of meltwater storage on Petermann's floating tongue, thereby mitigating the risk of instability and break-up.

2.7 Appendix: Supplementary Methods

2.7.1 Lake boundary/area algorithm

The lake boundary/area algorithm (Box and Ski, 2007; Banwell and others, 2014) creates a mask of surface lake areas by classifying the image pixels as either 'water-covered' or not. OLI bands 2 (blue; 450-510 nm) and 4 (red; 640-670 nm) were first converted from digital numbers to reflectance values using the equations of Chander and others (2009). Then the blue/red ratio of reflectance was evaluated; this ratio is highest where water is darkest in colour, indicative of deep water, and decreases towards the shallower lake edge. Based on testing different blue/red ratios and visual comparison with the pan-sharpened true-color images, a single minimum-threshold ratio, corresponding to the lake edge, was selected to identify the lakes throughout the season. A threshold ratio of 1.5 was chosen for this study, which is the same as that chosen by Pope and others (2016), and is comparable to threshold values used by Banwell and others (2014; 1.05-1.25) and Arnold and others (2014; 2-3). Sensitivity tests indicated that application of a threshold ratio >1.5 excluded too many surface lakes that were otherwise visible by manual visual interpretation, and a threshold ratio <1.5 identified too many false-positives. An exception was made for the higher-elevation Site 4 (location shown in Fig. 2.1) in objective (iii) only, where it was found to be necessary to use a higher threshold value of 1.9 to avoid classifying large expanses of slush as surface lakes (Yang and Smith, 2013). The nature of the identification algorithm means that lakes with a complete snow- and/or ice-cover were not identified as surface lakes.

Following Pope and others (2016), water-covered features identified by the algorithm that were ≤ 4 pixels in area were removed. A threshold of 4 was deemed sufficiently high to exclude small features that likely comprised solely of mixed pixels (i.e. those with a value

representative of the average of different surface types, e.g. snow/ice/water) while being sufficiently low to maximize inclusion of small lakes. However, unlike the study by Pope and others (2016), which did not classify any water-covered features narrower than 2 pixels (i.e. 60 m) as surface lakes, we decided to classify these areas as surface lakes. This decision was based on manual visual interpretation of the study site in pan-sharpened (15 m spatial resolution) OLI imagery that indicated that many of these narrow features, particularly on the low surface-gradient tongue, are surface lakes, and not meltwater channels. This does mean, however, that some sections of channels may have been misidentified as surface lakes in our analysis.

Some shadows on the ice tongue, due to large- and small-scale nearby topography, were also found to cause false-positives in some instances. For example, a 2.6 km^2 area on the western flank of the tongue was persistently covered in shadow from the fjord walls and thus was excluded from analysis. Variations in the surface topography of the tongue, particularly towards the end of each melt season, cast small, localized, shadows that were falsely identified as surface lakes. These features were difficult to identify and quantify for exclusion and therefore contribute to noise and uncertainty in our analysis.

2.7.2 Lake-depth algorithm

Following Banwell and others (2014), with improvements suggested by Pope and others (2016), we employed the lake-depth algorithm originally based on the Beer-Lambert law (Ingle and Crouch, 1988) and developed by Sneed and Hamilton (2007), which describes the attenuation of radiation through a water column. The depth of a surface lake can be approximated as:

$$z = [\ln(A_{\mathrm{d}} - R_{\infty}) - \ln(R_{\mathrm{lake}} - R_{\infty})]/g$$

where z is lake depth in meters, A_{d} is the lake bottom albedo, R_{∞} is the reflectance of optically deep water, R_{lake} is the reflectance of a lake pixel, and g is a value related to

the losses in upward and downward travel through the water column and varies with the wavelength used. To determine A_{d}, the mean reflectance of a ring of pixels adjacent to the identified surface lake pixels was assumed to be representative of the pixels at the lake bottom. Some images did not contain optically deep water, and the difference in results between using an R_{∞} value of 0 and a value obtained from the ocean (as in Banwell and others, 2014) was found to be negligible. Therefore, an R_{∞} value of 0 was used and considered sufficiently accurate for the purposes of the study. g values were taken from Pope and others (2016).

The depth of each pixel in a surface lake was calculated using a measure of reflectance both in band 2 and band 8 (panchromatic; 520-900 nm), and the final depth result was taken as the mean of the two results, as recommended by Pope and others (2016) for OLI imagery.

The lake-depth algorithm makes several assumptions. It assumes that: i) the substrate of the lake is homogenous and that the impact on absorption of any dissolved matter in the water is negligible; ii) there is no scattering of light from the lake surface associated with roughness due to wind; and iii) that the albedo of the pixels at the edge of lake is representative of those at the lake bottom (Sneed and Hamilton, 2007; Banwell and others, 2014).

Table 2.1: Table of satellite image IDs and dates used in the analysis of intra- and inter-seasonal evolution of surface lakes, 2014-2016 (objective i)

Date	Image ID
27 June 2014	LC80312482014178LGN00
29 June 2014	LC80450012014180LGN00
4 July 2014	LC80642432014185LGN00
6 July 2014	LC80302482014187LGN00
15 July 2014	LC80450012014196LGN00
31 July 2014	LC80612432014212LGN00
7 August 2014	LC80302482014219LGN00
9 August 2014	LC80440012014221LGN00
11 August 2014	LC80420012014223LGN00
12 August 2014	LC80652432014224LGN00
16 August 2014	LC80450012014228LGN00
18 August 2014	LC80430012014230LGN00
25 August 2014	LC80440012014237LGN00
30 August 2014	LC80312482014242LGN00
31 August 2014	LC80380022014243LGN00
11 June 2015	LC80420012015162LGN00
13 June 2015	LC80400012015164LGN00
15 June 2015	LC80380022015166LGN00
16 June 2015	LC80450012015167LGN00
4 July 2015	LC80430012015185LGN00
8 July 2015	LC80390012015189LGN00
9 July 2015	LC80302482015190LGN00
11 July 2015	LC80440012015192LGN00
13 July 2015	LC80420012015194LGN00
15 July 2015	LC80400012015196LGN00
16 July 2015	LC80312482015197LGN00
17 July 2015	LC80380022015198LGN00
24 July 2015	LC80390022015205LGN01
31 July 2015	LC80400012015212LGN00
1 August 2015	LC80312482015213LGN00
2 August 2015	LC80380022015214LGN00
12 August 2015	LC80440012015224LGN00
14 August 2015	LC80420012015226LGN00
1 June 2016	LC80380022016153LGN00
2 June 2016	LC80450012016154LGN00
11 June 2016	LC80440012016163LGN00
12 June 2016	LC80672422016164LGN00
16 June 2016	LC80632432016168LGN00
17 June 2016	LC80380022016169LGN00
18 June 2016	LC80612432016170LGN00
25 June 2016	LC80622432016177LGN00
9 July 2016	LC80642432016191LGN00
10 July 2016	LC80390012016192LGN00
11 July 2016	LC80622432016193LGN00
13 July 2016	LC80440012016195LGN00
14 July 2016	LC80672422016196LGN00
15 July 2016	LC80420012016197LGN00
17 July 2016	LC80400012016199LGN00
18 July 2016	LC80632432016200LGN00
19 July 2016	LC80380022016201LGN00
24 July 2016	LC80410012016206LGN00
30 July 2016	LC80672422016212LGN00
31 July 2016	LC80420012016213LGN00
7 August 2016	LC80430012016220LGN00

Table 2.1 continued:

Date	Image ID
9 August 2016	LC80410012016222LGN00
25 August 2016	LC80410012016238LGN00
26 August 2016	LC80322482016239LGN00

Table 2.2: Table of satellite image IDs and dates used in the analysis of intra- and inter-seasonal evolution of Lake A (2014-2016) (objective ii)

Date	Image ID
17 June 2014	LC80410012014168LGN00
20 June 2014	LC80302482014171LGN00
24 June 2014	LC80420012014175LGN00
25 June 2014	LC80652432014176LGN00
26 June 2014	LC80400012014177LGN00
11 June 2015	LC80420012015162LGN00
13 June 2015	LC80400012015164LGN00
15 June 2015	LC80380022015166LGN00
16 June 2015	LC80450012015167LGN00
11 June 2016	LC80440012016163LGN00
12 June 2016	LC80672422016164LGN00
16 June 2016	LC80632432016168LGN00
17 June 2016	LC80380022016169LGN00
18 June 2016	LC80612432016170LGN00
25 June 2016	LC80622432016177LGN00

Table 2.3: Table of satellite image IDs and dates used in the analysis of intra- and inter-seasonal evolution of Lake B (2014-2016) (objective ii)

Date	Image ID
17 June 2014	LC80410012014168LGN00
20 June 2014	LC80302482014171LGN00
24 June 2014	LC80420012014175LGN00
25 June 2014	LC80652432014176LGN00
26 June 2014	LC80400012014177LGN00
27 June 2014	LC80632432014178LGN00
29 June 2014	LC80450012014180LGN00
30 June 2014	LC80360022014181LGN00
1 July 2014	LC80430012014182LGN00
4 July 2014	LC80642432014185LGN00
5 July 2014	LC80390012014186LGN00
6 July 2014	LC80302482014187LGN00
15 July 2014	LC80450012014196LGN00
11 June 2015	LC80420012015162LGN00
13 June 2015	LC80400012015164LGN00
15 June 2015	LC80380022015166LGN00
16 June 2015	LC80450012015167LGN00
4 July 2015	LC80430012015185LGN00
8 July 2015	LC80390012015189LGN00
9 July 2015	LC80302482015190LGN00
11 July 2015	LC80440012015192LGN00
13 July 2015	LC80420012015194LGN00
15 July 2015	LC80400012015196LGN00
16 July 2015	LC80312482015197LGN00
17 July 2015	LC80380022015198LGN00
24 July 2015	LC80390022015205LGN01
31 July 2015	LC80400012015212LGN00
1 August 2015	LC80312482015213LGN00
16 June 2016	LC80632432016168LGN00
17 June 2016	LC80380022016169LGN00
18 June 2016	LC80612432016170LGN00
25 June 2016	LC80622432016177LGN00
9 July 2016	LC80642432016191LGN00

CHAPTER 3

FORMATION OF PEDESTALLED, RELICT LAKES ON THE MCMURDO ICE SHELF, ANTARCTICA

3.1 Introduction

Since Mercer's (1978) paper heralding the threat of sea-level rise from a collapsing West Antarctic Ice Sheet, glaciologists have sought to characterize how Antarctica's ice shelves, which buttress the ice sheet, respond to rising air and ocean temperatures. Recent observations show that surface meltwater is pervasive around the ice sheet (Kingslake and others, 2017) and its presence is predicted to increase with future climate change (Trusel and others, 2015; Bell and others, 2018). In sufficient quantities, meltwater on ice shelves can promote ice-shelf instability, as evidenced by the behaviour of ∼3000 meltwater lakes on the surface of the Larsen B Ice Shelf prior to its collapse in 2002 (Glasser and Scambos, 2008; Banwell and others, 2014). This has led to the notion that meltwater-driven hydrofracture (Scambos and others, 2003; 2009) and flexure (Banwell and others, 2013) can be strong destabilizing factors for ice shelves. Studies of meltwater-induced flexure have focused on forcing by surface lake filling and drainage (Banwell and others, 2013; Banwell and MacAyeal, 2015) and movement of surface meltwater (Banwell and others, in press). Ice-shelf flexure may also be forced by ocean tides (Vaughan, 1995; Walker and others, 2013; Rack and others, 2017) and swell (Massom and others, 2018), and other processes such as basal crevassing (McGrath and others, 2012) and ice flow over grounding lines (Walker and others, 2013). Here we propose that large spatial contrasts in surface ablation rates, which lead to contrasting and evolving hydrostatic buoyancy forces, may also have an effect on ice-shelf flexure, and therefore ice-shelf stability.

Previous studies of ice-shelf surface hydrology and mass balance have focused on relatively 'clean' (debris-free) Antarctic and Greenlandic ice shelves, such as Larsen B (Banwell and others, 2014), Larsen C (Bevan and others, 2017), Langhovde Glacier (Langley and others,

2016), Roi Baudoin (Lenaerts and others, 2017), Nansen (Bell and others, 2017), Petermann Glacier (Macdonald and others, 2018) and others (Kingslake and others, 2017; Bell and others, 2018). In the present study, however, we report on the 20-year surface evolution of the debris-covered McMurdo Ice Shelf (McMIS). Part of this evolution involves the emergence of previously undocumented pedestalled, relict lakes that we refer to as 'pedestals' because of their topographic expression. These features develop over inter-annual timescales, beginning as surface lakes, then becoming shallow subsurface lakes, and finally developing into raised areas of high albedo/low ablation compared to their surroundings.

Pedestals are glacio-morphic features that have not been documented before. Here, we document the development of specific pedestals on the McMIS and present a conceptual model for their formation (there may be others in this area, but we focus on those for which we have field observations). We do this primarily by analysing satellite image data collected over the period 1999-2018. Additionally, we analyse field photographs, in-situ field observations, and field-based topographic surveys conducted primarily during the 2016/2017 austral summer, with supplementary observations from the 2015/2016 austral summer.

3.2 Study Site

The McMIS is a 1500 km^2 ice shelf in the northwest corner of the Ross Ice Shelf. Its ice front faces McMurdo Sound to the north and it abuts the southern tip of Ross Island, where the US McMurdo Station is situated, to its northeast (Fig. 3.1a). The ice shelf is relatively thin and in the study area (Fig. 3.1b) it is at its regional minimum, ∼10-30 m (Rack and others, 2013; Campbell and others, 2017). The ice flow is slow (∼28 $m^{a\text{-}1}$) and oblique to the ice front (Banwell and others, 2017). Surface accumulation occurs in the east of the McMIS (Paige, 1968) and subsurface accumulation occurs through basal freezing (Kellogg and others, 1990; Fitzsimons and others, 2012).

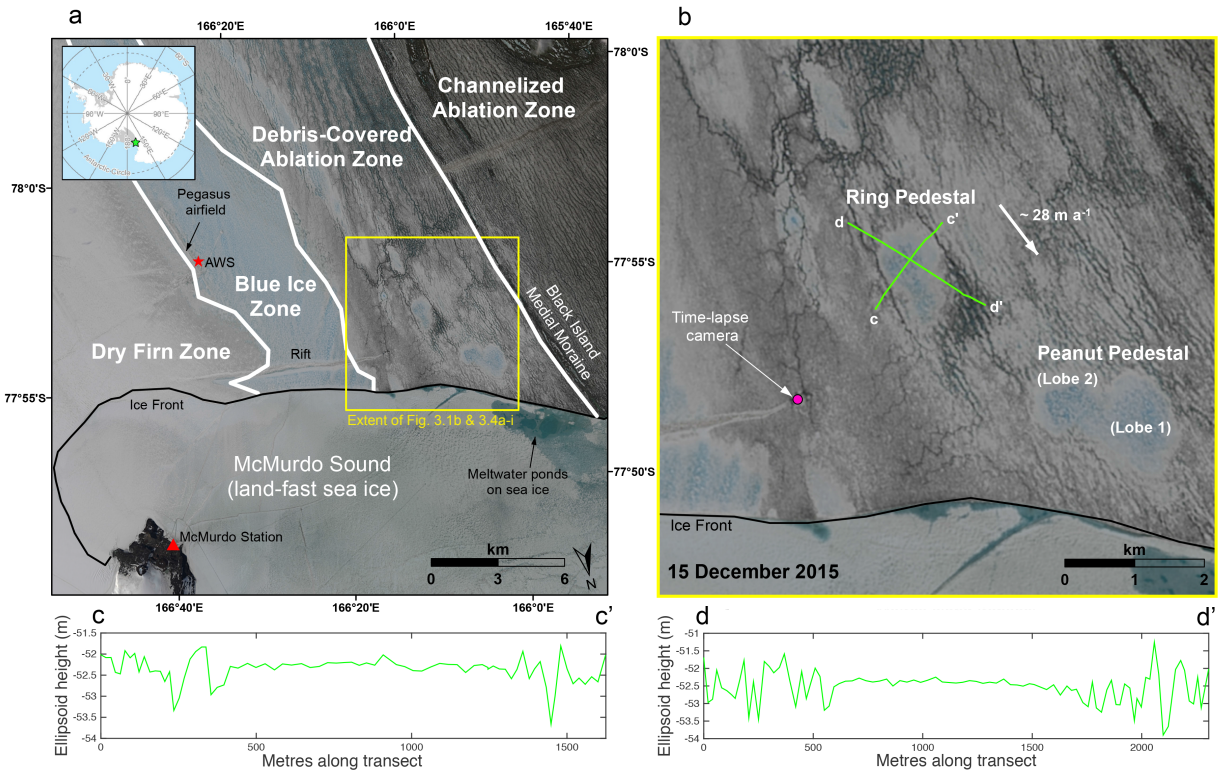

Fig. 3.1: (a) Part of the McMIS (green star in top-left inset shows location); (b) close up of the study region (yellow box in (a)); (c-d) surface topography of Ring Pedestal and its surrounding area (green lines in (b)). The background image is a pan-sharpened true-colour Landsat 8 OLI image dated 15 December 2015. White lines on (a) mark boundaries between different zones of the ice shelf (see text for explanation). The location is displayed for the automatic weather station (AWS) used for analysis (data displayed in Fig. 3.5). The white arrow in (b) indicates the local ice flow direction and speed (~335° True at ~28 m a^{-1} based on GPS velocity data from the 2016/17 austral summer; Banwell and others, 2017). The location is displayed for the time-lapse camera (data displayed in Fig. 3.2). Green lines on (b) indicate the location of the topographic surface profile transects shown in (c-d) that were measured by roving GPS ground survey. Ring and Peanut Pedestals can be seen in their advanced, pedestalled states. The inset map is from Matsuoka and others (2018).

3.3 Observations

Observations were made from the ground and helicopter during three field deployments; December 2015-January 2016, October-November 2016, and January-February 2017. Additionally, a time-lapse camera (location in Fig. 3.1b) captured images of the surface every 30 minutes between 25 November 2016 and 27 January 2017 (see Section 3.11.2 for further

details). In November 2016, two approximately perpendicular transects across Ring Pedestal and its immediate surroundings were surveyed using a roving differential Global Positioning System (GPS) (5-10 cm vertical uncertainty, see Section 3.11.5), with locations indicated in Fig. 3.1b.

A time-series of completely- or partially-cloud-free Landsat 7 and 8 images over the study site (Fig. 3.1b) was acquired for the period 13 December 1999 to 19 January 2018 (Table 3.1). Moderate Resolution Imaging Spectroradiometer (MODIS) images were also analysed in NASA's Worldview application for January-February 2002, when there was a gap in the Landsat 7 record. Analysis of the evolution of the study region was carried out by visual inspection of the images, with a particular focus on the evolution of Ring Pedestal, and the two lobes of Peanut Pedestal (Fig. 3.1b).

To assess the evolution of the study site in response to changes in temperatures, mean monthly air temperatures were calculated for our study period (when data were available). Data were obtained from the Pegasus North automatic weather station (AWS) (location in Fig. 3.1a, see Section 3.11.6).

To place observations made in the study region (Fig 3.1b) into a wider perspective, we first classified a larger area of the McMIS (Fig 3.1a) into distinct zones based on surface cover. This was done by assessing the output of a supervised classification of a Landsat 8 image (Fig. 3.S1), dated 12 December 2016 (see Section 3.11.1), in combination with qualitative visual inspection of the 1999-2018 imagery for the larger area, and consideration of reports in the literature.

3.4 Ice-Shelf 'Zones'

From East to West, across a distance of ∼12 km, the McMIS transitions from a 'Dry Firn Zone', through a 'Blue Ice Zone' and a hydrologically-dynamic 'Debris-Covered Ablation Zone', to, finally, a debris-covered 'Channelized Ablation Zone' (Fig. 3.1a). Our study site is situated in the 'Debris-Covered Ablation Zone'.

The Western portion of the McMIS includes the Debris-Covered Ablation and the Channelized Ablation Zones (Fig. 3.1a). The area is widely covered in gravel-size, or finer, debris that has a large influence on the surface energy balance (Fig. 3.1; Glasser and others, 2006, Clendon, 2009). Due to the low albedo of the debris, which across most of the area is too thin to thermally insulate the ice (c.f. Østrem, 1959), the debris-covered areas experience high rates of ablation (Glasser and others, 2006). The surface debris is dispersed and redistributed from the Black Island Medial Moraine (BIMM) that runs from south to north (Fig. 3.1a; Glasser and others, 2006; 2014). On and around the patches of surface debris, meltwater has been observed as early as November and as late as March (Debenham, 1965), with most melt occurring in December and January (Banwell and others, in press) when air temperatures reach or surpass 0°C.

Immediately east of the BIMM is the Debris-Covered Ablation Zone (Fig. 3.1a), an area of more heterogeneous debris cover (and hence albedo) than in the Channelized Ablation Zone to the west of the BIMM. The Debris-Covered Ablation Zone is the area where the biggest changes in surface hydrology appear to have taken place and new surface lakes (at least those >∼150 m in diameter) and pedestals have developed exclusively in this zone over the last ∼20 years as we report below. Currently, complex networks of anabranching channels exist in this zone, which pass through lakes or flow around pedestals. Melt ponds that form annually on the sea ice and abut this ice shelf zone suggest that at least some of the streams export meltwater over the ice shelf front. There is also evidence of subsurface melting (MacAyeal and others, 2018) and subsurface water flow in this zone during the melt season, as late as March (Banwell and others, 2017).

In contrast, the Channelized Ablation Zone (Fig. 3.1a) appears not to have undergone such marked changes in surface hydrology over the last ∼20 years. The channels are more linear, and appear more incised and in a fixed-ice position compared with those in the Debris-Covered Ablation Zone.

Similarly, the Blue Ice Zone (Fig. 3.1a) appears not to have undergone marked changes

over the last ∼20 years. There are no surface lakes or streams present but substantial subsurface water has been observed there in summer. For example, Paige (1968) observed subsurface meltwater pools <1 m deep here, as did we in the field in December 2015. Further evidence of subsurface water in this area comes from observations of ice pingos, i.e. mounds of ice that form from the pressure in subsurface water pools as they freeze (Cailleux, 1962; Paige, 1968; Klokov and Diemand, 1995).

3.5 Differential Ablation

The presence or absence of a thin surface debris cover is known to have a substantial effect on albedo, and therefore ablation rates (Østrem, 1959). Where there was debris, we recorded a mean ablation rate of 11 mm day^{-1} (Std. dev.: 3.4 mm day^{-1}) against three stakes between early (5-11 November 2016) and late (21 January-1 February 2017) summer, but a rate of just 1.5 mm day^{-1} (Std. dev.: 0.6 mm day^{-1}) against nine stakes over the same time period where the surface was clean. This differential ablation, between patches of debris-covered and clean ice, creates a rough, irregular surface that becomes more pronounced as the summer progresses (Fig 3.2). Columns, pinnacles and platforms of clean ice stand tall, raised above surrounding areas of debris-covered ice. Raised, clean areas have horizontal extents of just a few centimetres to several meters. Some of these elevated areas become unstable due to the differential ablation and/or undercutting by meltwater streams, causing them to collapse. New clean-surface, low-ablation patches can form over dirty areas when a thick ice lid forms over a pool of meltwater, and especially if this is supplemented by thick snow drifting in the low elevation areas during winter. Conversely, in some locations, ablation in a clean area can expose a subsurface debris layer. Differential ablation is therefore highly spatially and temporally variable, producing a constantly changing surface topography and roughness in the Debris-Covered Ablation Zone.

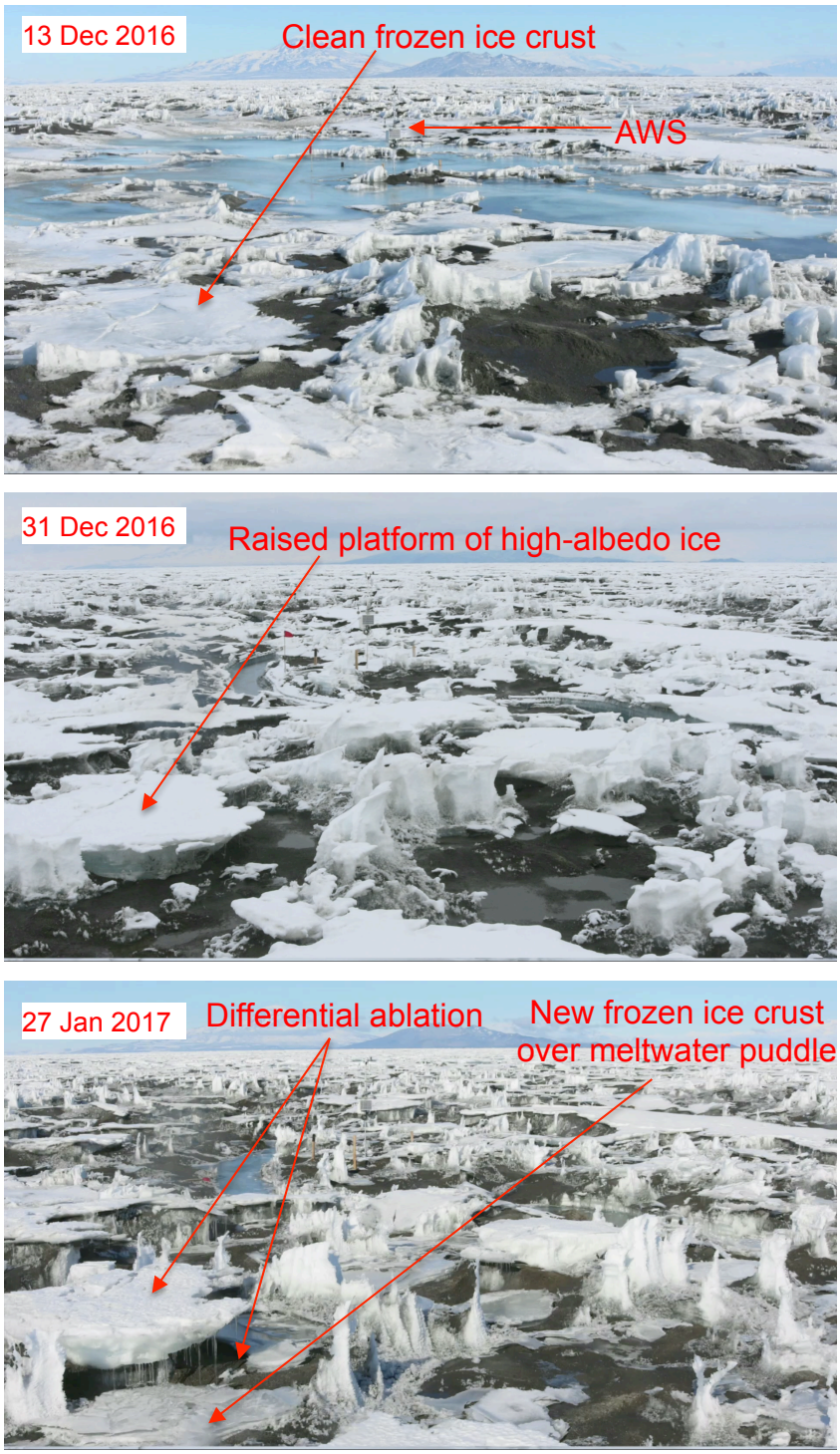

Fig. 3.2: Time-lapse camera photographs showing the effects of differential ablation at a small scale. The location of the time-lapse camera is shown in Fig. 3.1a. An automatic weather station (AWS) is visible in the upper, central area of each photograph.

Fig. 3.3: A pingo on Ring Pedestal in November 2016.

3.6 Pedestalled Relict Lakes

Ring Pedestal and Peanut Pedestal are conspicuous because of their large horizontal scales and debris-free surfaces (Fig. 3.1). Ring and Peanut's two lobes have diameters of ∼1 km. Unlike the surrounding area, the pedestals have a highly uniform, high-albedo, smooth, flat surface, suggestive of spatially uniform and low ablation rates.

Meltwater channels are diverted around the pedestals (Fig. 3.1b), showing they are raised compared to their surrounding areas. Their pedestalled nature is also illustrated by the topographic surveys conducted across Ring Pedestal and its surroundings (Fig. 3.1c-d). The surveys show the surrounding area has a highly variable topography with an elevation range of ∼2 m. This region includes many low areas with relatively high debris cover, some of which have coalesced to form stream channels. The pedestal surface, however, is >1 m higher than the surrounding low points and its elevation varies by <0.20 m over a distance of 900 m, except where there are ice pingos (Figs 3.1c-d and 3.3).

The pingos are typically ∼5 m in width and ∼1-2 m in height, with fractures radiating

from their peak (Fig 3.3). That pingos exist on the pedestals indicates that subsurface water has been present below the features (Cailleux, 1962). We observed subsurface water ∼1 m below the frozen surface of at least parts of Peanut Pedestal in January 2016 when we augured into its surface. Pingos are only observed on the pedestals and not elsewhere in the Debris-Covered Ablation Zone, but as mentioned above, they are recorded in the Blue Ice Zone (Paige, 1968), which is also characterized by the presence of subsurface water. The pedestals also share the light-blue appearance of the Blue Ice Zone, based on ground observations and satellite imagery (Fig. 3.1; Fig. 3.S1). Thus, the pedestals can be thought of as isolated, pedestalled Blue Ice Zones within the Debris-Covered Ablation Zone.

3.7 Formation of Pedestalled Relict Lakes

In our ∼20-year satellite record, we observe open water surface lakes develop, freeze over and evolve into pedestalled, relict lakes (Fig. 3.4). At the beginning of the time series, from December 1999 to December 2001 (Fig. 3.4a), there is no evidence of open water, frozen-over, or relict lakes in the study region. The first evidence of a lake forming is in a January 2002 MODIS image, when an open water lake becomes visible at Peanut Lobe 1 (Fig. 3.4b). At the beginning of the following summer (2002/2003), this lake has a thin frozen ice lid, which appears to have melted by 19 November 2002 (Video S1 in Macdonald and others, 2019), before the lake freezes over again by 17 December 2002 (Fig. 3.4c). Peanut Lobe 1 remains frozen over in 2003/2004 (Video S1 in Macdonald and others 2019).

In July 2004, the mean temperature is -40.5°C, the lowest for the study period (Fig. 3.5). In the summer of 2004/2005, despite ponding around it, Peanut Lobe 1 appears as an area of high-albedo ice and meltwater does not pond at or flow through it, during this (Fig. 3.4d) or subsequent melt seasons. This suggests that Peanut Lobe 1 starts to become a frozen-over, raised pedestal in 2004, possibly as a result of enhanced freezing-through of the lake because of the low winter temperatures. During the summer of 2004/2005, there is also an open water lake at the Ring site for the first time and Peanut Lobe 2 is an open

water lake immediately adjacent to Peanut Lobe 1 (Fig. 3.4d). Later in the summer, a superimposed ice lid forms over these two previously open-water surface lakes (Video S1 in Macdonald and others, 2019).

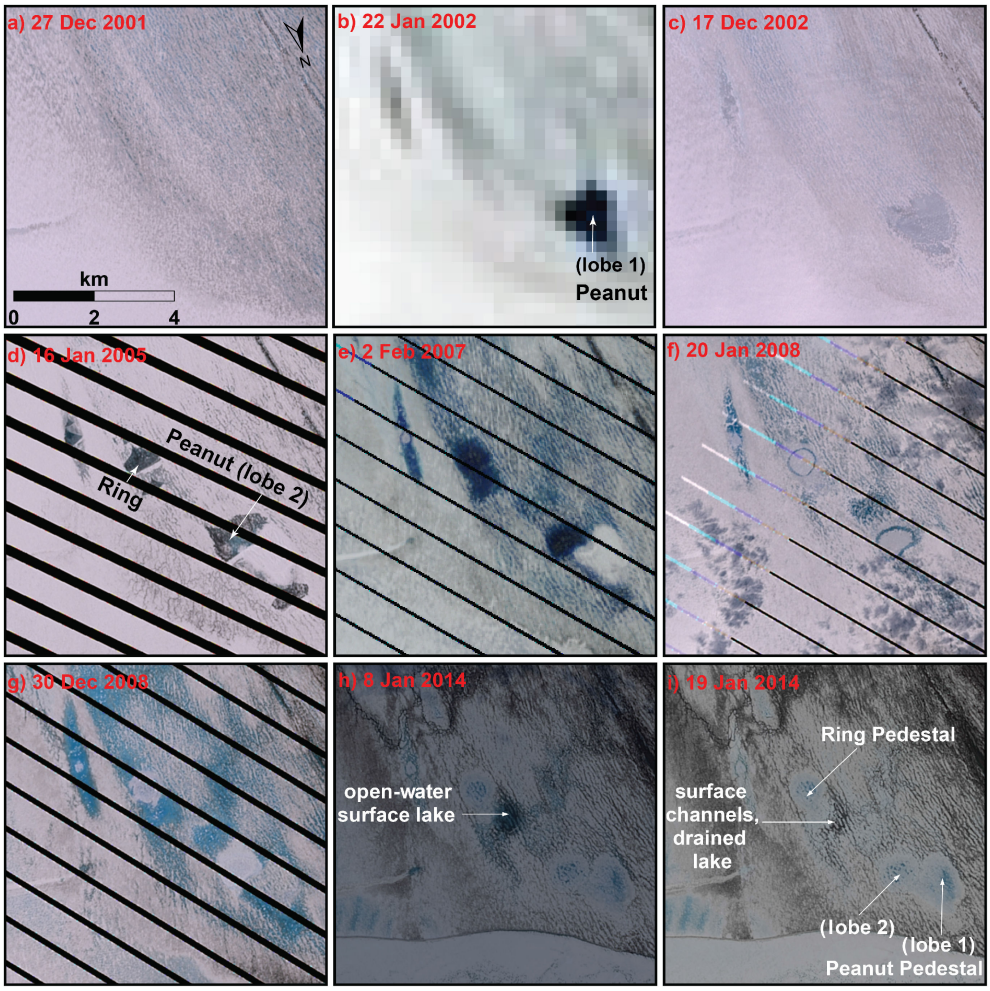

Fig. 3.4: Formation of Ring and Peanut Pedestals, from open-water surface lakes, to frozen-over surface lakes, to raised pedestals, from December 2001 to January 2014. No lakes are visible in (a). Peanut Lobe 1 is visible as (b) an open-water surface lake, (c) frozen-over surface lake and (d-i) pedestal. Ring and Peanut Lobe 2 are visible as (d-e) open-water surface lakes, (f) frozen-over surface lakes and (g-i) pedestals. Images (a, c-g) are true-colour pan-sharpened Landsat 7, (b) is a MODIS true-colour corrected reflectance image, and (h-i) are true-colour pan-sharpened Landsat 8 images. The extent of each image is shown in Fig. 3.1a. The complete time-series of all images acquired from 13 December 1999 to 19 January 2018 can be seen in Video S1 in Macdonald and others (2019).

In 2005/2006 there is a gap in the Landsat imagery and the MODIS images are difficult to interpret. However, open water lakes form again at the sites of Peanut Lobe 2 and Ring in

the 2006/2007 melt season and pedestalled Peanut Lobe 1 stands out as an area of very high albedo (Fig. 3.4e). These open water lakes freeze over at the end of that summer (Video S1 in Macdonald and others, 2019).

In the 2007/2008 melt season, Peanut Lobe 1 remains completely frozen over. At Peanut Lobe 2 and Ring there are frozen-over surface lakes with a ring of meltwater visible at the edge of each (Fig. 3.4f), similar to the rings of water that develop around ice-capped lakes on the Greenland Ice Sheet (e.g. Miles and others, 2017). The ring could be the result of melting at the edges of the ice cover, revealing water in the lakes (as in Greenland) or, alternatively, the frozen-over lakes may now have become pedestalled, with meltwater ponding in a ring-like depression that forms around them.

The second coldest month during the study period is August 2008 with a mean temperature of -39.6°C (Fig. 3.5). In the summer of 2008/2009, despite extensive meltwater ponding across the study region, including immediately adjacent to the Ring and Peanut sites, there appears to be no surface water at Ring or Peanut (both lobes), which have a high-albedo and appear to be frozen over (Fig. 3.4g). The fact that no water flows onto their apparently frozen surfaces suggests the features are now hydrologically isolated from their surroundings, which is consistent with them now being pedestalled. It is possible that the low temperatures during the preceding winter caused increased freeze-through, preventing melting of the ice surface in the summer and influencing the formation of the pedestals. After this melt season, all three sites retain high albedo, debris-free surfaces and show no evidence of surface water in subsequent satellite images. Furthermore, over the subsequent years (Fig. 3.4h-i), the pedestalled surfaces increasingly come to resemble the appearance of the Blue Ice Zone to the east (Fig. 3.1a), where blue ice dominates and both surface meltwater and debris are absent. From 2012/2013 onwards, a network of anabranching streams is clearly visible in the study area surrounding the pedestals, with all streams diverting around the pedestals (Fig. 3.4h-i).

We also note that not all surface lakes develop into pedestals. For example, an open-

water surface lake forms in the area immediately adjacent to Ring Pedestal on numerous occasions from 2008 onwards (e.g. Fig. 3.4h). On 8 January 2014, an open water surface lake is present there (Fig. 3.4h), but by 19 January 2014 it has drained (Fig. 3.4i), likely via the dense network of surrounding streams. This suggests that this area does not develop into a high albedo pedestal because the lake is able to drain before freezing over.

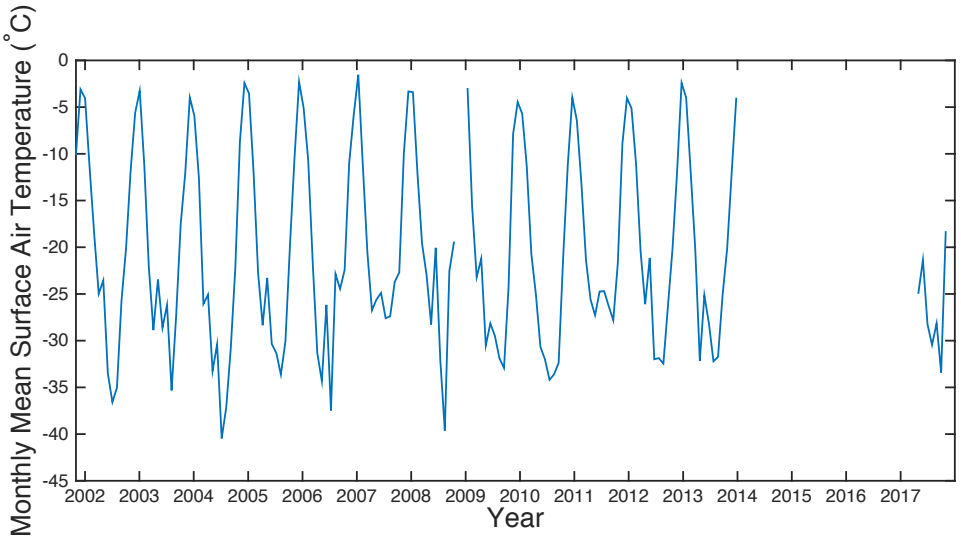

Fig. 3.5: Mean monthly air temperature at Pegasus North station in the east of the McMIS from November 2001 to November 2017, where data are available.

3.8 Conceptual Model

The observations described above lead us to propose the following conceptual model of pedestal formation on ice shelves (Fig. 3.6). The evidence suggests that a heterogeneous surface debris cover plays a key role in pedestal formation, due to the effects of debris on surface albedo and therefore energy balance.

Stage 1: In a high melt year, meltwater collects in a depression to form a shallow lake. This water, together with the high debris content, promotes lake-bottom ablation (Lüthje and others, 2006; Tedesco and others, 2012; Miles and others, 2018) and enlargement of the lake. The weight of the water causes a flexural response of the ice shelf, depressing it beneath and near to the lake (MacAyeal and Sergienko, 2013; Banwell and MacAyeal 2015).

Stage 2: The lake freezes over at the end of the melt season and remains frozen during the winter. Debris on the lake bottom is sufficiently far below the frozen surface that it is masked and the lake surface now has a higher albedo than the surrounding, debris-covered areas.

Stages 1 and 2 may occur over just one melt season, or they may repeat over multiple seasons, which will further enlarge the lake and cause additional ice-shelf flexure.

Stage 3: If, in a subsequent summer, the lake surface does not receive sufficient energy to melt its ice cover (which will now be thicker after low temperatures in the preceding winter), it retains this frozen, high-albedo surface. During this time, the frozen lake surface melts more slowly than the surrounding lower albedo, debris-covered areas. This differential ablation initiates the process of the former lake becoming pedestalled and hydrologically isolated. Meanwhile, the surrounding area of dirty ice shelf experiencing high ablation rates rebounds upwards, through ice flexure, to regain hydrostatic equilibrium, producing a ring-like depression around the pedestal in which meltwater ponds.

Beyond: If, during subsequent summers, the lake surface remains frozen, the differential ablation causes the former lake to become increasingly pedestalled. Meanwhile, the ring-like water-filled depression around this pedestal increases in depth as the rapidly ablating area continues to rebound hydrostatically. However, this surrounding area does not become as high as the pedestalled, relict lake because it has a lower ice thickness due to the higher ablation rates. Meltwater streams are diverted around, and ponds form next to, the pedestalled, relict lake. If, during a subsequent summer, energy receipt is particularly high, the pedestalled relict lake's frozen surface may melt, re-exposing the lake-bottom debris and enabling lake-bottom ablation to re-commence. This will slow the process of pedestal formation but not reverse it. Additional stages may exist but they have not yet been observed.

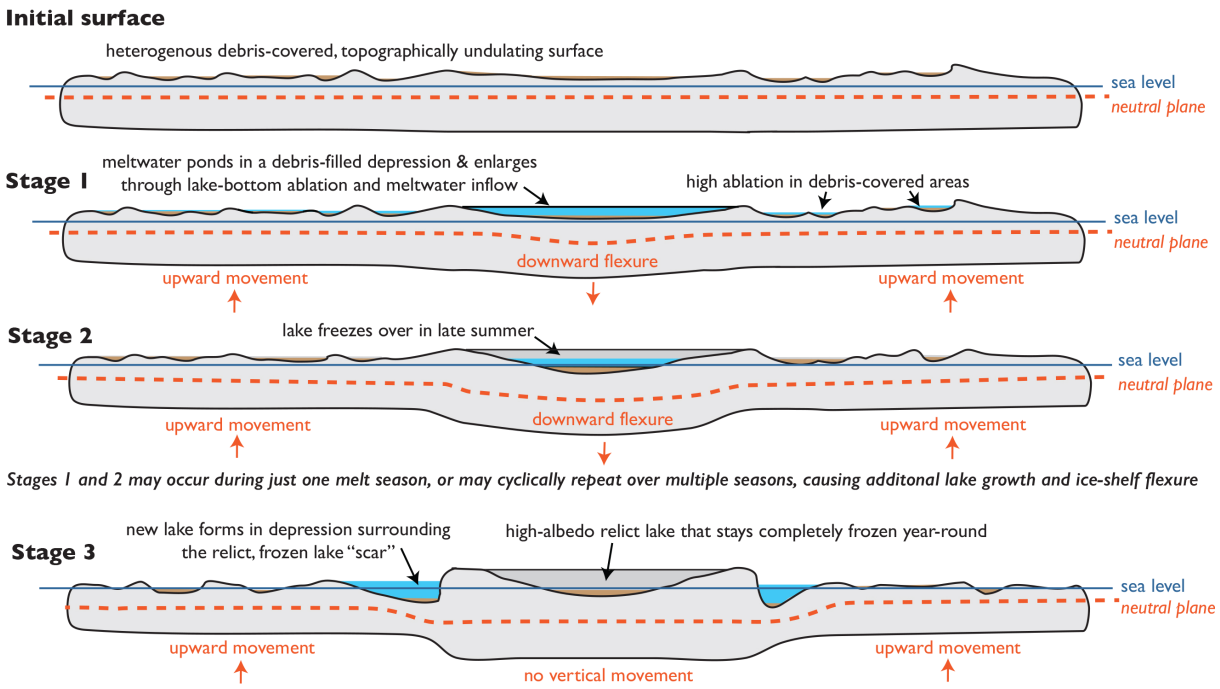

Fig. 3.6: Schematic illustration of the conceptual model of pedestal formation from debris-covered ice surface (initial surface), to open-water surface lake (stage 1), to frozen-over surface lake (stage 2) to pedestal (stage 3).

3.9 Implications

We suggest that the development of pedestalled relict lakes has a significant influence on the surface energy-balance, hydrology and flexure of an ice shelf. First, because pedestal formation reduces the amount of exposed surface debris, it increases the surface albedo and reduces the absorption of solar radiation. Expansion in the number of pedestals across the McMIS could, therefore, progressively lower average ablation rates and reduce surface meltwater runoff rates. This expansion may include the development of more directly-adjacent pedestals, like the two lobes of Peanut. The Debris-Covered Ablation Zone could increasingly resemble the Blue Ice Zone, an area with which the pedestals share certain characteristics. As such, there would also be an expansion of subsurface water in the area. However, the observed expansion of pedestalled areas may be limited if surface lakes drain, over the surface (as observed, Fig. 3.4i and Banwell and others, 2019) or through fractures (not observed to

date), before they freeze over in the winter, and by the eventual re-emergence of debris on the former lake bottom through ablation of the pedestal.

Second, because the pedestals are raised, and surrounded by a depression formed by hydrostatic rebound of the surrounding rapidly-ablating area, dense networks of diverted stream channels and intermittent areas of ponding meltwater form. Most notable is the area adjacent to and north-west of Ring Pedestal (Fig. 3.4h). If debris then becomes concentrated in these relatively low elevation areas, and if flowing meltwater passing through these areas helps prevent them from freezing over, then these areas between pedestalled features may become sites of sustained surface ablation.

Third, concentrated areas of meltwater ponding around pedestals, combined with hydrostatic rebound of the rapidly ablating areas (Fig. 3.6), could cause potentially significant ice-shelf flexure (e.g. Banwell and MacAyeal, 2015; Banwell and others, 2019), which may lead to fracture. The potential for ice-shelf fracture initiation will increase after multiple years of pedestal formation and associated ice flexure and stress build-up, which could contribute to ice-shelf instability (Banwell and others, 2013). Preliminary analysis (using the model of MacAyeal and others, 2015) indicates that the effect of pedestal formation on ice-shelf flexure appears to be strongest for ice shelves that are both thin (<50 m) and have debris-induced differential ablation rates leading to ∼10% thickness differences (2-5 m in the case of the 20-50 m thickness of the McMIS). The McMIS is atypical of ice shelves in Antarctica due to its low thickness and debris cover; so it remains to be determined whether pedestal formation will be a concern for flexure-stress driven ice-shelf fracture on other ice shelves. Modelling the flexural effect of pedestal formation will be the subject of further study in order to determine the potential influence on ice-shelf fracture and stability in more detail.

3.10 Conclusion

This study documents the development of novel ice-shelf glacio-morphic features that we call 'pedestalled relict lakes', or 'pedestals' for short. Although these features require the relatively unusual conditions found on the McMIS (an ice shelf with surface debris and meltwater), other ice shelves may become subject to debris-exposure or aeolian dust transport and enhanced surface melting as the climate changes. Where they develop, pedestals have a strong influence on the surface energy-balance, hydrology and potentially ice flexure, and thus could also affect the stability of an ice shelf.

3.11 Appendix: Supplementary Methods

3.11.1 Classification of 'surface type zones' on McMIS

Based on field observations and analysis of Landsat 7 and 8 imagery, we identified four main surface types on the McMIS: snow/dry firn, thick debris (i.e. the Black Island Medial Moraine), blue ice, and dirty (debris-covered) ice. We used a true-colour pan-sharpened Landsat 8 image from 12 December 2016, which was cloud-free across our area of interest, to perform a supervised classification of surface types. First, we identified pixels of each of the four surface types and assigned them as 'training data'. To maximise the available training data, we sourced training data from areas outside of the area shown in Fig. 3.1a, in addition to inside it. For example, training data for 'thick debris' included areas on land. Training pixels constituted 2% of total McMIS pixels in the image. Using ArcMap, we then used the training data with a 'minimum distance' supervised classification algorithm to classify every pixel in a multispectral version of the image (bands 1-7) into one of the four surface types. The output of this produced a 'surface-cover classification map' of the McMIS (Fig. 3.S1). The minimum distance algorithm assesses which class of surface type (as defined by the training data) each image pixel is spectrally closest to, based on the spectral signature of all seven bands. The number of training pixels was limited for the blue ice and dirty ice classes

because the heterogeneous surface made it difficult to identify large areas consisting solely of that surface type. This is why we used the 'minimum distance' algorithm, as opposed to the 'maximum likelihood' algorithm, because it can perform better when the number of training sites per a class is limited (Richards and Jia, 1999).

Using the surface-cover classification map (Fig. 3.S1) produced by the supervised classification, alongside visual interpretation of the images and reference to the literature, we divided the ice shelf into the Dry Firn Zone, Blue Ice Zone, Debris-Covered Ablation Zone and Channelized Ablation Zone shown in Fig 3.1a.

3.11.2 Field observations and time-lapse camera

We spent several weeks on the ground in the study area during three deployments: December 2015-January 2016; October-November 2016; and, January-February 2017. We actively explored and photographed the surface, and also made passive observations while undertaking other field activities. Additionally, we observed and photographed the surface of the ice shelf from a helicopter on numerous occasions in both summers.

The time-lapse camera that took the photos in Fig. 3.2 was a Harbotronics 'Cyclapse' system containing a Canon EOS Rebel T6i camera, which operated from 25 November 2016 until 27 January 2017, taking photos every 30 minutes. The location of the camera is shown in Fig. 3.1b and it was situated to collect data on Rift Tip Lake, a lake not reported here but reported in Banwell and others (2019).

3.11.3 Satellite imagery analysis

All November-February Landsat 7 Enhanced Thematic Mapper Plus (ETM+) and Landsat 8 Operational Land Imager (OLI) images of the study region that were sufficiently cloud-free over the study region shown in Fig. 3.1b were downloaded, covering the period 13 December 1999 to 19 January 2018. Images with heavy cloud cover could be used for analysis provided that at least one of our features of interest was visible. Landsat was chosen for its high

spatial resolution (30 m) compared with the lower spatial resolution of MODIS (250 m).

This period spans the first ETM+ images of the area until the most recent usable OLI image. Between 13 December 1999 and 31 January 2013 the images are captured by ETM+, and between 7 November 2013 and 18 January 2018 they are from OLI. OLI imagery has the advantage of a higher temporal acquisition rate than ETM+ and is free from the issue of missing scanlines that affects ETM+ imagery after May 2003 (as seen in Figs 3.4d - g). However, given the manual nature of the analysis used in this study, scanlines did not preclude imagery from being useful even when they obscured part of the study site. Additionally, for January-February 2002, which was a particularly important period for analysis, there were no Landsat images, so true-colour corrected surface reflectance MODIS images were analyzed in NASA's Worldview application (e.g. Fig. 3.4b). These images proved sufficient to at least identify the presence of the surface lake at Peanut Lobe 1 (Fig. 3.4b). MODIS images were also consulted for the 2005/2006 austral summer (when there were no Landsat images), but these images were difficult to interpret and not useful for analysis.

All true-colour pan-sharpened Landsat images were cropped to the region of interest (Fig. 3.1b) and assembled into a time-series for analysis (all images are visible in Video S1 in Macdonald and others, 2019). True-colour MODIS images for 2001/02 were similarly cropped and analysed separately. Analysis of the evolution of the pedestal sites and their interaction with the surrounding surface was carried out by manual visual interpretation of the images, with a particular focus on the sites of Ring and Peanut's two lobes. The unique nature of the pedestalled features, and their development from open water surface lakes, did not allow for an automated approach. Given our knowledge of the surface from the ground, manual visual interpretation of the satellite imagery is considered optimal for the purposes of the study.

3.11.4 Topographical survey

The surface profile of Ring Pedestal and its immediate surroundings was measured across two approximately perpendicular transects (locations indicated in Fig. 3.1b) using a roving Trimble R7 differential GPS provided by UNAVCO. There is 5-10 cm vertical uncertainty in the measurements. One member of the team marked out the route in an approximate straight line. The second member of the team walked, carrying the GPS system and counted their paces. On the surface of the pedestal they logged a measurement approximately every 40 paces (∼25-30 m). To better capture the high level of roughness in the area surrounding the pedestal, measurements were logged there approximately every 25 paces (∼15-20m). The frequency of measurements logged was limited by time constraints.

We acknowledge that other methods (e.g. terrestrial LIDAR) could characterize the surface topography of the pedestals at a higher spatial resolution and in three dimensions across the site. However, these data were not available to us. We regard these topographical transects sufficient for illustrating the contrast in topography of the pedestal and the surrounding area for the purpose of this study.

3.11.5 Ablation measurements

Mean ablation rates for debris-covered ice and clean ice were calculated from ablation measurements recorded at twelve sites across the study region. The heights of aluminium poles exposed above the snow/firn/ice surface was recorded when they were deployed (5-11 November 2016) and again when they were retrieved (21 January-1 February 2017). Nine poles were located in clean areas, where the ice surface was free of debris, and three where it was debris-covered. All poles were located within the study site (Fig. 3.1b). Three were located in the vicinity of the time-lapse camera, three on and around Ring Pedestal, three on and around Peanut Lobe 2, and three in a location ∼1 km east of Peanut Lobe 2.

3.11.6 Air temperature data

Daily surface air temperature data were acquired from the Antarctic Meteorological Research Center and Antarctic Weather Stations Project's website (http://amrc.ssec.wisc.edu/aws/api/form.html). All data from the Pegasus North AWS station that were available for our period of interest (November 1999 to January 2018) were downloaded. Data existed for all months between November 2001 and December 2013, except for November-December 2008. There were also data for December 2016-October 2017, except for January and March 2017. The mean temperature was calculated for each month and presented in Fig. 3.5.

3.11.7 Supplementary figures

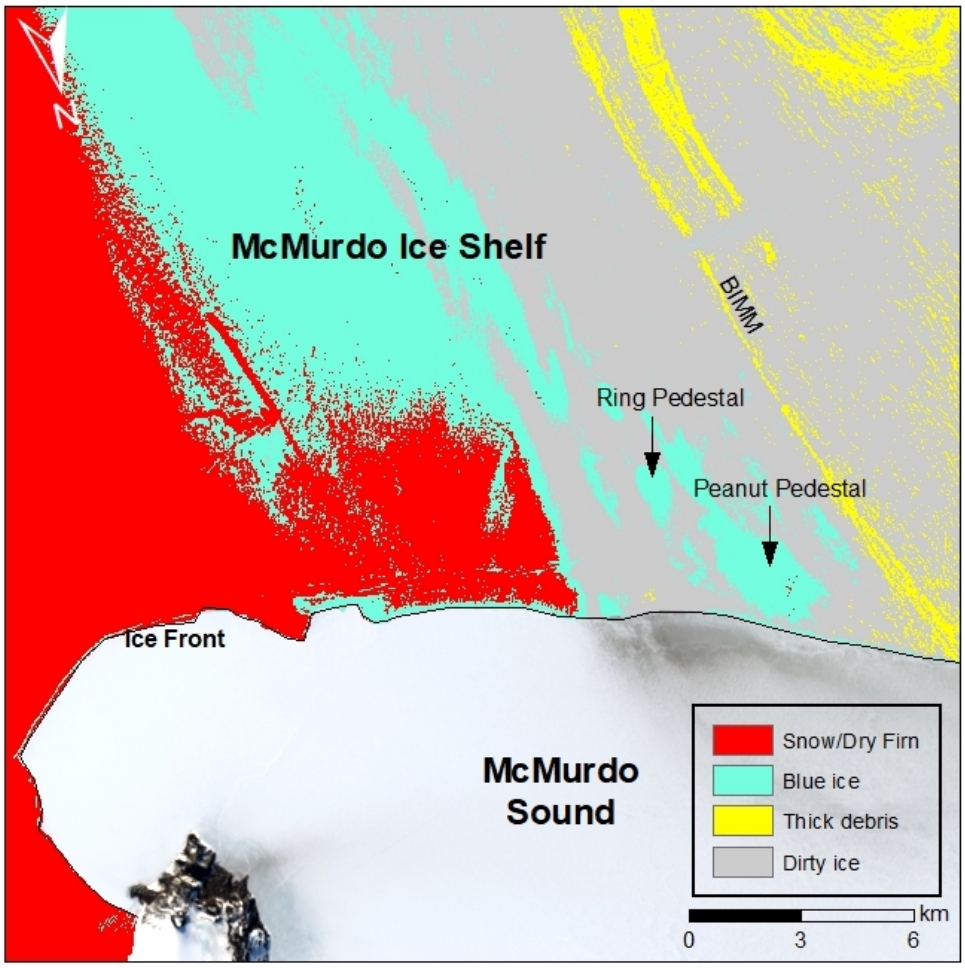

Fig. 3.S1: Surface-cover map of the McMIS based on a supervised classification analysis. The four surface types ('Snow/Dry Firn', 'Blue ice', 'Thick debris' and 'Dirty ice') are shown in the key, and were used to define the surface zones labelled in Fig. 3.1a. The classified image, which is also the background image, is a multispectral OLI image captured on 12 December 2016. The extent of the figure is the same as in Fig 3.1a. Note that the pedestals are classified as having a 'blue ice' surface, similar to that which dominates the Blue Ice Zone.

Table 3.1: Table of satellite image IDs and dates used to compile the time-series of the formation of pedestals. All images are Landsat 7 ETM+ (L7), Landsat 8 OLI (L8) or MODIS Terra (MT). For each image, we use our best judgement to determine whether Ring, Peanut Lobe 1, and Peanut Lobe 2 are 'open water' surface lakes (OW), 'frozen over' lakes (FO) or 'pedestalled'(P). '/' indicates that the feature does not yet exist in any form (i.e. there is bare ice/firn). '*' indicates that there is a ring of meltwater at the edge of the feature, as in Fig. 3.4f. As we discuss in the text, it is not clear at this point whether the lake is 'frozen over' or 'pedestalled'.

Date	Image ID	Sensor	Ring	Peanut Lobe 1	Peanut Lobe 2
13 Dec 1999	LE70531161999347EDC00	L7	/	/	/
18 Dec 1999	LE70561151999352EDC00	L7	/	/	/
12 Jan 2000	LE70551162000012EDC00	L7	/	/	/
14 Jan 2000	LE70531162000014EDC00	L7	/	/	/
11 Dec 2000	LE72261282000346EDC00	L7	/	/	/
21 Nov 2001	LE70561152001325EDC01	L7	/	/	/
25 Nov 2001	LE70521162001329EDC00	L7	/	/	/
2 Dec 2001	LE70531162001336EDC00	L7	/	/	/
7 Dec 2001	LE70561152001341EDC00	L7	/	/	/
27 Dec 2001	LE70521162001361EDC00	L7	/	/	/
28 Dec 2001	https://go.nasa.gov/2O2BuvW	MT	/	/	/
29 Dec 2001	https://go.nasa.gov/2O6iE7e	MT	/	/	/
31 Dec 2001	https://go.nasa.gov/2oY7IgR	MT	/	OW	/
1 Jan 2002	https://go.nasa.gov/2O3F4WB	MT	/	OW	/
4 Jan 2002	https://go.nasa.gov/2oTnSIu	MT	/	OW	/
6 Jan 2002	https://go.nasa.gov/2O5AOGb	MT	/	OW	/
9 Jan 2002	https://go.nasa.gov/2O4HDYH	MT	/	OW	/
10 Jan 2002	https://go.nasa.gov/2oVxrqk	MT	/	OW	/
11 Jan 2002	https://go.nasa.gov/2O0ZIqh	MT	/	OW	/
13 Jan 2002	https://go.nasa.gov/2O7T3dZ	MT	/	OW	/
14 Jan 2002	https://go.nasa.gov/2oWep35	MT	/	OW	/
17 Jan 2002	https://go.nasa.gov/2oWemEr	MT	/	OW	/
19 Jan 2002	https://go.nasa.gov/2O0yy2W	MT	/	OW	/
22 Jan 2002	https://go.nasa.gov/2oIiMib	MT	/	OW	/
26 Jan 2002	https://go.nasa.gov/2O0xcFo	MT	/	OW	/
10 Feb 2002	https://go.nasa.gov/2oWVPYN	MT	/	FO	/
14 Feb 2002	https://go.nasa.gov/2O5Q1qR	MT	/	FO	/
15 Feb 2002	https://go.nasa.gov/2oXrCJ4	MT	/	FO	/
25 Feb 2002	https://go.nasa.gov/2oWKhF2	MT	/	FO	/
28 Feb 2002	https://go.nasa.gov/2oWL6h6	MT	/	FO	/
19 Nov 2002	LE70531162002323EDC01	L7	/	FO	/
26 Nov 2002	LE70541162002330EDC00	L7	/	OW	/
5 Dec 2002	LE70531162002339EDC00	L7	/	OW	/
17 Dec 2002	LE70571152002351EDC00	L7	/	FO	/
7 Jan 2004	LE70551162004007EDC01	L7	/	FO	/
23 Jan 2004	LE70551162004023EDC01	L7	/	FO	/
30 Jan 2004	LE70561152004030EDC01	L7	/	FO	/
3 Feb 2004	LE70521162004034EDC01	L7	/	FO	/
17 Feb 2004	LE70541162004048EDC01	L7	/	FO	/
26 Feb 2004	LE70531162004057EDC02	L7	/	FO	/
16 Jan 2005	LE70561152005016EDC00	L7	OW	P	OW
20 Jan 2005	LE70521162005020EDC00	L7	OW	P	OW
1 Feb 2005	LE70561152005032PFS00	L7	FO	P	FO
3 Feb 2005	LE70541162005034PFS00	L7	FO	P	FO
28 Feb 2005	LE70531162005059EDC00	L7	FO	P	FO

Table 3.1 continued:

Date	Image ID	Sensor	Ring	Peanut Lobe 1	Peanut Lobe 2
26 Nov 2006	LE70571152006330EDC00	L7	FO	P	FO
28 Nov 2006	LE70551162006332EDC00	L7	FO	P	FO
5 Dec 2006	LE70561152006339EDC00	L7	FO	P	FO
7 Dec 2006	LE70541162006341EDC00	L7	FO	P	FO
16 Dec 2006	LE70531162006350EDC00	L7	FO	P	FO
21 Dec 2006	LE70561152006355EDC00	L7	FO	P	FO
23 Dec 2006	LE70541162006357EDC00	L7	FO	P	FO
28 Dec 2006	LE70571152006362EDC00	L7	FO	P	FO
30 Dec 2006	LE70551162006364EDC00	L7	FO	P	FO
13 Jan 2007	LE70571152007013EDC00	L7	FO	P	FO
17 Jan 2007	LE70531162007017EDC00	L7	FO	P	FO
2 Feb 2007	LE70531162007033EDC00	L7	OW	P	OW
1 Dec 2007	LE70551162007335EDC00	L7	FO	P	FO
3 Dec 2007	LE70531162007337EDC00	L7	FO	P	FO
12 Dec 2007	LE70521162007346EDC00	L7	FO	P	FO
15 Dec 2007	LE70571152007349EDC00	L7	FO	P	FO
19 Dec 2007	LE70531162007353EDC00	L7	FO	P	FO
2 Jan 2008	LE70551162008002EDC00	L7	FO	P	FO
13 Jan 2008	LE70521162008013EDC00	L7	FO	P	FO
20 Jan 2008	LE70531162008020EDC00	L7	FO*	P	FO*
25 Jan 2008	LE70561152008025EDC00	L7	FO*	P	FO*
5 Feb 2008	LE70531162008036EDC00	L7	FO*	P	FO*
26 Feb 2008	LE70561152008057EDC00	L7	FO	P	FO
8 Nov 2008	LE70561152008313EDC00	L7	FO	P	FO
10 Nov 2008	LE70541162008315EDC00	L7	FO	P	FO
12 Nov 2008	LE70521162008317EDC00	L7	FO	P	FO
17 Nov 2008	LE70551162008322EDC00	L7	FO	P	FO
10 Dec 2008	LE70561152008345EDC00	L7	FO	P	FO
19 Dec 2008	LE70551162008354ASN00	L7	FO	P	FO
21 Dec 2008	LE70531162008356EDC00	L7	FO	P	FO
30 Dec 2008	LE70521162008365ASN00	L7	P	P	P
22 Jan 2009	LE70531162009022EDC00	L7	P	P	P
29 Jan 2009	LE70541162009029EDC00	L7	P	P	P
16 Feb 2009	LE70521162009047EDC00	L7	P	P	P
23 Feb 2009	LE70531162009054EDC00	L7	P	P	P
4 Nov 2009	LE70551162009308EDC00	L7	P	P	P
15 Dec 2009	LE70541162009349EDC00	L7	P	P	P
18 Jan 2010	LE70521162010018EDC00	L7	P	P	P
23 Jan 2010	LE70551162010023EDC00	L7	P	P	P
8 Feb 2010	LE70551162010039EDC01	L7	P	P	P
10 Feb 2010	LE70531162010041EDC00	L7	P	P	P
18 Nov 2010	LE70521162010322EDC00	L7	P	P	P
9 Dec 2010	LE70551162010343EDC00	L7	P	P	P
20 Dec 2010	LE70521162010354EDC00	L7	P	P	P
25 Dec 2010	LE70551162010359EDC00	L7	P	P	P
17 Jan 2011	LE70561152011017EDC00	L7	P	P	P
28 Jan 2011	LE70531162011028EDC00	L7	P	P	P
4 Feb 2011	LE70541162011035EDC00	L7	P	P	P
6 Feb 2011	LE70521162011037EDC00	L7	P	P	P
1 Nov 2011	LE70561152011305EDC00	L7	P	P	P
3 Nov 2011	LE70541162011307EDC00	L7	P	P	P
8 Nov 2011	LE70571152011312EDC00	L7	P	P	P
17 Nov 2011	LE70561152011321ASN00	L7	P	P	P
28 Nov 2011	LE70531162011332EDC00	L7	P	P	P
14 Dec 2011	LE70531162011348EDC00	L7	P	P	P
28 Dec 2011	LE70551162011362ASN00	L7	P	P	P

Table 3.1 continued:

Date	Image ID	Sensor	Ring	Peanut Lobe 1	Peanut Lobe 2
30 Dec 2011	LE70531162011364EDC00	L7	P	P	P
13 Jan 2012	LE70551162012013ASN00	L7	P	P	P
15 Jan 2012	LE70531162012015EDC00	L7	P	P	P
20 Jan 2012	LE70561152012020ASN00	L7	P	P	P
31 Jan 2012	LE70531162012031EDC00	L7	P	P	P
7 Feb 2012	LE70541162012038ASA00	L7	P	P	P
9 Feb 2012	LE70521162012040ASA00	L7	P	P	P
21 Feb 2012	LE70561152012052ASN00	L7	P	P	P
23 Feb 2012	LE70541162012054ASA00	L7	P	P	P
3 Nov 2012	LE70561152012308ASA00	L7	P	P	P
14 Nov 2012	LE70531162012319EDC00	L7	P	P	P
5 Dec 2012	LE70561152012340ASN00	L7	P	P	P
28 Dec 2012	LE70571152012363ASN00	L7	P	P	P
1 Jan 2013	LE70531162013001EDC00	L7	P	P	P
10 Jan 2013	LE70521162013010ASN00	L7	P	P	P
17 Jan 2013	LE70531162013017ASA00	L7	P	P	P
24 Jan 2013	LE70541162013024ASA00	L7	P	P	P
31 Jan 2013	LE70551162013031ASN00	L7	P	P	P
7 Nov 2013	LC80551162013311LGN01	L8	P	P	P
18 Nov 2013	LC80521162013322LGN01	L8	P	P	P
30 Nov 2013	LC80561152013334LGN02	L8	P	P	P
4 Dec 2013	LC80521162013338LGN01	L8	P	P	P
9 Dec 2013	LC80551162013343LGN02	L8	P	P	P
23 Dec 2013	LC82261282013357LGN01	L8	P	P	P
27 Dec 2013	LC80531162013361LGN01	L8	P	P	P
30 Dec 2013	LC82271282013364LGN01	L8	P	P	P
1 Jan 2014	LC82251282014001LGN01	L8	P	P	P
5 Jan 2014	LC82211292014005LGN01	L8	P	P	P
8 Jan 2014	LC82261282014008LGN00	L8	P	P	P
19 Jan 2014	LC80541162014019LGN01	L8	P	P	P
3 Nov 2014	LC80541162014307LGN01	L8	P	P	P
10 Nov 2014	LC80551162014314LGN01	L8	P	P	P
17 Nov 2014	LC82251282014321LGN01	L8	P	P	P
21 Nov 2014	LC80521162014325LGN01	L8	P	P	P
5 Dec 2014	LC80541162014339LGN01	L8	P	P	P
10 Dec 2014	LC80571152014344LGN01	L8	P	P	P
28 Dec 2014	LC82241282014362LGN01	L8	P	P	P
30 Dec 2014	LC80531162014364LGN01	L8	P	P	P
11 Jan 2015	LC82261282015011LGN01	L8	P	P	P
22 Jan 2015	LC80541162015022LGN01	L8	P	P	P
29 Jan 2015	LC82241282015029LGN01	L8	P	P	P
14 Feb 2015	LC80551162015045LGN01	L8	P	P	P
16 Feb 2015	LC80531162015047LGN01	L8	P	P	P
27 Nov 2015	LC82261282015331LGN01	L8	P	P	P
29 Nov 2015	LC82241282015333LGN01	L8	P	P	P
1 Dec 2015	LC80531162015335LGN01	L8	P	P	P
13 Dec 2015	LC82261282015347LGN01	L8	P	P	P
15 Dec 2015	LC80551162015349LGN01	L8	P	P	P
14 Jan 2016	LC82261282016014LGN02	L8	P	P	P
8 Nov 2016	LC80541162016313LGN01	L8	P	P	P
15 Nov 2016	LC82241282016320LGN01	L8	P	P	P
29 Nov 2016	LC82261282016334LGN01	L8	P	P	P
12 Dec 2016	LC82211292016347LGN01	L8	P	P	P
2 Jan 2017	LC82241282017002LGN01	L8	P	P	P
11 Jan 2017	LC82231282017011LGN01	L8	P	P	P
18 Jan 2017	LC82241282017018LGN01	L8	P	P	P

Table 3.1 continued:

Date	Image ID	Sensor	Ring	Peanut Lobe 1	Peanut Lobe 2
25 Jan 2017	LC80561152017025LGN01	L8	P	P	P
4 Nov 2017	LC80531162017308LGN00	L8	P	P	P
13 Nov 2017	LC80521162017317LGN00	L8	P	P	P
25 Nov 2017	LC80561152017329LGN00	L8	P	P	P
27 Nov 2017	LC80541162017331LGN00	L8	P	P	P
29 Nov 2017	LC80521162017333LGN00	L8	P	P	P
2 Dec 2017	LC80571152017336LGN00	L8	P	P	P
15 Dec 2017	LC80521162017349LGN00	L8	P	P	P
7 Jan 2018	LC80531162018007LGN00	L8	P	P	P
19 Jan 2018	LC80571152018019LGN00	L8	P	P	P

CHAPTER 4

MODELLING THE EFFECT OF PEDESTALLED, RELICT LAKE FORMATION ON ICE-SHELF FLEXURE

4.1 Introduction

As temperatures rise with climate change, the stability and future of the Antarctic Ice Sheet (AIS) is closely related to the future of the ice shelves (e.g. DeConto and Pollard, 2016; Rignot and others, 2019) that surround ∼75% of its perimeter (Bindschadler and others, 2011). Ice shelves buttress grounded outlet glaciers that feed into them (e.g. Scambos and others, 2004; Dupont and Alley, 2005; De Rydt and others, 2015), and when this buttressing effect is removed it can cause these glaciers to accelerate (e.g. Rignot and others, 2004; Rott and others, 2011; Mouginot and others, 2015), leading to loss of ice and to sea-level rise.

Lakes form on numerous ice shelves around Antarctica (e.g. Kingslake and others, 2017; Langley and others; Stokes and others, 2019) and on floating ice tongues around Greenland (e.g. Macdonald and others, 2018), and climate change is predicted to increase surface melting on both Antarctica's and Greenland's margins (Trusel and others, 2015; Bell and others, 2018; Bevis and others, 2019). Modelling (Banwell and others, 2013; MacAyeal and Sergienko, 2013; Banwell and MacAyeal, 2015) and field studies (Banwell and others, 2019) have shown that filling and draining of lakes can be hazardous to ice-shelf stability due to their influence on ice-shelf flexure and fracture. For example, it is thought that the almost complete collapse of the Larsen B Ice Shelf in 2002 was in response to the drainage of ∼3000 lakes (Glasser and Scambos, 2008) through a chain reaction style drainage process (Banwell and others, 2013).

Previous studies of the role of meltwater lakes in ice-shelf flexure, and therefore instability, have focused on the effect of lakes filling and draining, a process which can cause fractures to form both within, and at a distance from, lake basins (Banwell and others, 2013; Banwell and MacAyeal, 2015; MacAyeal and others, 2015). However, in a recent study we documented

an additional lake process that we suggested could cause ice-shelf flexure: one that does not depend on water movement (draining and/or re-filling) (Macdonald and others, 2019). This process involves the formation of pedestalled, relict lakes, features which hereafter we refer to as 'pedestals'. These pedestals form in response to large spatial contrasts in ablation, i.e. 'differential ablation' (Macdonald and others, 2019). This process of differential ablation leads to the necessity of the ice shelf to flex at the boundaries between areas experiencing different ablation rates, because the different areas of the ice shelf must settle by different amounts into the ocean to maintain hydrostatic equilibrium.

We found that surface lakes can evolve into pedestals in the debris-covered zone of the McMurdo Ice Shelf (McMIS; Macdonald and others, 2019). When such an open-water surface lake freezes over during the winter and remains frozen-over during the subsequent summer, the low-albedo debris at the bottom of the surface lake becomes masked by a high-albedo ice surface. The high albedo of the surface of the frozen lake causes it to melt more slowly than the surrounding lower albedo, debris-covered areas, causing differential ablation to occur. This differential ablation between the frozen lake and its surroundings, and the development of a ring-like depression around the pedestal caused by ice flexure, causes the frozen lake to become pedestalled above the high-ablation surrounding area. Figure 4.1 depicts the latter stage of the pedestal formation process. The pedestalled nature of the feature causes it to become hydrologically isolated, preventing surface meltwater and entrained debris from flowing onto the feature, helping to maintain its frozen, high-albedo, low-ablation frozen surface. We have previously suggested that a sustained contrast in ablation rates between different areas of an ice shelf will produce a significant contrast in ice-shelf thickness, which in turn, may drive contrasting buoyancy forces, and an associated flexural response (Macdonald and others, 2019).

Here we seek to further investigate this idea and to better understand the flexural response of ice shelves to the formation of pedestals and concentrated spatial contrasts in ablation. To do so, we use an elastic flexure model to simulate the influence of idealized pedestals on

the surface profile and stress regime of the ice shelf, and to assess the implications of the results for the stability of the ice shelf. The results of our study will aid understanding of how the McMIS, and other ice shelves, will respond to the formation of pedestals, and it will also contribute to our overall understanding of how ice-shelf stability may be affected in a changing climate.

This chapter is organized as follows: First, we consider a conceptual model of elastic ice-shelf flexure in response to pedestal formation using springs and buckets. Second, we describe the equations that underpin our elastic model of ice-shelf flexure. Third, we outline each set of model runs and how parameters vary between them. Fourth, we describe the results of each model run. Fifth, we discuss the implications of these results for the stability of the McMIS and other ice shelves. Finally, we summarize our main conclusions and put them in the wider context of ice-shelf stability.

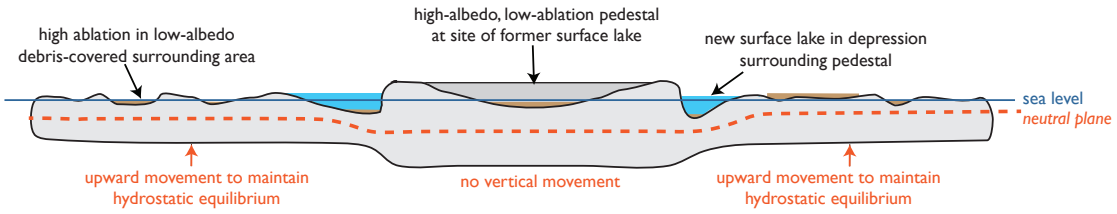

Fig. 4.1: Schematic illustration of a pedestal and the surrounding area on a debris-covered ice shelf surface, based on analysis of observations (*Source: Adapted from Fig. 3 in Macdonald and others (2019)).*

4.2 Conceptual model of ice-shelf flexure in response to pedestal formation

Before outlining the model we use to drive our simulations, it is helpful to consider a conceptual model of the situation. In this conceptual model, one area of the ice shelf is undergoing minimal change to ice thickness (because albedo is high and ablation is low, such as a pedestal) and a surrounding, adjacent, area of the ice shelf is undergoing a large change in ice thickness due to thinning (because albedo is low and ablation is high, such as the debris-

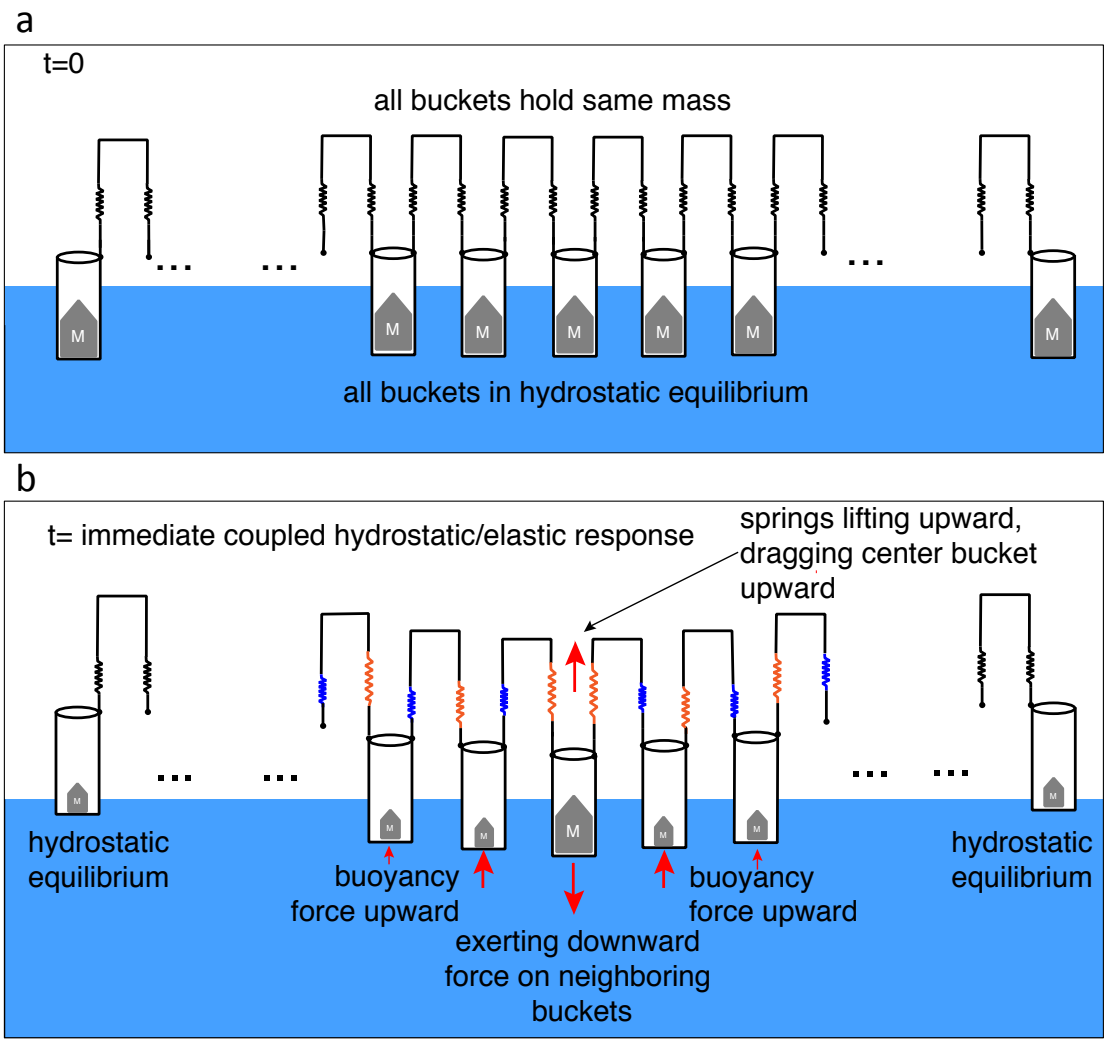

Fig. 4.2: Schematic illustration of the idealized spring and buoyancy bucket system that acts as a conceptual metaphor for the response of a floating ice shelf to pedestal-associated differential ablation. (a) represents before differential ablation has occurred and (b) after. Each bucket represents an ice column, with the central bucket representing the pedestal. Each bucket is connected by a rigid beam to its neighbour, meaning that they do not act independently of each other. The M in each bucket represents mass, and the size of M represents the amount of mass. Red springs are elongated and blue springs are compressed.

covered area surrounding a pedestal). Our conceptual model is illustrated in the schematic diagram shown in Fig. 4.2. Each bucket represents an individual ice column containing a mass M. Buckets are linked to their two neighbours via an arch-like rigid beam and therefore do not act independently of each other. At time $t = 0$, all buckets contain the same mass M and float in perfect hydrostatic equilibrium in the ocean where the buoyancy force

introduced at the bottom of the bucket exactly cancels the weight of the mass within the bucket (Fig. 4.2a).

At a point in time (an instant after $t = 0$) all apart from the central 'pedestal' bucket lose an amount of mass ΔM, as represented by the smaller mass weights in the surrounding buckets in Fig. 4.2b. This loss of mass represents a sudden occurrence of ablation at the surface of the ice shelf. To represent the area of high albedo/low ablation (the pedestal), the central bucket is kept unchanged, and has the same mass as initially. At this instant, before any motion or deformation takes place, all buckets, except the one in the centre, feel a buoyancy force on their bottom that exceeds the weight of the mass in the bucket. These outer buckets are now out of hydrostatic equilibrium, and thus must respond by moving upwards.

Moments after this, the buckets with reduced mass will have moved upwards because there is a hydrostatic pressure imbalance at their base (Fig. 4.2b). The centre bucket, which has not lost mass, however, does not have an impetus to move upwards, because it is in hydrostatic balance. The two buckets on either side of the centre bucket will elongate the two springs that are attached to the centre bucket as they move upwards. Because the centre bucket was not out of hydrostatic equilibrium, the elongation of the springs that connect it to the two neighbouring buckets will cause it to anomalously rise to a higher elevation, thus rendering the hydrostatic pressure at its base slightly less than what would be required for the bucket's hydrostatic equilibrium. Coupled with the elongation of the springs coming from the centre bucket to its two neighbours, the springs that come from the two neighbouring buckets will compress, because the centre bucket is exerting a downward force on the two neighbouring buckets. The buckets neighbouring the centre bucket will also be influenced by the fact the buckets on their outer-side are moving upward in response to the reduction of weight inside them too. This will result in a cascade of spring elongation and compression that will eventually approach a situation where, far enough from the centre of the array, all buckets will approach being in hydrostatic equilibrium, with no stretching or compression

on the springs that connect them to their neighbours. The length scale over which the spring-action decays to no compression/elongation due to reaching hydrostatic equilibrium is analogous to the flexural length scale of a thin elastic plate, which is what we are treating the McMIS to be.

4.3 Elastic model of ice-shelf flexure in response to pedestal formation

The simplest treatment of ice-shelf flexure response to a changing pattern of ice thickness, due to differential ablation at the surface, is to assume the ice shelf is purely elastic. A previous study (MacAyeal and others, 2015) uses a viscoelastic rheology to study ice-shelf flexure, but we use an elastic model because it is simple and is able to predict the maximum stress field even if the phenomenon is viscoelastic (MacAyeal and Sergienko, 2013). The elastic treatment requires the ice shelf to adopt a flexural profile and associated flexural stresses that are in instantaneous equilibrium with the differential ice thickness. This means that the ice-shelf deflection is not a function of time. The governing equations written for the axisymmetric geometry (central low-ablation pedestal surrounded by high-ablation debris-covered ice shelf) considered here, in our elastic model run in COMSOL$^{\mathrm{TM}}$, are:

$$-\frac{\partial^2 M_{rr}}{\partial r^2} - \frac{2}{r}\frac{\partial M_{rr}}{\partial r} + \frac{1}{r}\frac{\partial M_{\theta\theta}}{\partial r} + \rho_{sw} g \eta(r,t) \;=\; F(r,t) \tag{4.1}$$

$$\mathbf{M} = \mathbf{D}\mathbf{H} \tag{4.2}$$

where

$$\mathbf{M} = \begin{bmatrix} M_{rr} \\ M_{\theta\theta} \end{bmatrix} \quad , \quad \mathbf{H} = \begin{bmatrix} \dfrac{\partial^2 \eta}{\partial r^2} \\ \dfrac{1}{r}\dfrac{\partial \eta}{\partial r} \end{bmatrix} \tag{4.3}$$

and

$$\mathbf{D} = -\frac{EH^3}{12\left(1-\mu^2\right)}\begin{bmatrix} 1 & \mu \\ \mu & 1 \end{bmatrix} \tag{4.4}$$

where r is pedestal radius (as defined for each model run) and $r = 0$ defines the centre of the pedestal, H is ice thickness (as defined for each model run), t is time (0 before the model run and an instant after 0 at the end of the run), $E = 1$ GPa is Young's modulus of elasticity, $\mu = 1/3$ is the Poisson ratio, ρ_{sw}= 1030 kg m^3 is the density of sea water, and $g = 9.81$ m s^{-2} is the gravitational acceleration. The curvature of the flexed ice shelf is represented by the vector **H**. This curvature is related to the bending moment **M** by an elastic relation embodied by the matrix **D**. The ratio in the matrix **D** given by

$$\frac{EH^3}{12\left(1-\mu^2\right)} \tag{4.5}$$

is called the flexural rigidity, and is commonly seen in problems involving the flexure of thin plates. We note that it is a function of H^3, the cube of the ice thickness. Hence, we anticipate that the flexural amplitude and length scales will be strongly influenced by ice thickness, with thicker ice representing stiffer conditions. What are referred to as 'flexural stresses' are embedded in the definition of bending moments (**M** in the above equation). These moments are the integral of the product of the stress, times the vertical distance from the ice shelf centre integrated over the thickness of the ice shelf.

The variable F on the right-hand side of equation (4.1) is the vertical force applied to the ice shelf associated with addition or removal of mass due to differential ablation. Under the assumptions of the study being undertaken, surface ablation gives

$$F(r,t) = -\rho_i g \int_0^t A'(r,t')\mathrm{d}t' > 0 \tag{4.6}$$

In simulations presented here, the ablation value A' will be zero where r is less than the pedestal's radius (i.e. there is no ablation on the pedestal) and A' will have a defined

value where r is greater than the pedestal's radius (i.e. there is a defined ablation value for the area surrounding the pedestal). A' will occur 'instantaneously' (between $t = 0$ and an instant after $t = 0$) .

4.4 Model run initialization and parameters

Table 4.1: Values and ranges of parameter values used in each model run/model run groups.

Model Run	Initial ice shelf thickness (H)	Pedestal radius (r_{p})	Ablation (A')
A	30 m	500 m	3 m (10% of thickness)
Group B	10-1000 m	500 m	3 m
Group C	10-1000 m	500 m	10% of thickness
Group D	30 m	50-1000 m	3 m (10% of thickness)

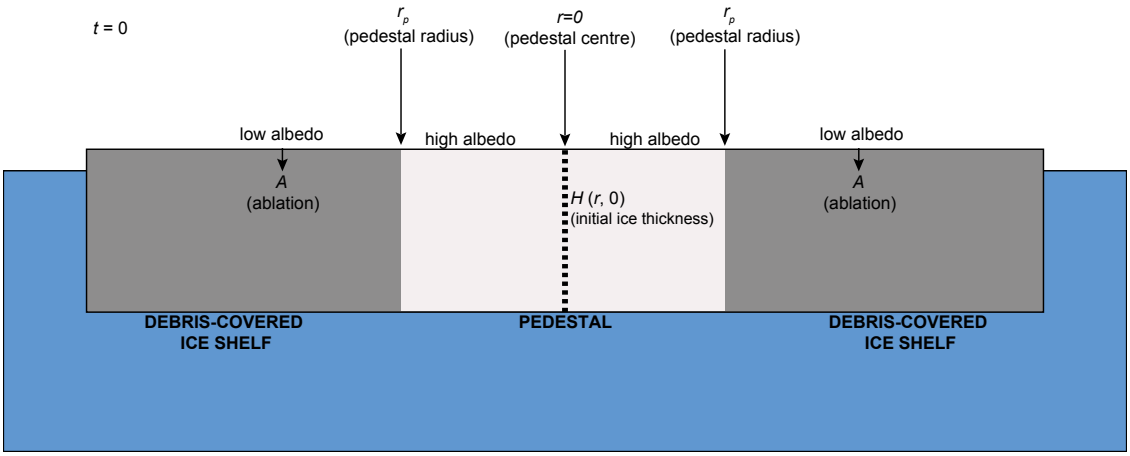

Fig. 4.3: Idealized geometry of an ice shelf used as the domain in our elastic model. The central high albedo area develops into a pedestal as differential ablation occurs.

We set up a model of the elastic response of an ice shelf to an axisymmetric feature experiencing no ablation surrounded by an area experiencing high ablation, to represent an idealized version of the high albedo and low albedo areas respectively (Fig. 4.3). One individual model run (A) and three groups of model runs (B-D) were produced. Each model run/model run group was initiated with different parameters, as summarized in Table 4.1 and described below.

In Model Run A, we aimed to analyse the surface profile produced by pedestal evolution. Pedestal radius, r_{p}, was set at 500 m, which is approximately the radius of 'Ring pedestal' in Macdonald and others (2019). The initial ice thickness, $H\ (r,\ 0)$, was taken to be 30 m, which is approximately the thickness of the McMIS in the area (Campbell and others, 2017). Ablation, A', was set at 3 m in the low albedo, debris-covered ice shelf region and $A' = 0$ m for the pedestal site.

In Model Runs Group B, we aimed to analyse the effect that initial ice-shelf thickness had on the stress produced by pedestal evolution. Pedestal radius, r_{p} was set at 500 m, the initial ice thickness, $H\ (r,\ 0)$, was set at values between 10 and 1000 m, inclusive, and ablation, A', was set at 3 m for the debris-covered ice shelf, regardless of ice-shelf thickness. $A' = 0$ m for the pedestal.

In Model Runs Group C, as with B, we aimed to analyse the effect that initial ice-shelf thickness had on the stress produced by pedestal evolution, but in this case we set a different value for the ablation parameter. Pedestal radius, r_{p} was set at 500 m, the initial ice thickness, $H\ (r,\ 0)$ was set at values between 10 and 1000 m, inclusive. In contrast to Model Runs Group B, in Model Runs Group C, ablation, A' was set at 10% of ice-shelf thickness for the debris-covered ice shelf and $A' = 0$ m for the pedestal.

In Model Runs Group D, we aimed to analyse the effect that pedestal radius had on the stress produced by pedestal evolution. Initial ice thickness, $H\ (r,\ 0)$, was set at 30 m, ablation, A' was set at 3 m for the debris-covered ice shelf and $A' = 0$ m for the pedestal. The radius of the high ablation area, r_{p}, was set at values between 50 and 1000 m, inclusive.

For Model Run Groups B-C, the maximum von Mises stress was calculated for each run, i.e. for each ice thickness that the model was initiated with. The von Mises stress, which is always positive, can be used as a diagnostic for fracture initiation (Albrecht and Levermann, 2012; Banwell and others, 2013). For Model Runs Group D, the von Mises stress was calculated for each run, i.e. for each pedestal radius that the model was initiated with. The von Mises stress was calculated at the top and bottom of the ice column; the two places

where this stress is highest.

4.5 Results

4.5.1 Model Run A: Response of ice-shelf surface profile

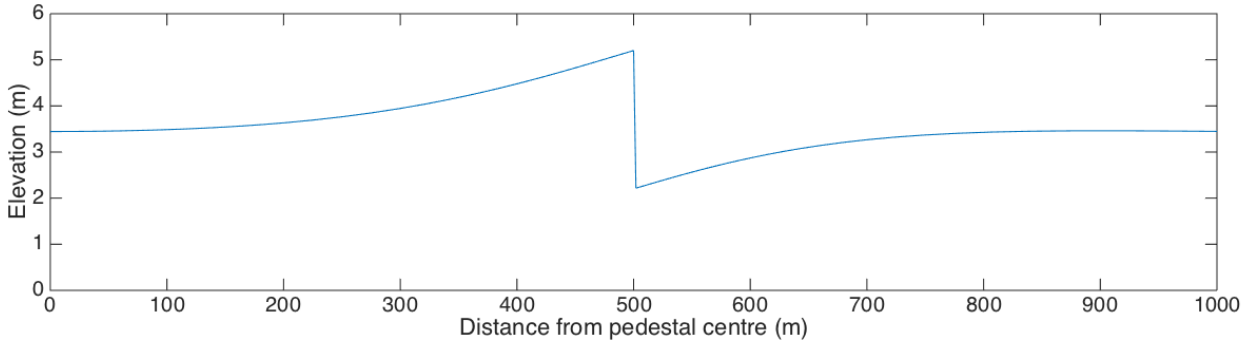

Fig. 4.4: The surface profile of the ice shelf produced by Model Run A, from the centre of the pedestal at 0 m ($r = 0$). The pedestal has a radius of 500 m, initial ice thickness is 30 m and 3m of ice-shelf thickness is ablated on the debris-covered ice shelf.

The surface profile produced by pedestal evolution shows that the centre of the pedestal is slightly raised above the outer part of the debris-covered ice shelf, with a surface elevation of 3.5 m at the centre of the pedestal compared to 3.4 m at 800-1000 m from the centre (Fig. 4.4). Towards the outer margins of the pedestal, the elevation of the surface rises compared to the centre, reaching a peak elevation of 5.2 m at 500 m from the centre. Adjacent to the pedestal, a depression forms. The depression is at its lowest point immediately adjacent to the pedestal (500 m from the pedestal centre), with an elevation of 2.2 m. From 500 to 800 m from the pedestal centre the elevation increases until it plateaus at 3.4 m from 800 to 1000 m from the pedestal centre.

4.5.2 Model Runs Group B: Stress response to varying initial ice thickness

In Model Runs Group B, where initial ice-shelf thickness is varied for each model run and the debris-covered ice shelf is subject to a fixed 3 m of ablation regardless of initial thickness,

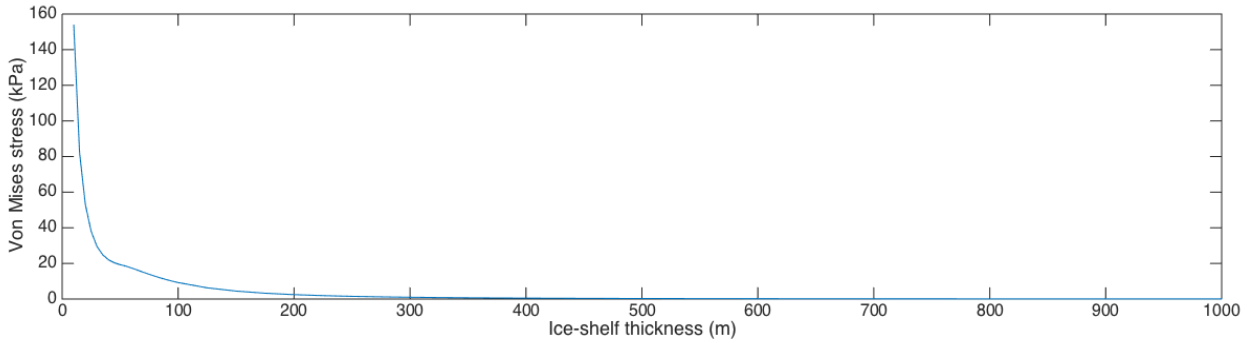

Fig. 4.5: The maximum von Mises stress produced by pedestal formation with different initial ice-shelf thicknesses in Model Runs Group B. The pedestal has a radius of 500 m and 3m of ice-shelf thickness is ablated on the debris-covered ice shelf. The von Mises stress was calculated at the top and bottom of the ice column.

the maximum von Mises stress reaches a peak of 154 kPa at the top/bottom of the ice shelf when the model is initiated with an ice shelf thickness of 10 m (Fig 4.5). However, from the peak, maximum von Mises stress declines steeply as initial thickness increases. For example, for an initial thickness of 20 m, the maximum von Mises stress reduces to 54 kPa. As initial thickness increases further, the maximum von Mises stress declines less steeply. At 30 m initial thickness, the maximum von Mises stress is 30 kPa, for 50 m it is 19 kPa and for 200 m it is 2 kPa. For an initial thickness of 300-1000 m, the maximum von Mises stress plateaus at approximately zero.

4.5.3 Model Runs Group C: Stress response to varying initial ice thickness

In Model Runs Group C, where initial ice-shelf thickness is varied for each model run and the debris-covered part of the ice shelf has 10% of its initial thickness ablated, the maximum von Mises stress reaches a peak of 48 kPa when initial thickness is set at 10 m (Fig 4.6). The maximum von Mises stress drops steeply alongside initial thickness to 29 kPa for an initial thickness of 35 m, but from there it increases with initial thickness to 35 kPa for 65-70 m initial thickness. From 70 m initial thickness upwards, the stress decreases constantly, to 31 kPa at 100 m initial thickness and 17 kPa at 200 m initial thickness.

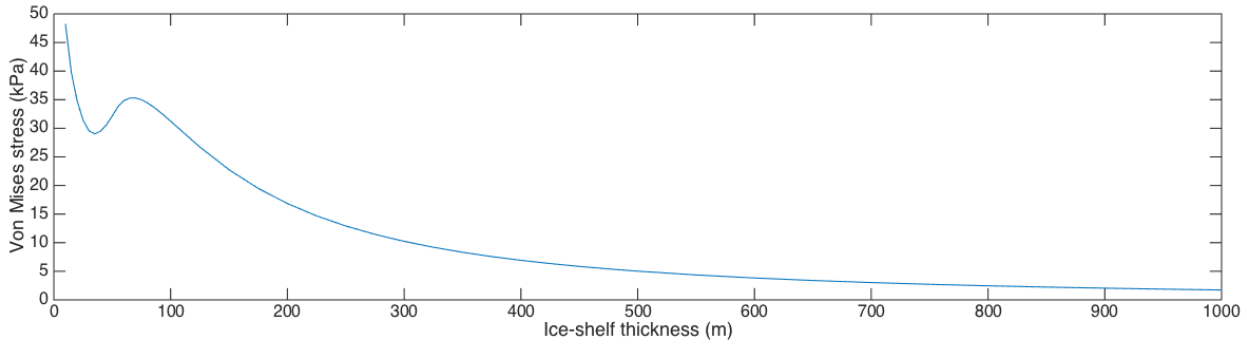

Fig. 4.6: The maximum von Mises stress produced by pedestal formation with different initial ice-shelf thicknesses in Model Runs Group C. The pedestal has a radius of 500 m and 10% of initial ice-shelf thickness is ablated on the debris-covered ice shelf. The von Mises stress was calculated at the top and bottom of the ice column.

4.5.4 Model Runs Group D: Stress response to varying pedestal radius

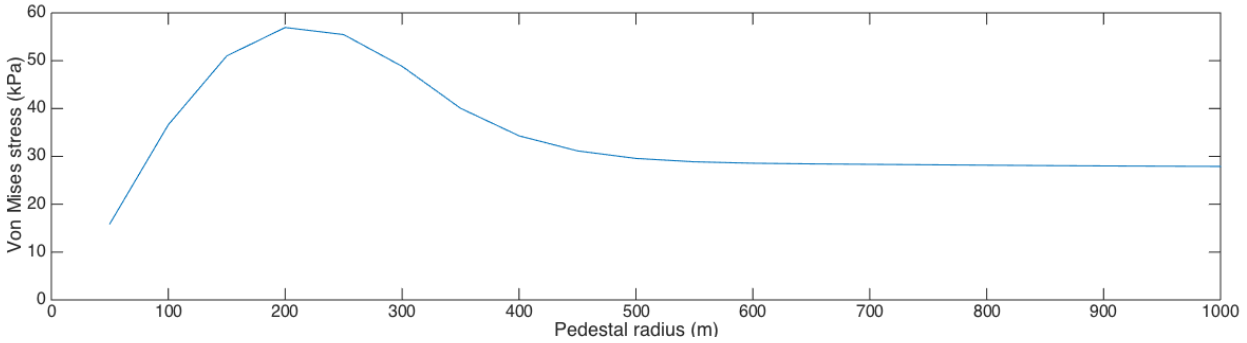

Fig. 4.7: The maximum von Mises stress produced by pedestal formation with different pedestal radius values in Model Runs Group D. The ice shelf has an initial thickness of 30 m and 10% of initial ice-shelf thickness is ablated on the debris-covered ice shelf. The von Mises stress was calculated at the top and bottom of the ice column.

In Model Runs Group D, where the pedestal radius is varied for each model run, initial ice-shelf thickness (30 m) is fixed and the debris-covered part of the ice shelf undergoes 3 m of ablation, the maximum von Mises stress increases alongside radius at lower radius values but then declines and plateaus as radius is increased further (Fig. 4.7). At a minimum pedestal radius of 50 m, the maximum von Mises stress is 16 kPa and it increases to its peak of 57 kPa when the pedestal radius is 200 m. As the pedestal radius increases from 200 m, the maximum von Mises stress declines steeply to a radius of around 600 m, where the maximum stress is 28 kPa. For a pedestal radius of 600-1000 m, the maximum von Mises

stress remains approximately the same.

4.6 Discussion

4.6.1 Consequences of pedestal formation for ice-shelf surface profile

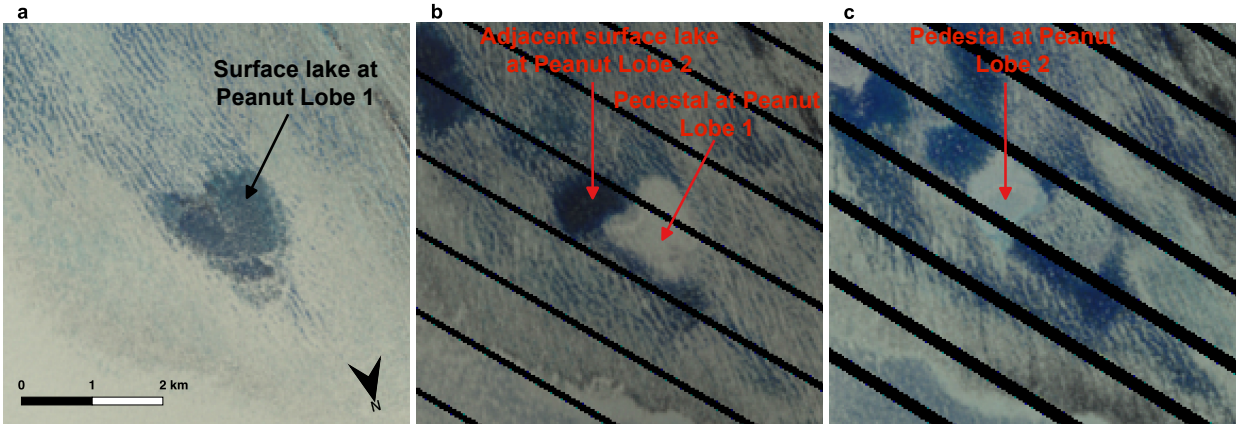

Fig. 4.8: After (a) a surface lake forms at the site of Peanut Lobe 1 (Fig. 3.1 in Chapter 3) on the, McMurdo Ice Shelf(b) this site develops into a pedestal and another surface lake develops adjacently (c) which subsequently also develops into a pedestal. Images are true-colour Landsat 7 images dated (a) 5 December 2002, (b) 2 February 2007 and (c) 30 December 2008.

The results of Model Run A (Fig. 4.4) show that the flexural processes and ablation associated with pedestal formation have an important influence on the surface profile of the ice shelf. First, the pedestal, especially the outer portion of it, becomes raised ('pedestalled') relative to the surroundings. This happens both because its surface has not lowered from ablation of ice/snow and because its outer portion deflects upward under the influence of the debris-covered ablating areas that move upward. The debris-covered area moves upward because the ablation causes thinning and an associated hydrostatic buoyancy imbalance (Fig. 4.2b). Second, these flexural processes cause a ring-like depression to form around and directly adjacent to the pedestal. This depression forms at the boundary between the pedestal and the debris-covered part of the ice shelf, where the downward force being exerted by the pedestal on the thinned debris-covered part is strongest (Fig. 4.2b).

Observations of pedestal formation by Macdonald and others (2019) support the suggestion that a depression forms adjacent to a pedestal. After 'Peanut Lobe 1' (Fig. 3.1 in Chapter 3) formed as an open-water surface lake in 2002 (Fig. 4.8a) it is visible as a pedestal in the 2004/2005 summer onwards. After the site had developed into a pedestal, an open-water surface lake formed directly adjacent to it (Fig. 4.8b), suggesting that the area was in a depression. This adjacent lake site also subsequently became a pedestal, 'Peanut Lobe 2' (Fig. 4.8c). Lakes and streams also developed directly adjacent to the other pedestal, 'Ring Pedestal', studied in Macdonald and others (2019).

The rising elevation towards the margin of the pedestal (Fig. 4.4) was not observed by Macdonald and others (2019) in the field. However, it is possible that it existed but was undetected, or that other processes that our model does not account for counter its formation.

4.6.2 Stress response to pedestal formation on ice shelves of different thicknesses

In both model run groups where the ice shelf is initiated with different initial ice-shelf thicknesses, Model Runs Groups B and C, the peak maximum von Mises stress occurs when the ice shelf has an initial thickness of 10 m, the lowest initial thickness that the model is run with (Figs. 4.5 and 4.6). The peak level of maximum von Mises stress reached in Model Run Group B (Fig. 4.5), when 3 m of ablation occurs for all initial thicknesses, is 154 kPa, which may be sufficient to cause fracture initiation. Although Banwell and others (2019) modelled von Mises stresses to exceed 300 kPa when a lake drained on the McMIS, and they did not observe the initiation of a fracture, Albrecht and Levermann (2012) suggest a von Mises stress of 70 kPa is sufficient for fracture initiation. Banwell and others (2013) also use a von Mises stress of 70 kPa as a threshold for fracture initiation in their modelling study of flexure on the Larsen B Ice Shelf. The peak maximum von Mises stress (48 kPa) reached in Model Run Group C (Fig. 4.6), when 10% of initial thickness is ablated, is, however, below

this 70 kPa fracture threshold. For all other initial thicknesses in Model Run Groups B and C, the maximum von Mises stress is also below this fracture threshold.

The relationship between maximum von Mises stress and initial ice-shelf thickness presented in Fig. 4.5 and Fig. 4.6 suggests that, as expected, the thinner an ice shelf is, the more the stress regime is affected by pedestal evolution (with some exception in Fig. 4.6). However, using the suggested fracture threshold of 70 kPa (Albrecht and Levermann, 2012) suggests that only a very thin ice shelf (∼10 m) would be vulnerable to fracturing and ice-shelf instability from pedestal formation. Importantly, even an ice-shelf as thin as the McMIS (∼30 m), the only location where pedestals have been documented, would not be vulnerable to fracturing under these conditions. Although we are not aware of any ice shelf with a thickness as low as 10 m, ice-shelf thinning due to climate change means that the McMIS, or another ice shelf, could become this thin in the future. At the McMIS, 11 mm d^{-1} of ablation was measured on the debris-covered surface and 1 mm d^{-1} on the pedestal surface (Banwell and others, 2019; Macdonald and others, 2019), meaning it would take approximately 300 days for 3 m of differential ablation to occur. This suggests that if the McMIS thins to ∼10 m, it is possible pedestal development could cause fracturing. It is also possible that thinning and exposure of debris on another ice shelf could lead to the potential for pedestal-evolution and associated fracturing elsewhere.

The 'S-curve' in Fig 4.6 (decrease-increase-decrease in stress as initial ice-shelf thickness increases) can be explained by geometric effects, with the lake size and flexural length scale being approximately the same when initial thickness is ∼35-65 m.

4.6.3 Stress response to formation of pedestals of varying radii

Running the model with different pedestal radius values, as in Model Runs Group D, does not lead to the fracture threshold suggested by Albrecht and Levermann (2012) being exceeded in any case. This peak maximum von Mises stress of 57 kPa, for a pedestal radius of 200 m (Fig. 4.7), is significantly below the suggested 70 kPa fracture threshold (Albrecht

and Levermann, 2012). This suggests that the development of the ∼500 m-radius Ring and Peanut pedestals observed on the McMIS (Macdonald and others, 2019) is unlikely to lead to fracture development. Furthermore, neither the development of pedestals smaller nor larger than the Ring and Peanut pedestals is likely to lead to fracture for the present conditions of the McMIS.

The low calculated values of maximum von Mises stress when the pedestal radius is small can be explained by the fact that in this situation, the load of the pedestal is also small, and therefore, the bending moment is low. As the pedestal increases in size, so does the load, and therefore, initially, stress. However, when the radius is sufficiently large, the model's solution asymptotes to a constant. This is because, once the lake is large enough, the flexural effect is so confined to the narrow region along its edge, that the circular geometry becomes effectively indistinguishable from a straight line boundary between a high and low ablation zone. This straight-line geometry has a fixed stress regime that no longer depends on radius.

4.7 Conclusion

We have investigated elastic ice-shelf flexure caused by the evolution of an axisymmetric pedestalled, relict lake. The high-albedo surface of the pedestal undergoes low (or in our model, zero) ablation, in contrast to the surrounding area where ablation is high due to low-albedo debris cover. This high degree of differential ablation causes a contrast in ice thickness between the pedestal site and the surrounding debris-covered ice shelf. As the surrounding area ablates, it must rebound upwards to maintain hydrostatic equilibrium. Our model shows that the resultant flexure has consequences for the surface profile of the ice shelf at, and adjacent to, the pedestal. Notably, it causes a ring-like depression to develop around/directly-adjacent-to the pedestal, which can explain observations of preferential ponding adjacent to pedestals (Macdonald and others, 2019). The ice-shelf flexure also produces stress in the ice shelf. Greater amounts of stress are produced in thinner ice shelves, but at present, sufficient stress to cause fracturing is unlikely, even in an exceptionally thin

ice shelf such as the McMurdo Ice Shelf. The only case where we model sufficient stress to cause fracturing to occur, using a threshold for fracture initiation of 70 kPa, is when a 10 m-thick ice shelf is subject to 3 m of differential ablation. The relationship between pedestal radius and stress is complex, but in no case did varying pedestal radius in our model lead to sufficient stress to cause ice-shelf fracturing. Although we find that pedestal evolution is only likely to cause sufficient flexure to initiate fracturing on an exceptionally thin ice shelf with high ablation, it is conceivable that such conditions could be met in the future at the McMIS or on another Antarctic or Greenland ice shelf, due to ice-shelf thinning caused by air and ocean warming.

CHAPTER 5

FORMATION OF SEA ICE PONDS FROM ICE-SHELF RUNOFF, ADJACENT TO THE MCMURDO ICE SHELF, ANTARCTICA

5.1 Introduction

Ponds that form on sea ice are important for the energy balance of the sea ice and the polar oceans. Sea ice ponds alter the light scattering properties of the ice surface and lower its albedo (Perovich and others 2002; Grenfell and Perovich, 2004). As the lower albedo causes the ice to absorb more solar energy, a positive feedback between melting and ponding can develop (Curry and others, 1995) and enhanced melting of sea ice can cause it to thin or break up (Perovich and others, 2003; Arntsen and others, 2015). Landfast sea ice and ice mélange buttress ice shelves and provide a protective buffer from ocean swells that can weaken ice-shelf fronts, so ice shelves are more prone to calve or disintegrate when landfast sea ice breaks-up or thins (Banwell and others, 2017; Robel, 2017; Massom and others, 2018).

In the Arctic, observations show that when snow and ice on the surface of sea ice melts and the meltwater accumulates in depressions, sea ice ponds form (Polashenski and others, 2012). In the Antarctic, although ponds may form on the sea ice when snow weighs it down and causes seawater to flood its surface (NSIDC, 2019), scientists have rarely observed the presence of ponds formed from meltwater (Andreas and Ackley, 1981).

However, recent studies have documented an additional phenomenon that we suggest could be a mechanism for the formation of sea ice ponds. Surface meltwater streams on ice shelves in both Greenland (Macdonald and others, 2018) and Antarctica (Bell and others, 2017) have been observed to flow over the ice front. Macdonald and others (2019) note that during the melt season, ponds form on sea ice adjacent to the McMurdo Ice Shelf (McMIS), Antarctica. We suggest that sea ice ponds may form when surface meltwater runoff from

ice shelves flows over the ice-shelf front onto the sea ice, particularly in Antarctica, possibly with significant implications for sea-ice stability.

Here, we document and analyze the formation and evolution of sea ice ponds in McMurdo Sound, adjacent to the McMIS, over the austral summers from 2015/2016 to 2018/2019. We do this qualitatively by analyzing satellite image data over the period and quantitatively by using a water-identification algorithm to measure the evolution of ponded area.

5.2 Study Site

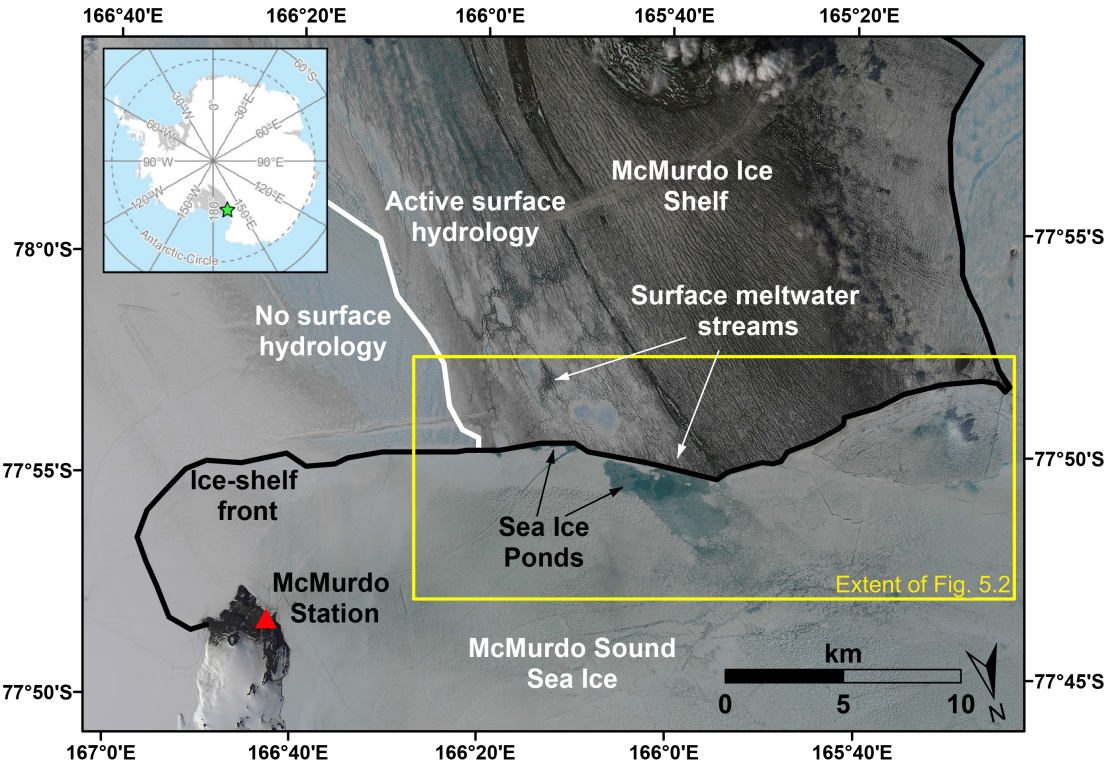

Fig. 5.1: Part of the McMIS and McMurdo Sound sea ice (green star in top-left inset shows location in Antarctica). The background image is a true-colour composite Sentinel 2B image dated 4 January 2019. The white line marks the boundary between the portion of the McMIS where there is an active surface hydrology during the summer, and the portion where there is typically no surface hydrology. The black line marks the boundary between the ice shelf and sea ice. The yellow box marks the study area and extent of the images in Fig. 5.2. Sea ice ponds are visible close to the ice front adjacent to the 'active surface hydrology' portion of the McMIS. The inset map is from Matsuoka and others (2018).

The McMIS is a ∼1500 km^2 ice shelf, located in the northwest corner of the Ross Ice Shelf at 78°S. It abuts the southern tip of Ross Island where the US McMurdo Station and New Zealand Scott Base are located (Fig. 5.1). The ice shelf is relatively thin close to its front (10-30m; Rack and others, 2013; Campbell and others, 2017) and its front faces McMurdo Sound, which is typically covered by landfast sea ice through the summer. February 2016 and February 2019 are the most recent instances of the sea ice breaking out. The breakout of sea ice at the ice-shelf front in 2016 was associated with calving of icebergs from the ice shelf and the propagation of a rift by ∼3 km on the ice shelf (Banwell and others, 2017).

The western portion of the McMIS is heavily covered by debris, primarily due to the redistribution of sediment from the Black Island Medial Moraine (BIMM) (Glasser and others 2006; 2014). Largely due to the effect of the debris on the energy balance of the surface (Glasser and others, 2006), during the summer the McMIS has an active surface (and subsurface) hydrology in its western portion (MacAyeal and others, 2018), where lakes and surface streams form (Banwell and others, 2019; Macdonald and others, 2019). These surface streams are forced to divert around 'pedestalled relict lake' features. To the east of the 'active surface hydrology' part of the ice shelf is an area where subsurface water is present but typically not surface water, and further east is a dry snow zone (Klokov and Diemand, 1995; Macdonald and others, 2019).

We focus our analysis in and around the area where ponds form on the sea ice abutting the 'active surface hydrology' part of the ice shelf (Fig. 5.1).

5.3 Data and Methods

We acquired a time series of completely- or partially-cloud-free Landsat 8 and Sentinel-2 images over the study site (Fig. 5.1) for the period from 29 November 2015 to 24 January 2019 (Table 5.1). This period covers the entire breadth of the lifecycle of the McMurdo Sound multi-year sea ice that formed in 2016 and broke-out in 2019 and the sea ice that only lasted for the 2015/2016 season.

First, we analysed how the sea ice ponds form and evolve by visually inspecting the true-color satellite images, with a particular focus on the study site area (Fig. 5.1).

Second, to quantify the evolution of sea ice ponds, we used the normalized difference water index adapted for ice ($NDWI_{ice}$) method (see Section 5.6.1). The method uses the red and blue bands for both types of satellite to identify water-covered pixels, from which we calculated the ponded area on the sea ice at our study site for all quality images.

5.4 Observations and Discussion

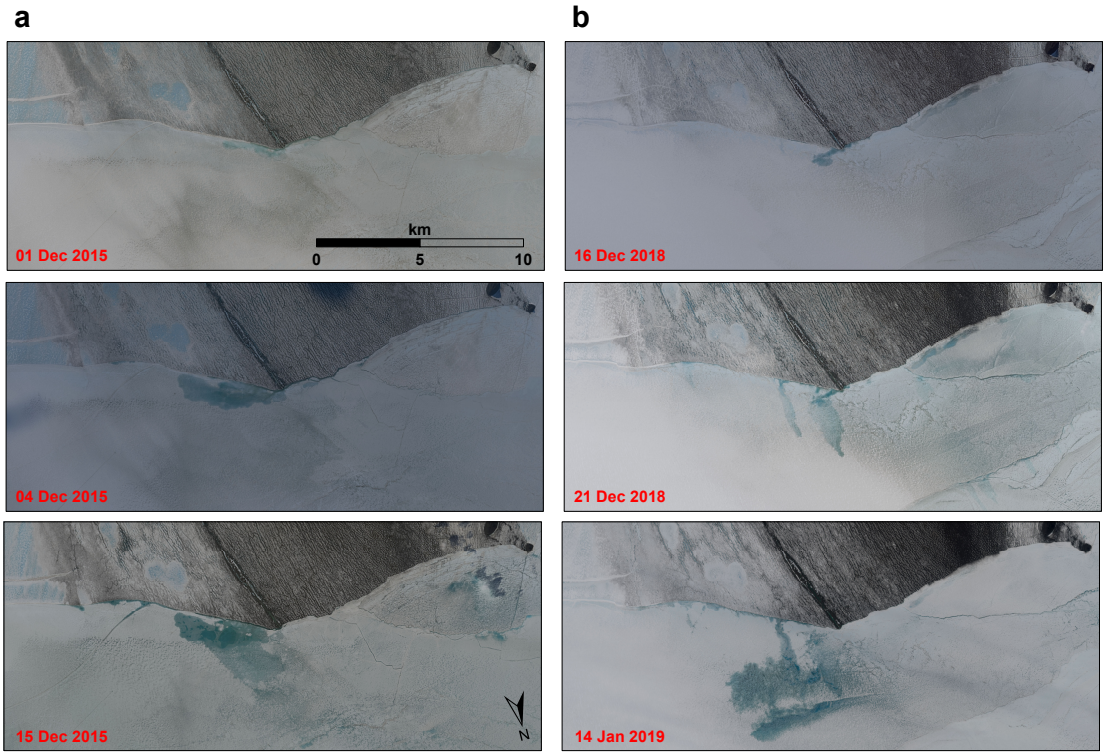

Fig. 5.2: The development of sea ice ponds adjacent to the 'active surface hydrology' portion of the McMIS in the 2015/2016 and 2018/2019 austral summers. The extent of each image is shown in Fig. 5.1. The image IDs for the complete time-series of all 32 images acquired from 29 November 2015 to 24 January 2019 can be seen in Table 5.1.

We show that meltwater from the McMIS flows off the ice shelf and onto the adjacent sea ice, forming sea ice ponds that we suggest may affect the stability of the sea ice. This process is a previously undocumented mechanism for the formation of sea-ice ponds. In each of the four

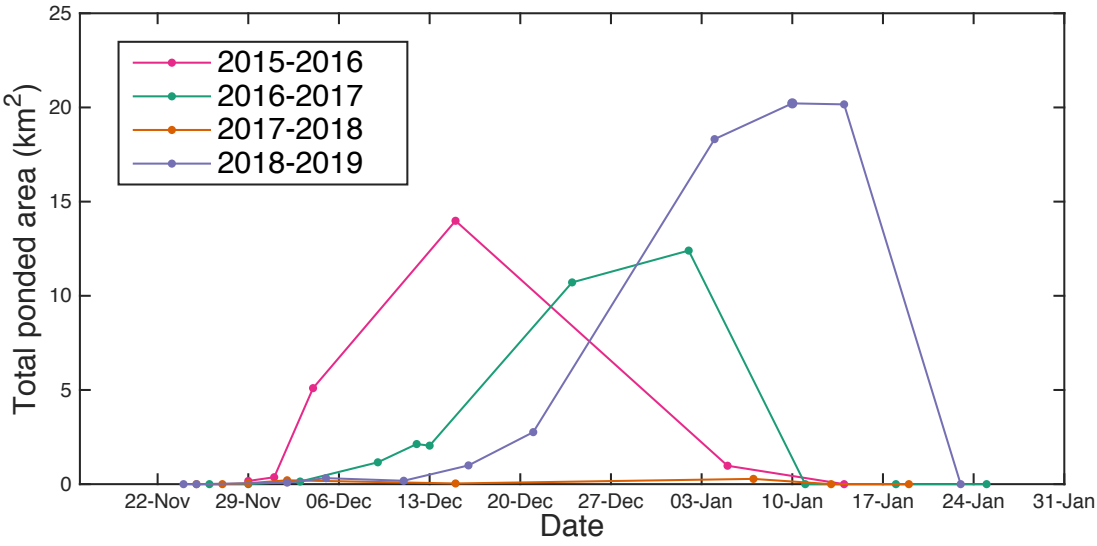

Fig. 5.3: Total ponded area in the study area during each melt season of the study period (2015/2016 to 2018/2019).

melt seasons studied, ponds first begin to develop on the sea ice immediately adjacent to the ice-shelf front in late November or early December, before expanding in number and area over the following weeks (Figs. 5.2 and 5.3). The ponds typically expand along the ice-shelf front, although in 2018/2019 some meltwater spills out of this area and a pond expands to ∼4 km from the ice-shelf front. Ponds form on the sea ice directly adjacent to the ice-shelf front, in the part that abuts the 'active surface hydrology' zone of the ice shelf (Glasser and others, 2006; Banwell and others, 2019; Macdonald and others, 2019). Throughout the study period, ponds do not form beyond an eastern limit, which corresponds to the boundary on the ice shelf between the zone of 'active surface hydrology' and 'no surface hydrology'. This supports our suggestion that the ponds are derived from ice-shelf surface meltwater runoff. Additionally, ponds do not form adjacent to a ∼1 km wide high-albedo section in the 'active surface hydrology' zone of the ice shelf, which is likely a pedestalled, relict lake. This high-albedo area can be expected to undergo less surface melting and it forms a topographic obstacle to surface streams (Macdonald and others, 2019).

The sea-ice ponds that we observe are large. Total ponded area reaches a peak of 14.0, 10.7 and 20.2 km^2 in 2015/2016, 2016/2017 and 2018/2019, respectively (Fig. 5.3). In each

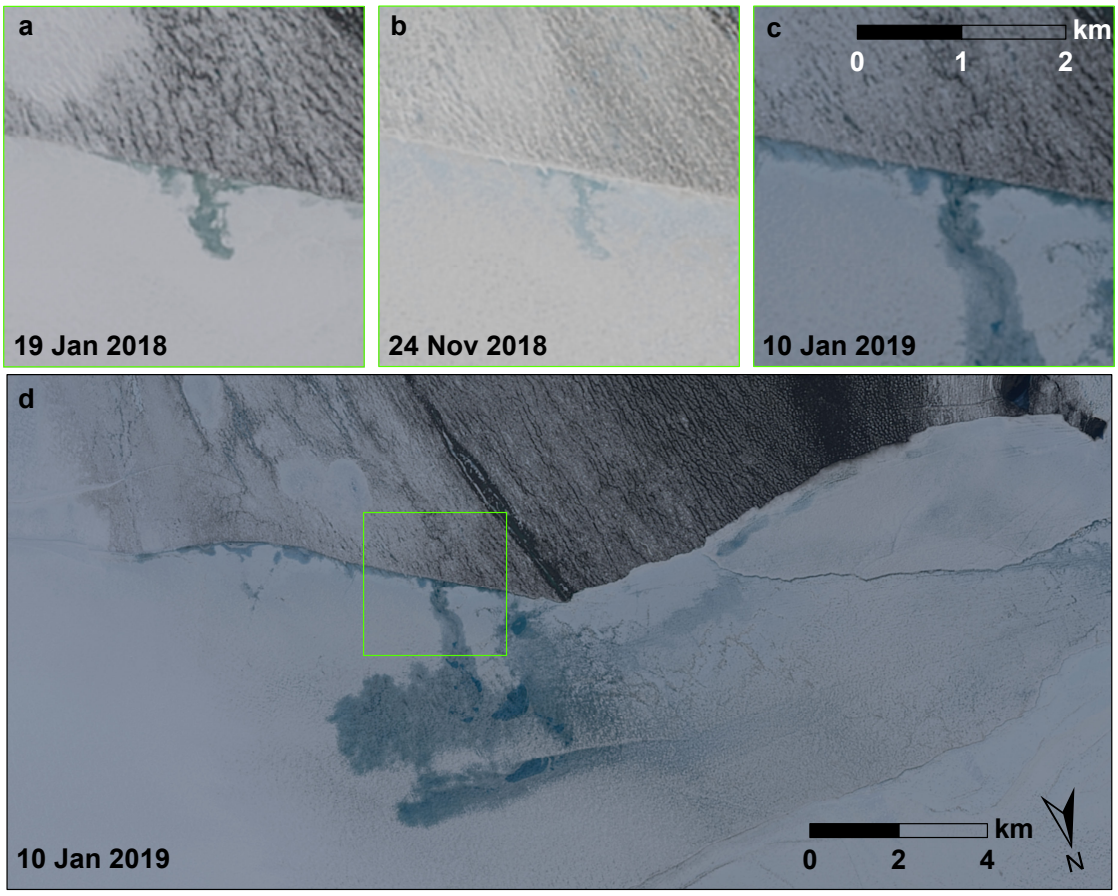

Fig. 5.4: A pond that (a) forms and freezes over in the 2017-2018 austral summer (b) persists as a feature into the following summer, when a pond forms at the same site in the same approximate form. (c) In the 2018-2019 season, ponding expands away from the ice-shelf front at this site. The extent of (d) is the same as the study site shown in Fig. 5.1 by the yellow box, and the green box in (d) shows the extent of (a-c).

case, the majority of the ponded area at its peak is contained within a single large pond. In 2017/2018, the peak ponded area reaches only 0.3 km^2. The date that peak area is reached ranges from 15 December to 10 January. Ponds can grow rapidly. For example, between 1 and 4 December 2015, total ponded area grows from 0.4 km^2 to 5.1 km^2 (Figs. 5.2a and 5.3). They expand and merge, and can reach areas substantially larger than that of typical sea ice ponds which have diameters of several meters to several tens of meters (Yackel and others, 2000; Hohenegger and others, 2012; Petrich and others, 2012; Popović and others, 2018). For example, on 15 December 2015 a single consolidated pond reaches an area of approximately 9.0 km^2. This suggests that surface meltwater runoff from ice shelves provides a mechanism

to create significantly larger sea ice ponds than otherwise develop. Previous research has suggested that there is typically an upper-limit on sea-ice pond coverage fraction because common flaws in the ice (e.g. cracks, seal holes) limit expansion (Popović and others, *in press*). Therefore, it seems that the specific conditions that exist in the sea ice adjacent to the ice shelf enable large ponds to form by restricting the formation of cracks and flaws in the ice. However, more research would be required to determine the exact cause of this phenomenon.

Eventually, the ponds freeze-over. At first, the pond may be covered by a thin, transparent ice-lid and later by a thicker, white ice-lid that masks the meltwater below. We observe evidence of freeze-over as early as 15 December, and this can occur at one pond while others continue to expand.

Ponds can influence the surface hydrology of the sea ice in the following year after they freeze-over. On 24 November 2018, before pond formation begins, a frozen-over pond that froze-over at the end of the preceding summer is still visible (Fig. 5.4). By 21 December 2018, an open-water pond is visible at this same site. Although it is common for sites to be ponded in multiple years, this is the only clear instance of a particular pond freezing-over and maintaining its form into the following season. Notably, it is at this site (along with one other site) where meltwater spills away from the ice-shelf front and causes the pond to expand into an area of the sea ice $\sim$4 km away from ice-shelf front (Figs. 5.2b and 5.4). It is unclear why the meltwater spills away from the ice-shelf front in this instance.

In addition to promoting sea-ice thinning by lowering the albedo, the formation of these ponds could flex the ice, affecting the stability of the sea ice at the ice-shelf front. Typical sea ice ponds develop from meltwater that forms and pools in-situ (Polashenski and others, 2012). Therefore, in those cases the formation of a pond does not result in any additional mass at the site. However, we show that meltwater is added from an external source (the ice shelf) to the sea ice. As has been modelled (MacAyeal and Sergienko, 2013; Banwell and MacAyeal, 2015) and observed (Banwell and others, 2019) on ice shelves, when meltwater

flows into depressions to form ponds, the added gravitational load of the water causes the ice to depress and flex at the site of the pond. This flexure stresses the ice, and can potentially cause it to fracture. Fracturing in the sea ice increases the chance that it will break-up and breakout (Arntsen and others, 2015). Additionally, because the ponds are located directly adjacent to the ice-shelf front, any fracturing or thinning they cause could be particularly important for the sea ice's influence on the ice-shelf front. Fracturing or thinning here could disrupt the sea ice's ability to buttress the ice-shelf front by detaching it from the ice shelf.

At the McMIS, previous observations suggest that sea-ice breakout promotes calving and rifting on the ice shelf. For example, the breakout of sea ice in March 2016 was associated with the calving of numerous icebergs and the extension of an ice-shelf rift (Banwell and others, 2017). Meltwater runoff from the ice shelf could, therefore, lead to ice-shelf mass loss in two ways, by: (i) direct loss of meltwater runoff and (ii) forming ponds on the sea ice that promote sea-ice thinning/break-up, thereby reducing/removing the sea ice's ability to buttress the ice-shelf front and to buffer it from ocean swells.

Presently, we only observe the formation of these ice-shelf derived ponds on sea ice adjacent to the McMIS. This could be due to several factors. First, the conditions for meltwater to flow over the ice-shelf front only exist at a limited number of ice shelves due to a combination of climatic factors and factors pertaining to the surface conditions of the ice shelf. Second, the McMIS is a relatively thin ice shelf, with a thickness near our study site of ∼10-30 m (Campbell and others, 2017). Consequently, there is a gentle sloped transition between the ice shelf and the sea ice that water can flow over. In contrast, at the Nansen Ice Shelf, which is around 200 m thick close to its terminus (Dow and others, 2018), Bell and others (2017) observed water flowing over a steep cliff as a waterfall. We suggest that in this case, particularly if the sea ice below is first-year ice, the ice-shelf runoff could break through the sea ice. Third, katabatic winds that flow at the margins of Antarctica can play a role in blowing sea ice away from the ice-shelf front (Bromwich and others, 1989).

However, this new mechanism of sea ice pond formation from ice-shelf meltwater runoff

is likely to become a more important factor in the future. Meltwater is predicted to become increasingly pervasive on ice shelves with future climate change (Trusel and others, 2015; Bell and others, 2018). As more meltwater runoff flows over ice-shelf fronts, more and larger ponds could form adjacent to more ice shelves and other marine-terminating glaciers. More work is required to understand what governs the formation of sea ice ponds from ice-shelf runoff, and how they affect sea-ice stability at the ice-shelf front. As this mechanism for sea ice pond formation becomes more prevalent, it could become a significant factor in determining ice-shelf stability at multiple sites around Antarctica.

5.5 Conclusion

This study analyses a previously-undocumented mechanism for the formation of sea ice ponds on sea ice in Antarctica. We show that, during the austral summer, meltwater runoff from the McMIS flows over the ice-shelf front and forms large ponds on the adjacent sea ice. These ponds are distinct from those typically observed in the Arctic that form from in-situ melting. Because these ponds form by adding mass to the sea ice, they could destabilize the sea ice by flexing it, as well as by reducing the albedo. Although ponds formed by this mechanism have only been found adjacent to the McMIS, they could become more prevalent around Antarctica as melting on ice shelves increases due to climate change.

5.6 Appendix: Supplementary Methods

5.6.1 Satellite Imagery Analysis

We downloaded all November-February Landsat 8 Operational Land Imager (OLI) and Sentinel-2A and 2B images of the study region that were sufficiently cloud-free over features of interest were downloaded, covering the period 29 November 2015 to 24 January 2019. Sentinel-2B only launched in March 2017, during the study period. Images with heavy cloud cover could be used for analysis provided that at least one of our sites of interest was

visible. We chose Landsat 8 and Sentinel-2, as opposed to Moderate Resolution Imaging Spectroradiometer (MODIS), because these instruments have relatively high spatial resolutions. Landsat 8 imagery has a spatial resolution of 30 m, or 15 m when pan-sharpened, and Sentinel-2 has a spatial resolution of 10 m. MODIS, in contrast, has a resolution of 250 m, which is inadequate for resolving the presence or character of many of the ponds of interest in this study.

All true-colour pan-sharpened Landsat and true-colour Sentinel images were cropped to an area encompassing the region of interest and some surrounding area (Fig. 5.1) and assembled into a time-series for analysis. Analysis was carried out using a combination of manual visual interpretation of the time-series, and quantification of ponded area using a water-identification algorithm.

Ponded-area calculations

To calculate ponded area, we first determined which images had sea ice ponds present on the sea ice adjacent to the McMurdo Ice Shelf using manual visual interpretation of true-colour images. If we determined that there were no ponds, either because none had developed yet or because they had frozen over, we assigned a value of 0 to pond area. If we determined that meltwater was present on a particular day, and the image was cloud-free over the study area (Fig. 5.1), we processed the images for pond-area quantification. If on a particular day there was both a Sentinel-2 and Landsat 8 image available, we used the Sentinel-2 image because they have a higher spatial resolution.

To process the images for pond-area quantification, we selected the blue and red bands of each image. For Landsat 8, we used band 2 (blue, 450-510 nm) and band 4 (red, 640-670 nm) and for Sentinel 2, we also used band 2 (blue, 459-525 nm) and band 4 (red, 649-680 nm). We then cropped each image to the study area (Fig. 1) using Extract by Mask in ArcMap^{TM}.

For the Landsat 8 images, we then used image's metadata to convert digital numbers to

top-of-atmosphere (TOA) reflectance and to correct for solar elevation. For the Sentinel-2 images, we used the L1C product, which has already been processed to TOA reflectance. These TOA reflectance values represent an adequate proxy for surface reflectance for our purposes (Pope and others, 2016).

To identify water-covered pixels, we calculated the normalized difference water index adapted for ice ($NDWI_{ice}$), defined as

$$(NDWI_{ice}) = B2 - B4 / (B2 + B4)$$

where B2 and B4 represent the blue and red bands, respectively. We determined a threshold ($NDWI_{ice}$) value by testing different values and comparing the results to our manual visual interpretation of the images. Pixels with an ($NDWI_{ice}$) value above this value were assigned as water-covered. For Landsat 8 images, pixels with ($NDWI_{ice}$) >0.12 were assigned as water-covered. This threshold value has been used to detect water-covered pixels in Landsat 8 in other studies on glaciers and ice shelves (e.g. Yang and Smith, 2013; Bell and others, 2017). For Sentinel-2 images, we found a lower threshold value of ($NDWI_{ice}$) >0.09 to be most suitable.

Following previous studies of ponds on glaciers and ice shelves (Pope and others, 2016; Macdonald and others, 2018), we then excluded ponds that were identified as having an area of ≤4 pixels. We deemed that a threshold of 4 was sufficiently high to exclude small ponds that consisted exclusively of mixed pixels (i.e. pixels with a value representative of the average of different surface types e.g. snow/ice/water), while being sufficiently low to maximize the inclusion of small lakes. This meant that the smallest detectable pond area was 0.0036 km^2 for Landsat 8 images, and 0.0004 km^2 for Sentinel-2 images.

Differences in the spatial resolution, and radiometric differences between the bands, of the two satellite instruments will be responsible for some differences in the calculated areas between images.

Table 5.1: Table of satellite image IDs and dates used to compile the time-series used for analysis of sea ice ponds. All Sentintel-2 images are product level MSIL1C, tile number T58CEU and 'Standard Archive Format for Europe' (SAFE) product format, except on 14 January 2016 where the image has no tile number.

Date	Sensor	Image ID
29 November 2015	Landsat 8 OLI	LC82241282015333LGN01
01 December 2015	Landsat 8 OLI	LC80531162015335LGN01
04 December 2015	Landsat 8 OLI	LC82271282015338LGN01
15 December 2015	Landsat 8 OLI	LC80551162015349LGN01
05 January 2016	Landsat 8 OLI	LC82271282016005LGN02
14 January 2016	Sentinel 2A	S2A_OPER_20160330T074715_R085_20160114T203520
23 January 2016	Landsat 8 OLI	LC80561152016023LGN01
01 February 2016	Landsat 8 OLI	LC80551162016032LGN01
29 November 2016	Landsat 8 OLI	LC82261282016334LGN01
03 December 2016	Landsat 8 OLI	LC80531162016338LGN01
09 December 2016	Sentinel 2A	S2A_20161209T203522_N0204_R085_20161209T203516
12 December 2016	Sentinel 2A	S2A_20161212T204512_N0204_R128_20161212T204514
13 December 2016	Sentinel 2A	S2A_20161213T201532_N0204_R142_20161213T201529
24 December 2016	Landsat 8 OLI	LC80561152016359LGN01
02 January 2017	Sentinel 2A	S2A_20170102T201522_N0204_R142_20170102T201525
11 January 2017	Landsat 8 OLI	LC82231282017011LGN01
18 January 2017	Sentinel 2A	S2A_20170118T203511_N0204_R085_20170118T203509
25 January 2017	Sentinel 2A	S2A_20170125T202521_N0204_R042_20170125T202517
28 January 2017	Sentinel 2A	S2A_20170128T203511_N0204_R085_20170128T203513
31 January 2017	Sentinel 2A	S2A_20170131T204511_N0204_R128_20170131T204617
05 February 2017	Sentinel 2A	S2A_20170205T195521_N0204_R056_20170205T195519
11 February 2017	Sentinel 2A	S2A_20170211T201531_N0204_R142_20170211T201525
14 February 2017	Sentinel 2A	S2A_20170214T202521_N0204_R042_20170214T202519
04 November 2017	Landsat 8 OLI	LC80531162017308LGN00
13 November 2017	Landsat 8 OLI	LC80521162017317LGN00
25 November 2017	Landsat 8 OLI	LC80561152017329LGN00
27 November 2017	Landsat 8 OLI	LC80541162017331LGN00
29 November 2017	Landsat 8 OLI	LC80521162017333LGN00
02 December 2017	Landsat 8 OLI	LC80571152017336LGN00
15 December 2017	Landsat 8 OLI	LC80521162017349LGN00
07 January 2018	Landsat 8 OLI	LC80531162018007LGN00
13 January 2018	Sentinel 2A	S2A_20180113T203621_N0206_R085_20180113T215509
19 January 2018	Landsat 8 OLI	LC80571152018019LGN00
12 February 2018	Sentinel 2A	S2A_20180212T203621_N0206_R085_20180212T232245
24 November 2018	Sentinel 2B	S2B_20181124T203629_N0207_R085_20181124T212417
25 November 2018	Sentinel 2B	S2B_20181125T200529_N0207_R099_20181125T210826
26 November 2018	Landsat 8 OLI	LC82271282018330LGN00
30 November 2018	Landsat 8 OLI	LC80541162018334LGN00
02 December 2018	Landsat 8 OLI	LC80521162018336LGN00
05 December 2018	Sentinel 2B	S2B_20181205T200529_N0207_R099_20181205T223759
11 December 2018	Landsat 8 OLI	LC80511162018345LGN00
16 December 2018	Landsat 8 OLI	LC82231282018350LGN00
21 December 2018	Landsat 8 OLI	LC80571152018355LGN00
04 January 2019	Sentinel 2B	S2B_20190104T200529_N0207_R099_20190104T210616
10 January 2019	Landsat 8 OLI	LC82221292019010LGN00
14 January 2019	Sentinel 2B	S2B_20190114T200529_N0207_R099_20190114T211558
15 January 2019	Landsat 8 OLI	LC80561152019015LGN00
23 January 2019	Sentinel 2B	S2B_20190123T203629_N0207_R085_20190123T212532
24 January 2019	Sentinel 2B	LC80551162019024LGN00
13 February 2019	Sentinel 2B	S2B_20190213T200529_N0207_R099_20190213T223839
16 February 2019	Landsat 8 OLI	LC80561162019047LGN00

CHAPTER 6

CONCLUSION

This thesis presents a study of the surface hydrology of ice shelves using remote sensing, fieldwork and modelling, and assesses the implications of the results for ice-shelf stability. This was done with the goal of improving knowledge and understanding of ice-shelf hydrology and processes, ultimately enabling better predictions of the response of ice shelves and ice sheets to climate change.

In Chapter 2, in the first quantitative study of surface lakes on a floating ice tongue in Greenland, we analyzed remote sensing data to study the seasonal evolution of surface lakes on the floating tongue of Petermann Glacier, north Greenland over the boreal summers of 2014-2016. Each year, surface lakes develop in early-mid June as air temperatures increase and their total number, volume and area peaks in late June/early July. Despite sustained high temperatures, total lake number, volume and area then declines through July and August. We suggest that this is due both to meltwater drainage across the tongue and into the ocean by a river, and to rapid vertical lake drainage events on the tongue. Further, the fact that mean lake depth remains relatively constant during this time suggests that a large proportion of the lakes that drain do so completely, likely by rapid hydrofracture. The mean areas of lakes on the tongue are calculated to be only $\sim$20% of those on the grounded ice and exhibit lower variability in maximum and mean depth, differences likely attributable to the contrasting formation processes of lakes in each environment. Predicted future rises in air temperature could enable a higher density of lakes, with larger volumes, to develop from earlier in the season on Petermann's tongue. This could potentially lead to increased ice-tongue instability. However, the decline of surface lakes through July and August in each year studied, despite sustained high temperatures during those months, suggests that evacuation of meltwater from the tongue may limit the total volumes of meltwater storage on Petermann's tongue, thereby mitigating the risk of instability and break-up from surface lakes.

In Chapter 3, in the first study of how surface lakes develop on a debris-covered ice shelf, we analyzed remote sensing and field data to study the formation of pedestalled, relict lakes ('pedestals') on the McMurdo Ice Shelf, Antarctica. In the western portion of the McMurdo Ice Shelf, where debris covers much of the surface, differential ablation between debris-covered and debris-free areas creates an unusual heterogeneous surface of topographically low, high-ablation areas, and topographically raised ('pedestalled'), low-ablation areas. Our analysis shows that pedestalled relict lakes ('pedestals') form when an open water surface lake that develops on the ice shelf in the summer, freezes-over in winter, resulting in the lake-bottom debris being masked by a high-albedo ice surface. If this ice surface fails to melt during a subsequent melt season, it experiences reduced surface ablation relative to the surrounding debris-covered areas of the ice shelf. We propose that this differential ablation, and resultant hydrostatic and flexural readjustments of the ice shelf, causes the former surface lake to become increasingly pedestalled above the lower topography of the surrounding ice shelf. Consequently, meltwater streams cannot flow onto these pedestals, and instead divert around them. The development of pedestals has a significant influence on the surface-energy balance, hydrology and, potentially, flexure of the ice shelf.

In Chapter 4, we studied the flexural effect of pedestal formation on ice shelves using an elastic model of an idealized pedestal. Changes in ice thickness associated with pedestal formation induce a flexural response that causes a depression to develop adjacent to the pedestal, which can explain the observation of preferential ponding adjacent to pedestals. Greater amounts of stress are produced from pedestal formation on thinner ice shelves, but the associated stress is unlikely to be sufficient to cause fracturing and affect ice-shelf stability on the McMurdo Ice Shelf or other existing ice shelves, which are not sufficiently thin. The relationship between pedestal radius and stress is complex, but in no case did varying pedestal radius in our model lead to sufficient stress to cause ice-shelf fracturing (using a fracture threshold of a von Mises stress of 70 kPa). Although the results suggest that only pedestal evolution on an exceptionally thin ice shelf with high differential ablation

is likely to cause sufficient flexure to initiate fracturing, it is conceivable that such conditions could be met in the future at the McMurdo Ice Shelf or elsewhere due to ice-shelf thinning caused by air and ocean warming.

In Chapter 5, we analyzed remote sensing data to study the formation of sea ice ponds from ice-shelf runoff adjacent to the McMurdo Ice Shelf over the austral summers from 2015/2016 to 2018/2019. Each summer, meltwater flows from the ice shelf onto the sea ice and forms large (up to 9 km^2) ponds immediately adjacent to the ice front. This is a previously undocumented mechanism for the formation of sea ice ponds and could have consequences for the stability of the sea ice, and by implication, the ice shelf. These ponds decrease the sea ice's albedo, causing it to thin. Additionally, we suggest the added mass of ice-shelf runoff causes the sea ice to flex. Both of these processes could promote break-up of the sea ice, which could promote calving of the ice shelf. As surface melting on ice shelves increases, ice-shelf surface hydrology is expected to have a greater effect on sea-ice surface hydrology and stability.

This thesis expands knowledge of ice-shelf surface hydrology and its implications for ice-shelf stability. It includes the first analysis of surface hydrology on a Greenland ice shelf, a debris-covered ice shelf, and the interaction between the hydrology of an ice shelf and sea ice. Through this analysis, we have gained a greater understanding of ice-shelf hydrology and processes, which will enable the scientific community to better predict the response of the polar ice sheets to climate change. Furthermore, we have highlighted the complex nature of the relationship between ice-shelf hydrology and ice-shelf stability, and the need for more research in this subject area.

REFERENCES

Albrecht, T., and A. Levermann (2012), Fracture field for large-scale ice dynamics, J. Glaciol., 58(207), 165-176

Alley, R., T. Dupont, B. Parizek, and S. Anandakrishnan (2005), Access of surface meltwater to beds of sub-freezing glaciers: Preliminary Insights, Ann. Glaciol., 40, 8-14

Andreas, E. L. and S. F. Ackley (1981), On the differences in ablation seasons of Arctic and Antarctic sea ice, J. Atmos. Sci., 39, 440-447

Arntsen, A. E., Song, A. J., Perovich, D. K. and J. A. Richter-Menge (2015), Observations of the summer breakup of an Arctic sea ice cover, Geophys. Res. Lett. 42, 8057-8063

Arnold, N. S., A. F. Banwell, and I. C. Willis (2014), High-resolution modelling of the seasonal evolution of surface water storage on the Greenland Ice Sheet, The Cryos., 8, 1149-1160

Aschwanden, A. and 7 others (2019), Contribution of the Greenland Ice Sheet to sea level over the next millennium, Sci. Adv., 5, eaav9396

Bamber, J. L., M. J. Siegert, J. A. Griggs, S. J. Marshall and G. Spada (2013), Paleofluvial mega-canyon beneath the central Greenland ice sheet, Science, 341(6149), 997-999

Banwell, A. F and 5 others (2012), Calibration and validation of a high resolution surface mass balance model for Paakitsoq, west Greenland, J. Glaciol., 58(212), 1047-1062

Banwell, A. F., D. R. MacAyeal, and O. V. Sergienko (2013), Breakup of the Larsen B Ice Shelf triggered by chain reaction drainage of surface lakes, Geophys. Res. Lett, 40, 5872-5876

Banwell, A. F. and 5 others (2014), surface lakes on the Larsen B ice shelf, Antarctica, and at Paakitsoq, West Greenland: A comparative study. Ann. Glaciol., 55(66), 1-8

Banwell, A.F., and D. R. MacAyeal, (2015), Ice-shelf fracture due to viscoelastic flexure stress induced by fill/drain cycles of surface lakes, Ant. Sci, 27, 587-597

Banwell, A. F. and 6 others (2017), Calving and rifting on the McMurdo Ice Shelf, Antarctica, Ann. Glaciol., 58(75), 78-87

Banwell, A. F., I. C. Willis, G. J. Macdonald, B. Goodsell and D. R. MacAyeal (2019), Direct measurements of ice-shelf flexure caused by surface meltwater ponding and drainage, Nat. Comm., 10(730)

Bartholomew, I. and 5 others (2010), Seasonal evolution of subglacial drainage and acceler-

ation in a Greenland outlet, Nat. Geosci., 3, 408-411

Bell, R. E. and 9 others (2017), Antarctic ice shelf potentially stabilized by export of meltwater in surface river, Nature, 544, 344-348

Bell R. E., A. F. Banwell, L. Trusel and J. Kingslake (2018), Antarctic Surface Hydrology and impacts on ice sheet mass balance, Nat. Cli. Ch., 8, 1044-1052

Bevan, S. L. and 9 others (2017), Centuries of intense surface melt on Larsen C Ice Shelf, The Cryos., 11(6), 2743-2753

Bevis, M. and 13 others (2019), Accelerating changes in ice mass within Greenland, and the ice sheet's sensitivity to atmospheric forcing, Proc. Natl. Acad. Sci. USA, 116, 1934-1939

Bindschadler, R. and 17 others (2011), Getting around Antarctica: new high-resolution mappings of the grounded and freely-floating boundaries of the Antarctic ice sheet created for the International Polar Year, The Cryos., 5, 569-588

Box, J. E. and K. Ski (2007), Remote sounding of Greenland surface melt lakes: implications for subglacial hydraulics, J. Glaciol., 53(181), 257-265

Bromwich, D. H. (1989), Satellite Analyses of Antarctic Katabatic Wind Behavior. Bull. Am. Meteorol. Soc., 70, 738-749

Cailleux, A. (1962), Ice mounds in frozen lakes in McMurdo Sound, Antarctica, J. Glaciol. 4(31), 131-133

Campbell, S., Z. Courville, S. Sinclair and J. Wilner (2017), Brine, englacial structure and basal properties near the terminus of McMurdo Ice Shelf, Antarctica, Ann. Glaciol., 58(74), 1-11

Clendon, P. C. (2009), Summertime surface mass balance and atmospheric processes on the McMurdo Ice Shelf, Antarctica, PhD Diss., Univ. of Canterbury

Csatho, B. M. and 9 others (2014), Laser altimetry reveals complex pattern of Greenland Ice Sheet Dynamics, Proc. Natl. Acad. Sci., 111(52), 18478-18483

Curry, J. A., J. L. Schramm, and E. E. Ebert (1995), Sea ice-albedo climate feedback mechanism, J. Clim., 8(2), 240-247

Das, S. B. and 6 others (2008), Fracture propagation to the base of the Greenland Ice Sheet during surface lake drainage, Science, 320(5877), 778-781

Debenham, F. (1965), The genesis of the McMurdo Ice Shelf, Antarctica, J. Glaciol., 5(42), 829-832

DeConto R. M. and D. Pollard (2016), Contribution of Antarctica to past and future sea-level rise, Nature, 531(7596), 591-597

De Rydt, J., G. H. Gudmundsson, H. Rott and J. L. Bamber (2015), Modeling the instantaneous response of glaciers after the collapse of the Larsen B Ice Shelf, Geophys. Res. Lett., 42, 5355-5363

Dow, C. F. and 8 others (2018), Basal channels drive active surface hydrology and transverse ice shelf fracture, Sci. Adv., 4(6), eaao7212

Dupont, T. K and R. B. Alley (2005), Assessment of the importance of ice-shelf buttressing to ice-sheet flow, Geophys. Res. Lett., 32(4), L04503

Echelmeyer, K., T. S. Clarke and W. D. Harrison (1991), Surficial glaciology of Jakobshavn Isbrae, West Greenland: Part 1. Surface morphology, J. Glaciol., 37(127), 368-382

Enderlin, E. M and 5 others (2014), An improved mass budget for the Greenland ice sheet, Geophys. Res. Lett., 41, 866-872

Fitzsimons, S., S. Mager, R. Frew, A. Clifford and G. Wilson (2012), Formation of ice-shelf moraines by accretion of sea water and marine sediment at the southern margin of the McMurdo Ice Shelf, Antarctica, Ann. Glaciol. 53(60), 211-220

Fretwell, P. and 59 others (2013), Bedmap2: improved ice bed, surface and thickness datasets for Antarctica, The Cryos., 7, 375-393

Gilbert, R., and E. W. Domack (2003), Sedimentary record of disintegrating ice shelves in a warming climate, Antarctic Peninsula, Geochem. Geophys. Geosyst., 4(4), 1038

Glasser, N. F. and T. A. Scambos (2008), A structural glaciological analysis of the 2002 Larsen B ice-shelf collapse, J. Glaciol., 55(191), 400-410

Glasser, N., B. Goodsell, L. Copland and W. Lawson (2006), Debris characteristics and ice-shelf dynamics in the ablation region of the McMurdo Ice Shelf, Antarctica, J. Glaciol., 52(177), 223-234

Glasser, N. F., T. Holt, E. Fleming and C. Stevenson (2014), Ice shelf history determined from deformation styles in surface debris, Ant. Sci., 26(6), 661-673

Grenfell, T. C., and D. K. Perovich (2004), Seasonal and spatial evolution of albedo in a snow-ice-land-ocean environment, J. Geophys. Res., 109, C01001

Hill, E. A., J. R. Carr, C. R. Stokes and G. H. Gudmundsson (2018), Dynamic changes in outlet glaciers in northern Greenland from 1948 to 2015, The Cryos., 12, 3243-3263

Hogg, A. E., A. Shepherd, N. Gourmelen and M. Engdahl (2016), Grounding line migration from 1991 to 2011 on Petermann Glacier, North-West Greenland, J. Glaciol., 62(236), 1104-1114

Hohenegger, C., B. Alali, K. R. Steffen, D. K. Perovich, and K. M. Golden (2012), Transition in the fractal geometry of Arctic melt ponds, The Cryos. 6(5), 1157-1162

Humphrey, N. F., J. T. Harper and W. T. Pfeffer (2012), Thermal tracking of meltwater retention in Greenland's accumulation area, J. Geophys. Res., 117,F01010

Ingle, J. D. and S. R. Crouch SR (1988) Spectrochemical measurements, In Ingle, J. D. and S. R. Crouch eds. Spectrochemical analysis. Prentice Hall, Upper Saddle River, New Jersey

Johansson, A. M., P. Jansson and I. A. Brown (2013), Spatial and temporal variations in lakes on the Greenland Ice Sheet, J. Hydrol., 476, 314-320

Joughin, I., B. E. Smith and B. Medley (2014), Marine ice sheet collapse potentially under way for the thwaites glacier basin, West Antarctica. Science, 344 (6185), 735-738

Kellogg, T. B., D. E. Kellogg and M. Stuiver (1990), Late Quaternary history of the southwestern Ross Sea: evidence from debris bands on the McMurdo Ice Shelf, Antarctica, in Bentley, C. R., ed. Contributions to Antarctic research I., Washington DC, American Geophysical Union, 25-56 (Antarctic Research Series 50)

Kingslake, J., F. Ng and A. Sole (2015), Modelling channelized surface drainage of surface lakes, J. Glaciol., 61(225), 185-199

Kingslake, J., J. C. Ely, I. Das and R. E. Bell (2017), Widespread movement of meltwater onto and across Antarctic Ice Shelves, Nature, 544(349), 349-352

Kirtman, B. and 16 others (2013), Near-term Climate Change: Projections and Predictability: In: Climate Change 2013: The Physical Science Basis. Contribution of Working Group 1 to the Fifth Assess. Report of the Int. Panel on Clim. Cha. (eds. Strocker, T. F. and 9 others), 953-1028 (Cambridge Univ. Press)

Klokov, V. and D. Diemand (1995), Glaciology of the McMurdo Ice Shelf in the area of air operations, Contributions to Antarctic Research IV, Ant. Res. Ser., 67, 175-195

Koenig, L. S. and 11 others (2015), Wintertime storage of water in buried surface lakes across the Greenland Ice Sheet, The Cryos., 9, 1333-1342

LaBarbera, C. H. and D. R. MacAyeal (2011), Traveling surface lakes on George VI Ice Shelf, Antarctica, Geophys. Res. Lett., 38(24), L24501

Langen, P. L. and 13 others (2015), Quantifying Energy and Mass Fluxes Controlling

Godthbsfjord Freshwater Input in a 5-km Simulation (1991-2012), J. of Clim., 28, 3694-3713

Langen, P. L., R. S. Fausto, B. Vandecrux, R. H. Mottram and J. E. Box (2017), Liquid Water Flow and Retention on the Greenland Ice Sheet in the Regional Climate Model HIRHAM5: Local and Large-Scale Impacts, Front. Earth Sci., 4(110), 1-18

Langley E.S., A. A. Leeson, C. R. Stokes and S.S.R. Jamieson (2016), Seasonal evolution of surface lakes on an East Antarctic outlet glacier, Geophys. Res. Lett., 43(16), 8563-8571

Le Brocq, A.M., and 8 others (2013), Evidence from ice shelves for channelized meltwater flow beneath the Antarctic ice sheet, Nat. Geo., 6, 945-948

Leeson, A. A. and 7 others (2013), A comparison of surface lake observations derived from MODIS imagery at the western margin of the Greenland ice sheet, J. Glaciol., 59(218), 1179-1188

Lenaerts, J. T. M. and 12 others (2016), Meltwater produced by wind-albedo interaction stored in an East Antarctic ice shelf, Nat. Clim. Cha., 7, 58-62

Liang, Y.-L. and 7 others (2012), A decadal investigation of surface lakes in West Greenland using a fully automatic detection and tracking algorithm, Rem. Sens. Env., 123, 127-138

Lüthje, M., L. T. Pedersen, N. Reeh and W. Gruell (2006), Modelling the evolution of supra-glacial lakes on the western Greenland Ice Sheet margin, J. Glac., 52(179), 608-618

MacAyeal D. R. and O. V. Sergienko (2013), The flexural dynamics of melting ice shelves, Ann. Glaciol., 54(63), 1-10

MacAyeal, D. R., Sergienko, O. V. and A. F. Banwell (2015), A model of viscoelastic ice-shelf flexure, J.Glac., 61(228), 635-645

MacAyeal, D. R. and 6 others (2018), Diurnal seismicity cycle linked to subsurface melting on an ice shelf, Ann. Glaciol. 60(79), 137-157

Macdonald, G. J., A. F. Banwell and D. R. MacAyeal (2018), Seasonal evolution of supraglacial lakes on a floating ice tongue, Petermann Glacier, Greenland, Ann. Glaciol., 59(76), 56-65

Macdonald, G. J. and 5 others (2019), Formation of pedestalled, relict lakes on the McMurdo Ice Shelf, Antarctica, J. Glaciol., 65(220), 337-343

Macdonald, G. J., P. Popović and D. P. Mayer (in review), Formation of sea ice ponds from ice-shelf runoff, adjacent to the McMurdo Ice Shelf, Antarctica, Ann. Glaciol., 61(82)

Massom, R. A. and 5 others (2018), Antarctic ice shelf disintegration triggered by sea ice loss and ocean swell, Nature, 558, 383-389

Matsuoka, K., Skoglund, A. and G. Roth (2018), Quantarctica [Data set], Norwegian Polar Institute.

McGrath, D. and 5 others (2012), Basal crevasses on the Larsen C Ice Shelf, Antarctica: implications for meltwater ponding and hydrofracture, Geophys. Res. Lett., 39(16), L16504

McMillan, M., P. Nienow, A. Shepherd, T. Benham and A. Sole (2007), Seasonal evolution of supra-glacial lakes on the Greenland Ice Sheet, Earth Planet. Sci Lett., 262(3), 484-492

Mercer, J. H. (1978), West Antarctic ice sheet and CO2 greenhouse effect: a threat of disaster, Nature, 271(5643), 321-325

Miles, K. E., I. C. Willis, C. L. Benedek, A. G. Williamson and M. Tedesco (2017), Toward monitoring Surface and subsurface lakes on the Greenland Ice Sheet using Sentinel-1 SAR and Landsat-8 OLI imagery, Front. Earth Sci., 5(58)

Miles, E. S., Willis, I., Buri, P., Steiner, J., Arnold, N.S. and Pellicciotti, F. (2018), Surface pond energy absorption across four Himalayan glaciers accounts for 1/8 of total catchment ice loss, Geophys. Res. Lett., 45(19), 10646-10473

Moon, T., I. Joughin, B. Smith and I. Howat (2012), 21st-Century evolution of Greenland outlet glacier velocities,, Science, 336(6081), 576-578

Mouginot J. and 7 others (2015), Fast retreat of Zachari Isstrm, northeast Greenland, Science, 350(6266), 1357-1361

Münchow, A., L. Padman, and H. A. Fricker (2014), Interannual changes of the floating ice shelf of Petermann Gletscher, North Greenland, from 2000 to 2012, J. Glaciol., 60(221), 489-499

National Snow and Ice Data Center (NSIDC), Sea ice features: Introduction, Accessed 1 May 2019 https://nsidc.org/cryosphere/seaice/characteristics/features.html

Nick F. M. and 8 others (2012), The response of Petermann Glacier, Greenland, to large calving events, and its future stability in the context of atmospheric and oceanic warming, J. Glaciol., 58(208), 229-239

Oppenheimer, M. and 45 others (in press), Chapter 4: Sea Level Rise and Implications for Low Lying Islands, Coasts and Communities, In: Special Report on the Ocean and Cryosphere in a Changing Climate [Pörtner, O.-H. and 10 others (eds.)]

Østrem, G. (1959), Ice melting under a thin layer of moraine, and the existence of ice cores

in moraine ridges, Geogra. Ann, 41(4), 228-230

Paige, R. A. (1968), Sub-surface melt ponds in the McMurdo Ice Shelf, Antarctica, J. Glaciol., 7(51), 511-516

Perovich, D. K., T. C. Grenfell, B. Light, and P. V. Hobbs (2002), Seasonal evolution of the albedo of multiyear Arctic sea ice, J. Geophys. Res., 107(C10), 8044

Perovich, D. K. and 5 others (2003), Thin and thinner: Sea ice mass balance measurements during SHEBA, J. Geophys. Res., 108(C3), 8050

Petrich, C., H. and 6 others (2012), Snow dunes: A controlling factor of melt pond distribution on Arctic sea ice. J. Geophys. Res.: Ocs., 117(C9)

Poinar, K. and 5 others (2015), Limits to future expansion of surface-melt-enhanced ice flow into the interior of western Greenland, Geophys. Res. Lett., 42, 1800-1807

Polashenski, C., D. Perovich, and Z. Courville (2012), The mechanisms of sea ice melt pond formation and evolution, J. Geophys. Res., 117, C01001

Pope, A. and 6 others (2016), Estimating surface lake depth in West Greenland using Landsat 8 and comparison with other multispectral methods, The Cryos., 10(1), 15-27

Popović , P., B. B. Cael, M. Silber and D. S. Abbot (2018), Simple Rules Govern the Patterns of Arctic Sea Ice Melt Ponds, Phys. Rev. Lett., 120, 148701

Popović , P., M. Silber and D. S. Abbot (in press), Critical percolation threshold is an upper bound on Arctic sea ice melt pond coverage

Rack, W., C. Haas, P. J. Langhorne (2013), Airborne thickness and freeboard measurements over the McMurdo Ice Shelf, Antarctica, J. Geophys. Res., 118, 5899-5907

Rack, W., M. A. King, O. J. Marsh, C. T. Wild and D. Flordicioiu (2017), Analysis of ice shelf flexure and its InSAR representation in the grounding zone of the southern McMurdo Ice Shelf, The Cryos., 11, 2481-2490

Richards, J.A. and Jia, X. (1999), Remote sensing digital image analysis. An Introduction. 3rd Edition. Springer, Berlin, Heidelberg, New York, 363pp

Rignot, E. (1998), Hinge-line migration of Petermann Gletscher, north Greenland, detected using satellite-radar interferometry, J. Glaciol., 44(148), 469-476

Rignot, E. and 5 others (2004), Accelerated ice discharge from the Antarctic Peninsula following the collapse of Larsen B ice shelf, Geophys. Res. Lett., 31, L18401

Rignot, E. and 5 others (2019), Four decades of Antarctic Ice Sheet mass balance from 1979-2017, Proc. Natl Acad. Sci. USA, 116, 1095-1103

Robel, A. A. (2017), Thinning ice weakens buttressing force of iceberg mlange and promotes calving, Nat. Comm., 8(14596), 1-7

Rott, H., F. Mller, T. Nagler and D. Floricioiu (2011), The imbalance of glaciers after disintegration of Larsen-B ice shelf, Antarctic Peninsula, The Cryos., 5(1), 125-134

Scambos, T. A., C. Hulbe, M. Fahnestock and J. Bohlander (2000), The link between climate warming and break-up of ice shelves in the Antarctic Peninsula, J. Glaciol., 46(154), 516-530

Scambos, T. A., C. Hulbe and M. Fahnestock (2003), Climate-induced ice shelf disintegration in the Antarctic Peninsula. In: Antarctic Peninsula climate variability: a historical and paleoenvironmental perspective (eds. Domack, E. W., A. Burnett, A. Leventer, P. Conley, M. Kirby and R. Bindschadler) American Geophysical Union, Washington, DC, 79-92

Scambos, T. A., J. A. Bohlander, C. A. Shuman and P. Skvarca (2004), Glacier acceleration and thinning after ice shelf collapse in the Larsen B embayment, Antarctica, Geophys. Res. Lett., 31(18), L18402

Scambos, T. A. and 7 others (2009), Ice shelf disintegration by plate bending and hydro-fracture: satellite observations and model results of the 2008 Wilkins Ice Shelf break-ups, Ear. and Planet Sci. Let., 280, 51-60

Scheuchl, B., J. Mouginot, E. Rignot, M. Morlighem and A. Khazendar (2016), Grounding line retreat of Pope, Smith, and Kohler Glaciers, West Antarctica, measured with Sentinel-1a radar interferometry data, Geophys Res. Lett., 43(16), 8572-8579

Selmes, N., T. Murray and T. D. James (2011), Fast draining lakes on the Greenland Ice Sheet, Geophys. Res. Lett., 38(15), L15501 Sergienko, O. (2013), Glaciological twins: basally controlled subglacial and surface lakes, J. Glaciol., 59(213), 3-8

Shen, Q. and 5 others (2018), Recent high-resolution Antarctic ice velocity maps reveal increased mass loss in Wilkes Land, East Antarctica, Nat. Sci. Rep., 8(1), 4477

Sneed, W. A. and G. S. Hamilton (2007), Evolution of melt pond volume on the surface of the Greenland Ice Sheet, Geophys. Res. Lett., 34(3), L03501

Stokes, C. R., J. E. Sanderson, B. W. J. Miles, S. S. R. Jamieson and A. A. Leeson (2019), Widespread distribution of surface lakes around the margin of the East Antarctic Ice Sheet, Nat. Sci. Rep., 9, 13823

Tedesco, M. and 7 others (2012), Measurement and modeling of ablation of the bottom of surface lakes in western Greenland, Geophys. Res. Lett., 39(2), L02502

Tedesco, M. and 5 others(2013), Ice dynamic response to two modes of surface lake drainage on the Greenland ice sheet, Environ. Res. Lett., 8(3), 034007

Tedesco, M. and 7 others (2014), Greenland Ice Sheet [in Arctic Report Card (2014)], http://www.arctic.noaa.gov/Report-Card

Tedesco, M. and 10 others (2015), Greenland Ice Sheet [in Arctic Report Card (2015)], http://www.arctic.noaa.gov/Report-Card

Tedesco, M. and 10 others (2016), Greenland Ice Sheet [in Arctic Report Card (2016)], http://www.arctic.noaa.gov/Report-Card

Thomsen, H. H., L. Thorning and R. J. Braithwaite (1988), Glacier-hydrological conditions on the Inland Ice north-east of Jacobshavn/Illulisat, West Greenland, Rapp. Grnl. Geol. Unders. 138 (Copenhagen, Denmark)

Trusel, L. D. and 6 others (2015), Divergent trajectories of Antarctic surface melt under two twenty-first-century climate scenarios, Nat. Geo., 8, 927-932

Vaughan, D. G. (1995), Tidal flexure at ice shelf margins, J. Geophys. Res., 100(B4), 6213-6224

van As, D. and 6 others (2016), Placing Greenland ice sheet ablation measurements in a multi-decadal context, Geol. Surv. Den. Greenl. Bull.,35, 71-74

van den Broeke, M. R. and 7 others (2016), On the recent contribution of the Greenland ice sheet to sea level change, The Cryos., 10, 1933-1946

van der Veen, C. J. (1998), Fracture mechanics approach to penetration of bottom crevasses on glaciers, Cold Reg. Sci. Tech., 27(3), 213-223

van der Veen, C. J. (2007), Fracture propagation as means of rapidly transferring surface meltwater to the base of glaciers, Geophys. Res. Lett., 34(1), L01501

Walker, R. T. and 5 others (2013), Ice-shelf tidal flexure and subglacial pressure variations, Earth and Planet. Sci. Lett., 361, 422-428

Weertman, J. (1973), Can a water-filled crevasse reach the bottom surface of a glacier?, IAHS Publ., 95, 139-145

Wuite, J. and 7 others (2015), Evolution of surface velocities and ice discharge of Larsen B outlet glaciers from 1995 to 2013, The Cryos., 9, 957-968

Yackel, J. J., D. G. Barber, and J. M. Hanesiak (2000), Melt ponds on sea ice in the Canadian Archipelago: 1. Variability in morphological and radiative properties, J. Geophys.

Res.: Ocs., 105(C9), 22049-22060

Yang, K. and L. C. Smith (2013), Supraglacial Streams on the Greenland Ice Sheet Delineated From Combined Spectral-Shape Information in High-Resolution Satellite Imagery, IEEE Geosci. and Rem. Sens. Lett., 10(4), 801-805